

AD-A157 535

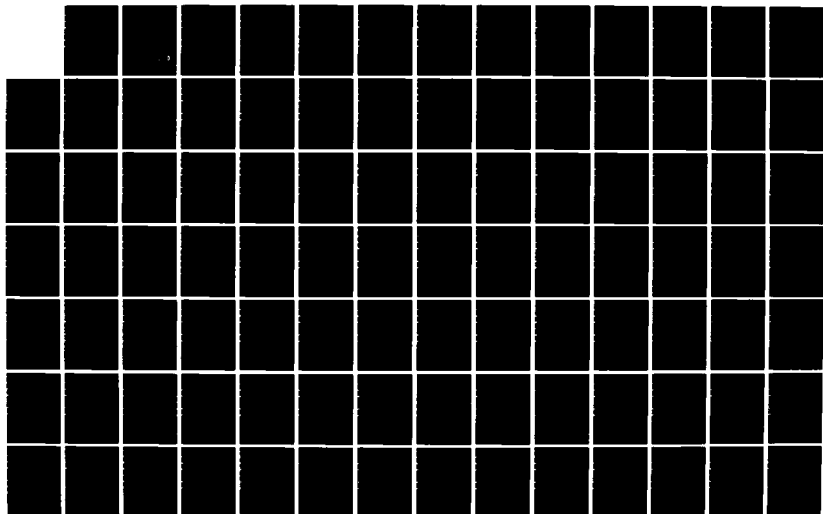
ADVANCED CONCEPTS THEORY ANNUAL REPORT 1984(U) NAVAL  
RESEARCH LAB WASHINGTON DC 26 JUN 85 NRL-MR-5590

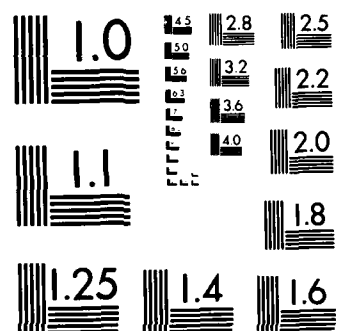
1/2

UNCLASSIFIED

F/G 20/9

NL





MICROCOPY RESOLUTION TEST CHART  
NBS-1963-A

7

NRL Memorandum Report 5590

# Advanced Concepts Theory Annual Report 1984

*Plasma Radiation Branch  
Plasma Physics Division*

AD-A157 535

June 26, 1985

This research was sponsored by the Defense Nuclear Agency under Subtask T99QMXLA,  
work unit 00019 and work unit title "Advanced Concepts."



DTIC  
SELECTED  
JUL 17 1985  
S D  
G

DTIC FILE COPY

NAVAL RESEARCH LABORATORY  
Washington, D.C.

Approved for public release; distribution unlimited.

002

SECURITY CLASSIFICATION OF THIS PAGE

REPORT DOCUMENTATION PAGE				
1a. REPORT SECURITY CLASSIFICATION <b>UNCLASSIFIED</b>		1b. RESTRICTIVE MARKINGS		
2a. SECURITY CLASSIFICATION AUTHORITY		3. DISTRIBUTION/AVAILABILITY OF REPORT <b>Approved for public release; distribution unlimited.</b>		
2b. DECLASSIFICATION/DOWNGRADING SCHEDULE				
4. PERFORMING ORGANIZATION REPORT NUMBER(S) <b>NRL Memorandum Report 5590</b>		5. MONITORING ORGANIZATION REPORT NUMBER(S)		
6a. NAME OF PERFORMING ORGANIZATION <b>Naval Research Laboratory</b>	6b. OFFICE SYMBOL (if applicable) <b>Code 4720</b>	7a. NAME OF MONITORING ORGANIZATION <b>Defense Nuclear Agency</b>		
6c. ADDRESS (City, State, and ZIP Code) <b>Washington, DC 20375-5000</b>		7b. ADDRESS (City, State, and ZIP Code) <b>Washington, DC 20375-5000</b>		
8a. NAME OF FUNDING/SPONSORING ORGANIZATION <b>Defense Nuclear Agency</b>	8b. OFFICE SYMBOL (if applicable) <b>RAEV</b>	9. PROCUREMENT INSTRUMENT IDENTIFICATION NUMBER		
8c. ADDRESS (City, State, and ZIP Code) <b>Washington, DC 20305</b>		10. SOURCE OF FUNDING NUMBERS		
		PROGRAM ELEMENT NO. <b>61725H</b>	PROJECT NO.	TASK NO. <b>DN880-191</b>
11. TITLE (Include Security Classification) <b>Advanced Concepts Theory Annual Report 1984</b>				
12. PERSONAL AUTHOR(S) <b>Plasma Radiation Branch</b>				
13a. TYPE OF REPORT <b>Annual</b>	13b. TIME COVERED FROM <b>1/84</b> TO <b>12/84</b>	14. DATE OF REPORT (Year, Month, Day) <b>1985 June 26</b>	15. PAGE COUNT <b>146</b>	
16. SUPPLEMENTARY NOTATION <b>This research was sponsored by the Defense Nuclear Agency under Subtask T99QMXLA, work unit 00019 and work unit title "Advanced Concepts."</b>				
17. COSATI CODES			18. SUBJECT TERMS (Continue on reverse if necessary and identify by block number)	
FIELD	GROUP	SUB-GROUP	Radiation Hydrodynamics	
			Plasma Mixtures	
19. ABSTRACT (Continue on reverse if necessary and identify by block number) <p>This volume of the Annual Final Report contains the results of a number of theoretical issues related to the radiative properties and x-ray conversion efficiency of dense hot plasmas. In particular, numerical simulations and analyses are presented for the radiative properties of gas puff mixtures, the dynamics of imploding gas puff plasmas, the implosion dynamics of stagnating gas puff plasmas, the influence of radiation on the velocity scaling of gas puff implosions and radiation from an ion beam target interaction.</p>				
20. DISTRIBUTION/AVAILABILITY OF ABSTRACT <input checked="" type="checkbox"/> UNCLASSIFIED UNLIMITED <input type="checkbox"/> SAME AS RPT <input type="checkbox"/> OTIC USERS			21. ABSTRACT SECURITY CLASSIFICATION <b>UNCLASSIFIED</b>	
22a. NAME OF RESPONSIBLE INDIVIDUAL <b>Jack Davis</b>			22b. TELEPHONE (Include Area Code) <b>(202) 767-3278</b>	22c. OFFICE SYMBOL <b>Code 4720</b>

DD FORM 1473, 84 MAR

93 APR edition may be used until exhausted  
All other editions are obsolete

SECURITY CLASSIFICATION OF THIS PAGE

## CONTENTS

PREFACE .....	iv
A. → RADIATIVE PROPERTIES OF PUFFED-GAS MIXTURES: OPTICALLY THIN CASE .....	1
B. → MODELING OF K-SHELL YIELDS .....	27
C. → DYNAMICS OF IMPLoding Z-PINCH .....	39
D. → IMPLOSION OF A NEON PUFF-GAS PLASMA ONTO A LOW-DENSITY PLASMA .....	63
E. → VELOCITY SCALING OF THE RADIATIVELY DOMINATED Z-PINCH .....	88
F. → ION-BEAM DEPOSITION, HEATING, AND RADIATION FROM AN ALUMINUM PLASMA .....	101

Accession For	
NTIS GRA&I	<input checked="" type="checkbox"/>
DTIC TAB	<input type="checkbox"/>
Unannounced	<input type="checkbox"/>
Justification	
By _____	
Distribution/ _____	
Availability Codes	
Dist	Avail and/or Special
A/1	



## Preface

During the past year the NRL Advanced Simulation Concepts Theory Program has focused on extending and improving the non-LTE equation of state data base, investigating the dynamics of imploding Z-pinchs, with and without a central plasma core, predicting the radiation from ion beam heated targets, developing a simple K-shell scaling law for conventional PRS loads, and the preparation of a pulse power primer for the beginner. The non-LTE equation of state work was devoted to studying the radiation enrichment of gas puff mixtures, i.e., determine whether it is possible to optimize the power radiated by a plasma comprised of two elements. Two cases were investigated: the optically thin and optically thick plasmas, respectively. For the optically thin investigation the plasma was composed of two elements of widely separated atomic number. The results suggest that the efficient radiation from lower shells of higher-Z elements require more powerful generators to attain the same conditions as higher shells of lower-Z loads. A not too surprising conclusion. However, it was shown that "spectral fill-in" can be obtained by mixtures using appropriate concentrations of complementary constituents, resulting in smoother photon distributions in the line spectrum. For the optically thick scenario the plasma was composed of two elements with adjacent atomic number. Under these conditions the results show convincingly that the K-shell emissivity of the plasma can be increased significantly over the conventional single-element load. The mechanism that increases the emissivity is that the opacity of each element is less, allowing more photons out - and twice as many lines are present in the K-shell region.

Numerical simulations were performed to provide guidance for the gas puff experiments conducted on the GAMBLE II facility and to determine the stability of plasma shells during the runin acceleration phase with Double-Eagle class generators. The GAMBLE II experiments were modeled with the 1-D radiation hydrodynamics simulation code, PRISM. The numerical simulations compared and contrasted the differences in code results with and without radiation transport and detailed atomic physics modeling. The code comparisons yield larger differences than those obtained from a comparison of the full model and the experimental results. The non-LTE numerical simulations were in particularly good agreement with the

experimental results. On the question of plasma stability during the run-in acceleration phase two issues were considered: first, the amount of shell mass participating in the unstable configuration and second, the magnitude of the growth rate of the instability and how it compares with the implosion time. It was determined that about 60% of the initial mass participates in the implosion to completion and although the back surface starts breaking-up, most of the mass remains stable and can become the source of intense radiation i.e., degradation of K-line radiation is only minimally influenced by the instability.

Another area of considerable interest is the examination of stagnating an imploding gas puff plasma onto a low density plasma for both radiation enhancement or for use as a fast switch. Application of plasma stagnation as a fast switch is currently being examined. For the purposes of this report the process of plasma stagnation is investigated as a source of radiation enhancement. The numerical simulations deal with the implosion of a neon gas puff onto a central neon core. The densities and temperatures at stagnation over interesting volumes and timescales are sufficient to suggest the efficient conversion of kinetic to thermal energy which is subsequently converted to radiation. About two-thirds of the total plasma energy was converted to K- and L-shell radiation in 100 nanoseconds.

Velocity scaling of a radiatively dominated Z-pinch was investigated using an electrodifusive model. Preliminary results show that the effect of the early radiation on the scaling error is most acute for the low current cases. However, the general trend is to reduce the pinch velocity and narrow the load width. A more extensive study is in progress.

Finally, an improved model for evaluating proton stopping power was developed and incorporated into the hydrodynamic response simulation code in place of the Local Oscillator Model (LOM). The new version incorporates the results of detailed theoretical calculations of proton stopping cross sections by Al ions from a Generalized Oscillator Strength treatment of the projectile target interaction. For neutral aluminum the agreement with the LOM result is good, but predicts smaller stopping power than LOM results for ionized Al, particularly at lower proton energies and higher charge states. These lower stopping powers result in deeper penetration into the

target by the proton beam, especially at early times. This causes the rear side to be hotter and less dense than if LOM stopping powers are used. At times of the order of a nanosecond, the rear side plasma emission is greater than the front side; when the LOM is used, the reverse situation occurs. Hence, the use of different stopping powers can result in marked differences in plasma emission spectra.

In addition to the work presented in this report there has been a number of reports on related activities. They include:

"Imploding Plasma Radiation Sources: Basic Concepts."

NRL Memo Rept. 5392 (July, 1984)

"K-Shell Yield Scaling Law for Conventional PRS Loads."

NRL Memo Rept. 5406 (Aug. 1984)

"Hydrodynamic Response of a Radiating Al Plasma Excited

by a Proton Beam." NRL Memo Rept. 5482 (Dec. 1984).

Copies of these reports are available on request.



## ADVANCED CONCEPTS THEORY ANNUAL REPORT 1984

### A. Radiative Properties of Puffed-Gas Mixtures: Optically Thin Case

#### I. INTRODUCTION

It has been a major goal of the plasma physics community in recent years to produce a high-fluence source of soft x-rays ( $h\nu > 1.0$  keV) in the laboratory. The applications of such a source are numerous: x-ray lithography, x-ray microscopy, extended x-ray absorption fine structure (EXAFS) studies, photon-pumped short-wavelength lasers, and x-ray vulnerability studies, to name a few examples. In the effort to construct such a source, several diverse experimental configurations have been successfully demonstrated, such as laser-target and ion beam-target interaction, synchrotrons, imploding foil liners, imploding wire arrays, and gas-puff Z-pinches. The last of these techniques<sup>1-16</sup> rely on high-voltage, pulse-power discharges through a plasma load, transforming the low-temperature material into an imploding annular plasma, accelerated radially by the current-driven, azimuthal magnetic field to velocities near  $10^7$  cm/sec. The on-axis assembly of the imploding plasma results in thermalization of the kinetic energy driving it and the subsequent emission of copious radiation in the soft x-ray band. Due to the electrical characteristics of these machines (e.g., attainable peak voltage and current, impedance, inductance, and pulse width), much time and effort has been invested in matching the appropriate load (be it a foil, wires or gas-puff) to the generator in order to optimize x-ray emission in the desired wavelength regions. One proposed method of enhancing the x-ray yield (as well as broadening the spectral region where emission occurs) is to replace single-material loads with mixtures. Although little work has been devoted to study this proposed technique,<sup>17</sup> it has been suggested that by combining materials of low and high atomic number, an increase in either the plasma temperature or density (or both) during the x-ray emission phase would be realized, as compared to that of purely the higher-Z material implosion. Since the desired soft x-ray emission scales nearly as  $N_I^2$  and up to  $T_e^4$  in certain regimes ( $N_I$  and  $T_e$  being plasma ion density and electron temperature), it is hoped that the increase in these parameters would yield an increment in radiation which would exceed that which was lost by the use

Manuscript approved March 26, 1985.

of a lower concentration of the higher-Z material, thereby enhancing the radiative output.

In this study, a theoretical investigation of the radiative properties of multi-material gas-puff Z-pinch plasmas is described. The primary tool used in this study is a numerical model of plasma ionization/radiation with the newly-developed capability of treating multi-material plasmas simultaneously and self-consistently. The model, which is discussed below in more detail, is based on a solution of a set of atomic rate equations characterizing a plasma in collisional-radiative equilibrium (CRE).<sup>18</sup> Parameter studies are presented for mixtures consisting of various concentrations of helium/argon, helium/krypton, neon/argon, and argon/krypton; the radiative yields are reported as a function of plasma temperature by maintaining a constant mass density of the mixture. In order to separate the purely collisional effects on the radiation enhancement from photon pumping processes, only optically thin plasmas are considered here. The cooperative effects of collisions, opacity and radiation transport will be studied in a paper to appear later.

## II. MODEL DESCRIPTION

### a. Ionization/Radiation Model

The basic ionization/radiation model has been discussed and documented in several previous publications<sup>19</sup> and only a brief description will be given here. A set of atomic rate equations of the form,

$$\frac{dN_i}{dt} = \sum_j W_{ji} N_j - \sum_j W_{ij} N_i \quad (1)$$

are solved for the ground and excited state population densities  $N_i$ , where  $W_{ij}$  is a collisional or radiative transition rate from state  $i$  to state  $j$ . The processes comprising  $W_{ij}$  used in this investigation include: collisional ionization, collisional, radiative, and dielectronic recombination, collisional excitation and deexcitation, and spontaneous radiative decay. As mentioned above, this study assumes the plasmas to be optically thin, hence, photoionization, photoexcitation and stimulated emission processes are neglected. The rate coefficients used to describe

the plasma atomic transitions are documented in the next section. Note that this is an investigation of the radiative properties of mixtures in equilibrium at some nominal electron temperature and ion density. The combined effects of the radiation and the magnetohydrodynamics (MHD) of the current-driven plasma mixture are a more complicated issue and will be addressed at a later time.

In order to treat the dual-component plasma mixture, the set of atomic rate equations for each material must be solved simultaneously, since the free electrons due to ionization of both materials are shared in the sense that any electron can collide with any ion. Thus, the electron density for a given temperature and fixed total mass density will lie between that of the pure lower-Z plasma and the pure higher-Z plasma, and is given by,

$$N_e = \sum_i Z_i N_i + \sum_i Z'_i N'_i \quad (2)$$

where  $Z_i$  and  $Z'_i$  are the charges of state  $i$  in material 1 and material 2 (of course, the level structure of each material employed in the model may be different). Since the electron density occurs in  $W_{ij}$  (via both 2-body and 3-body processes), the set of equations is highly non-linear and is solved numerically using an iterative predictor-corrector scheme.

The plasma radiative yield is comprised of emission via three atomic mechanisms: (i) line radiation from bound-bound transitions, (ii) recombination radiation from bound-free transitions, and (iii) bremsstrahlung emission via free-free interactions. At densities and temperatures typical of most plasma implosions on the largest pulse power generators presently configured for gas puffs ("BLACKJACK V" at Maxwell Laboratories, "PITHON" at Physics International, "SHIVA" at the Air Force Weapons Laboratory, "PROTO II" at Sandia Laboratories, and "GAMBLE II" at the Naval Research Laboratory), about 0.5-2.0 keV at  $\sim 10^{19}$  ions/cm<sup>3</sup>, the largest fraction of the total radiation is emitted as lines.<sup>20,21</sup> For this reason it is necessary to take into account all of the strong lines emitted in this temperature range to accurately determine the yield. The level structure employed to accomplish this is described below.

## o. Atomic Data

A critical factor affecting the integrity of a radiation calculation is both the accuracy and completeness of the data base used in the ionization/radiation calculation. This includes the level energies, rate coefficients and the number of excited levels of each ion that are retained in the model. This investigation included studies with the first four noble gases: helium, neon, argon, and krypton. Since they vary in atomic number from 2 to 36, and the temperature range of interest was held relatively constant, different level structure was required for each material. Helium was assumed to be fully ionized at temperatures above 100 eV and, hence, only the bare nucleus and two free electrons are free to interact. No detailed level structure was therefore needed for helium. Neon will most likely be stripped of its L-shell electrons above 100 eV, hence, excited level structure was retained for the lithiumlike, heliumlike, and hydrogenlike ions. Argon will have lost its M-shell electrons at 100 eV,<sup>14</sup> so structure was included for Ar IX-Ar XVIII (neonlike through hydrogenlike). Krypton, on the other hand will not be stripped down to the L-shell electrons until about 1.0 keV.<sup>20</sup> Since at present we have modeled the excited level structure in krypton only down to Kr XXVI (sodiumlike ion) we cannot conduct meaningful calculations of total radiative yield below temperatures of 500 eV. However, for our purposes, we are predominantly interested in photon emission above a kilovolt; since the M-shell ions emit lines below about 900 eV and L-shell ions emit most lines ( $\Delta n \geq 1$ ) above 1.6 keV, all of the relevant line emission is included in the model. A list of the energy levels included in the model is given in Table I; the same structure was used for both argon and krypton, while only the 1-, 2-, and 3-electron systems apply to neon. All ground states were included for each of the three materials.

The level energies and radiative decay coefficients for the level structure in Table I were calculated using the Hartree-Slater atomic structure model written by R. Cowan.<sup>22</sup> Since this code provides information for individual j-levels, significant averaging over j (and oftentimes l) was necessary to obtain energies and Einstein-A coefficients for the structure given in Table I. Electron impact excitation is calculated by a number of techniques and a short discussion of these

follows. In the case of krypton, a complete set of collision strengths calculated by Bhatia and Feldman<sup>23</sup> in the distorted wave approximation were used to generate the rate coefficients for the  $\Delta n=0$  transitions in L-shell ions. The rate coefficients for K-shell and lithiumlike transitions in argon were calculated using the method of distorted waves described by Blaha,<sup>24</sup> while those for neon and krypton were calculated using the Coulomb-Born scheme in intermediate coupling described by Sampson and co-workers.<sup>25</sup> The screening constants (both direct and exchange contributions) used in this calculation were obtained via direct comparisons with the argon distorted wave results. The transitions coupling the  $n=1$  and  $n=2$  levels in the heliumlike ions of neon and argon were taken from the results of Pradhan et al.<sup>26</sup> which include the effects of autoionizing resonances. The rates for sodiumlike krypton were taken from the distorted wave calculations of Blaha and Davis,<sup>27</sup> while those for neonlike krypton have been calculated by Reed and Hazi.<sup>28</sup> Rate coefficients for carbonlike, boronlike, and berylliumlike argon were also calculated using Blaha's distorted wave model. All other rate coefficients not obtainable by more sophisticated means were calculated using a code developed by Davis<sup>29</sup> based on the semi-classical impact parameter technique; the oscillator strengths calculated using the atomic structure code were used as the input, and bound-bound Gaunt factors were calculated directly. The rate coefficients for the remaining collisional processes are identical to those used in previous investigations and the details of the calculational methods can be found by consulting Ref. 18.

### III. RESULTS

#### a. Density Scaling

As was stated earlier, no attempt was made to account for the dynamics of the imploding plasma in this study, hence, the radiation/ionization calculation took electron temperature and the density of each constituent as input variables. In this sense, the predicted radiative yields in a given spectral range are representative of only the hottest, most dense part of the pinched plasma, along the axis of the initial gas annulus. Previous MHD simulations<sup>30</sup> indicate that surrounding the hotter

plasma are colder, less dense plasma regions characterized by large temperature gradients. Since the ions found in these cooler regions emit radiation at frequencies below the range of interest here, it will suffice to neglect these regions and treat only the hotter plasma. The peak electron temperatures attained in these plasmas usually vary according to the size of the pulse power generator and the initial gas pressure. However, the range of interest is typically between 300 eV and 2.5 keV, therefore, we limited our parameter study to this region.

Four different gas mixtures were studied for radiation enhancement: neon/argon, argon/krypton, helium/argon, and helium/krypton. The spectral ranges of interest were above 900 eV for neon (K-shell emission), above 3.0 keV for argon (K-shell emission), and above 1.5 keV for krypton (L-shell emission). Helium emits only low-fluence bremsstrahlung in these spectral ranges and was therefore neglected in the yield analysis. We conducted the parameter study by varying the concentration of the gases in each mixture for a number of relevant temperatures. The present level of understanding of gas-puff implosions dictates that when varying the concentrations of the mixture gases, one should hold the total mass density of the mixture constant in order to make fair comparisons of the yield. In this way, as the concentrations vary, the same mass will be accelerated, presumably attaining the same temperature at assembly. Thus the ion density of constituent 1 is given by

$$N_1 = \frac{m_v}{A_1 + A_2 \left( \frac{1-\alpha}{\alpha} \right)} \quad (3)$$

and that of constituent 2 by

$$N_2 = \frac{m_v}{A_1 \left( \frac{\alpha}{1-\alpha} \right) + A_2} \quad (4)$$

where  $m_v$  is the mass density in amu/cm<sup>3</sup>,  $A_1$  and  $A_2$  are the atomic weights of the constituents and  $\alpha$  is the ion number concentration of constituent 1 ( $\alpha = N_1 / (N_1 + N_2)$ ). The mass density was held fixed at  $2 \times 10^{20}$  amu/cm<sup>3</sup> which is commensurate with a density of  $10^{19}$  ions/cm<sup>3</sup> for a pure neon plasma. This corresponds approximately to the densities determined from spectral analysis of K-shell emission on the Blackjack V machine, although

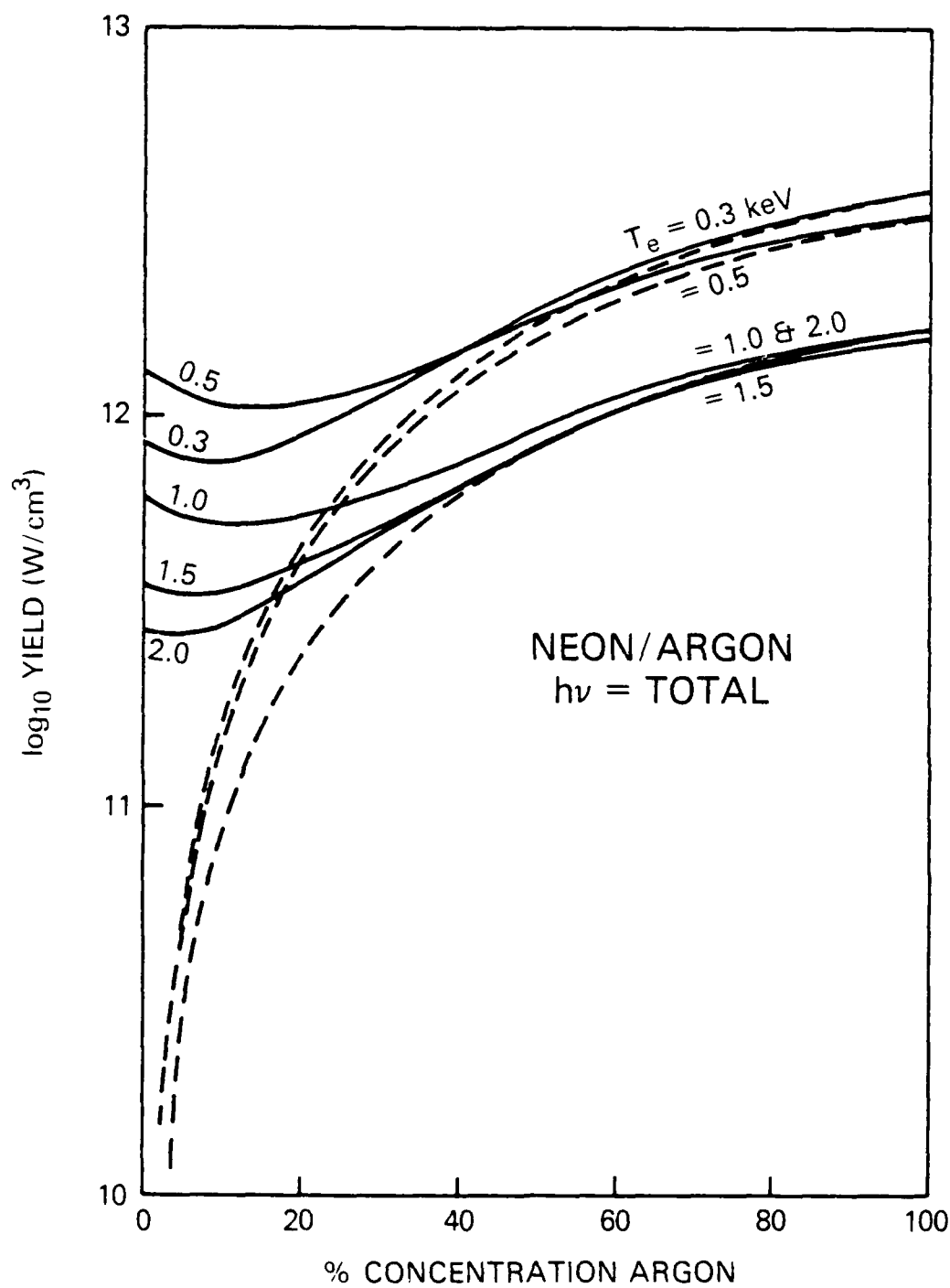


Fig. 4. Total radiation versus argon concentration for neon/argon mixtures; solid curves are argon + neon, broken curves are the argon alone.

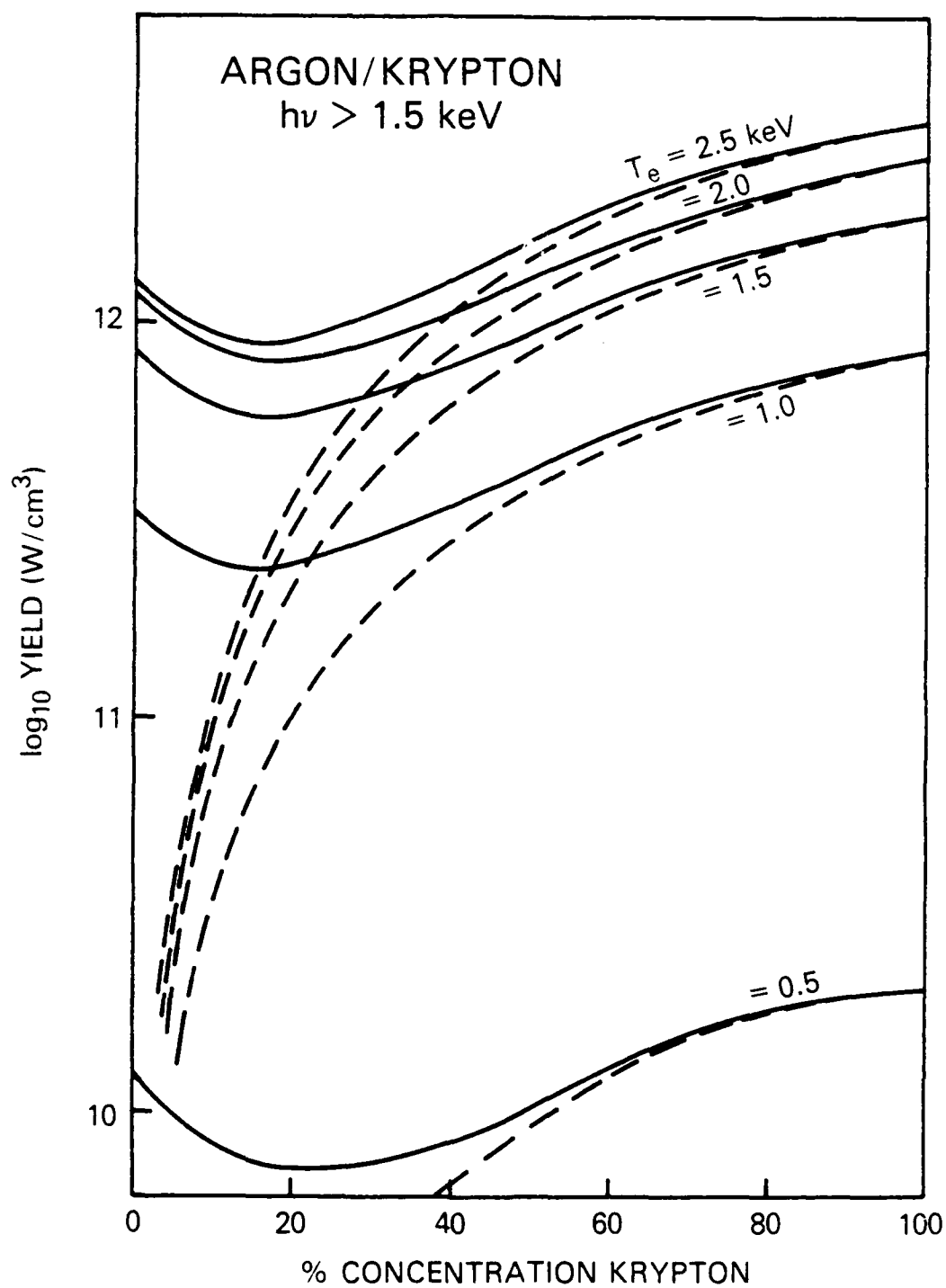


Fig. 3. Line radiation yield ( $h\nu > 1.5 \text{ keV}$ ) versus krypton concentration for argon/krypton mixtures; solid curves are argon + krypton, broken curves are the krypton contribution.



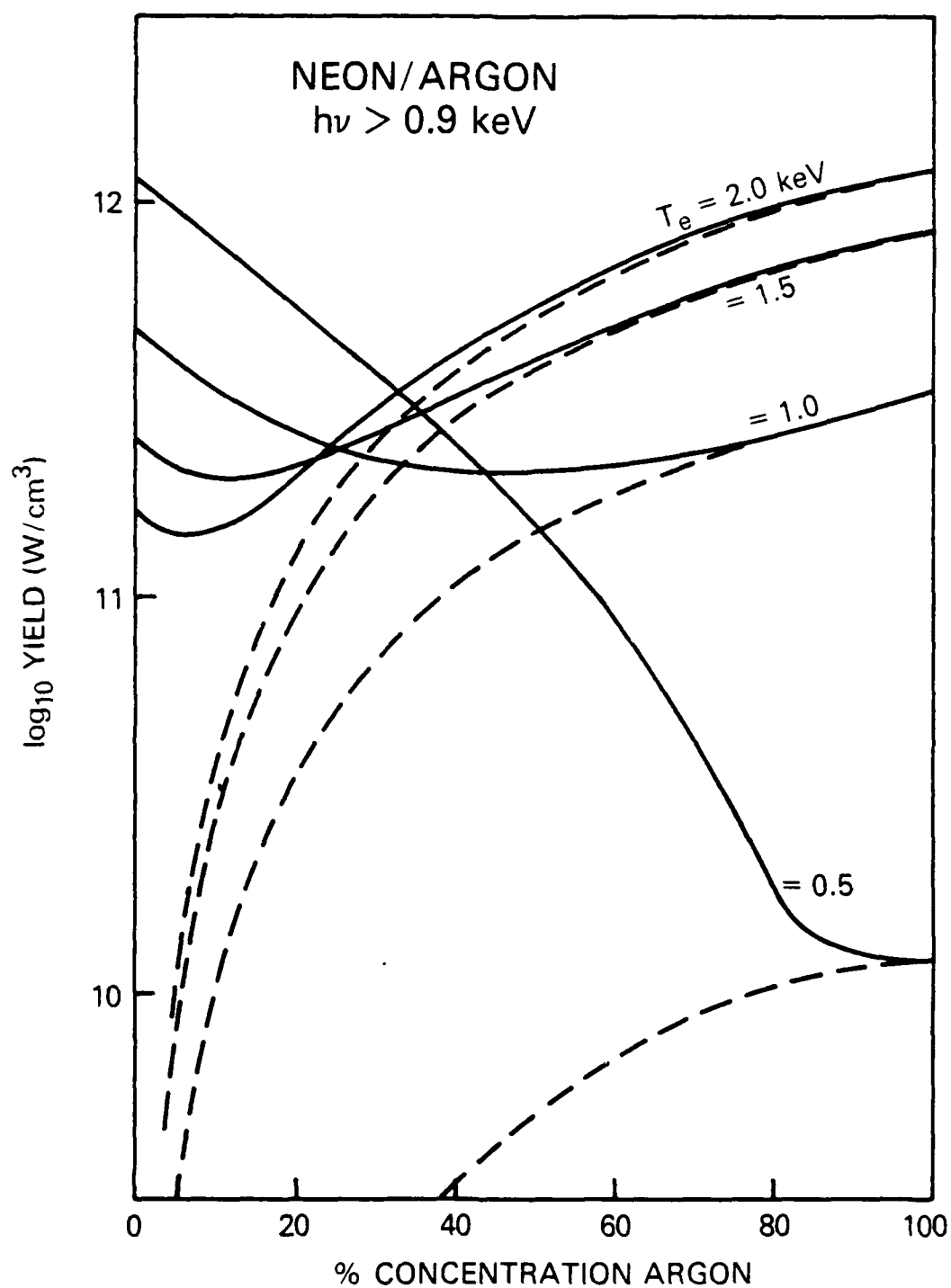


Fig. 2. Line radiation yield ( $h\nu > 0.9 \text{ keV}$ ) versus argon concentration for neon/argon mixtures; solid curves are argon + neon, broken curves are the argon contribution.

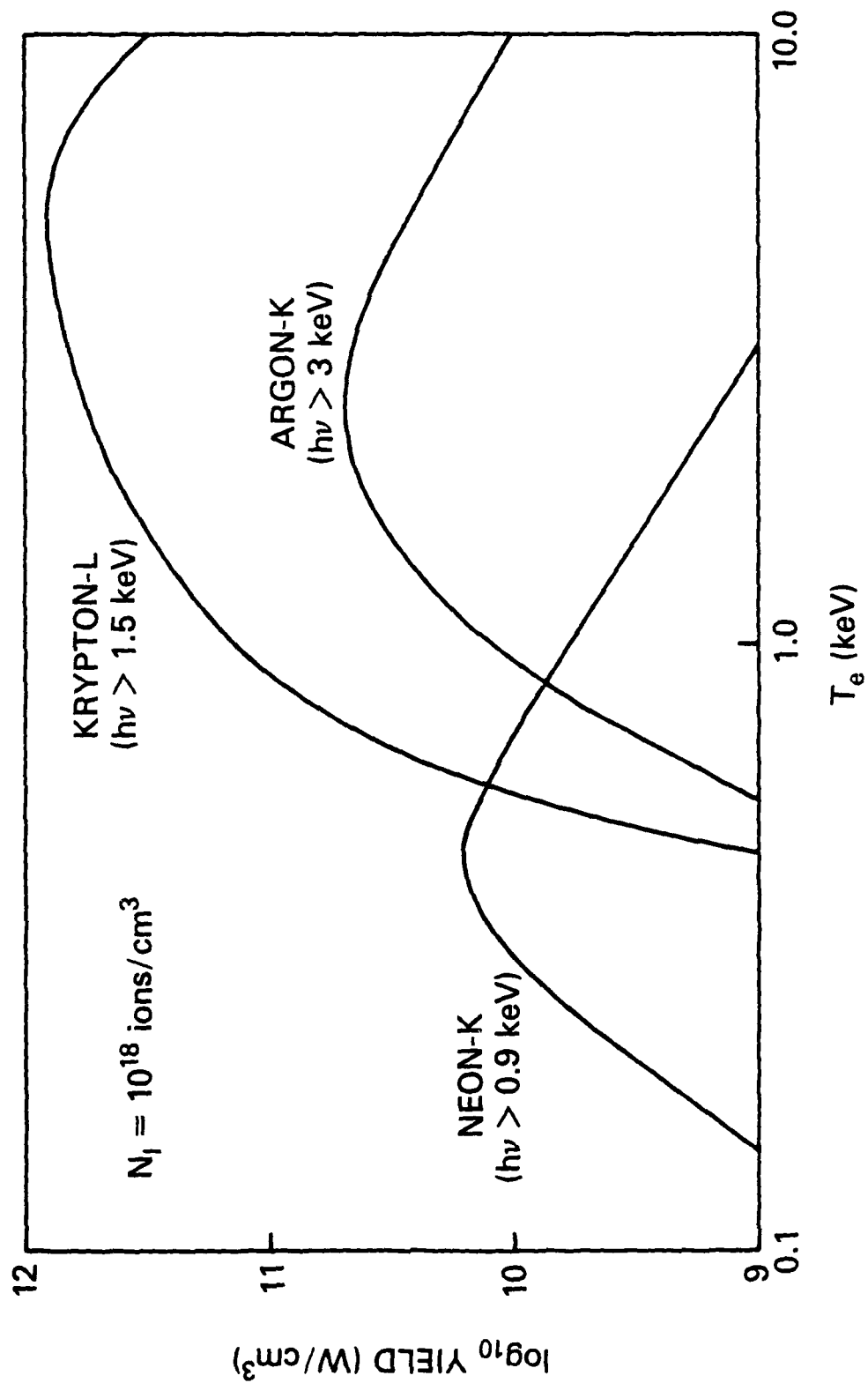


Fig. 1. Line radiation yield versus electron temperature for neon K-lines, argon K-lines, and krypton L-lines at a density of  $10^{18}$  ions/cm<sup>3</sup> (optically thin).

Table II — Ion densities corresponding to the concentrations used in the mixture studies.  
Units are  $\times 10^{18}$  ions/cm<sup>3</sup>.

CONCENTRATION OF THE HIGHER Z CONSTITUENT (1 -  $\alpha$ )

Mixture	0%	5%	10%	20%	50%	100%
# 1 Neon	10.0	9.05	8.18	6.67	3.33	0.00
Argon	0.00	0.476	0.909	1.67	3.33	5.00
# 2 Argon	5.00	4.50	4.05	3.28	1.61	0.00
Krypton	0.00	0.237	0.450	0.820	1.61	2.38
# 3 Helium	50.0	32.8	23.7	14.3	4.55	0.00
Argon	0.00	1.72	2.63	3.57	4.55	5.00
# 4 Helium	50.0	23.8	15.0	8.00	2.27	0.00
Krypton	0.00	1.25	1.67	2.00	2.27	2.38

Table I (Cont'd) — Atomic level structure used in the ionization/radiation model for neon, argon, and krypton (only the krypton model has Na-like excited levels).

<u>Li-like</u>	
$1s^2 2s$	2
2p	6
3s	2
3p	6
3d	10
4 $\ell$	32
5 $\ell$	50

<u>He-like</u>	
$1s^2 (^1S)$	1
$1s2s (^3S)$	3
$1s2s (^1S)$	1
$1s2p (^3P)$	9
$1s2p (^1P)$	3
$1s3\ell (^3L)$	27
$1s3\ell (^1L)$	9
$1s4\ell$	64
$1s5\ell$	100

<u>H-like</u>	
1s	2
2 $\ell$	8
3 $\ell$	18
4 $\ell$	32
5 $\ell$	50

Table I (Cont'd) — Atomic level structure used in the ionization/radiation model for neon, argon, and krypton (only the krypton model has Na-like excited levels).

N-like		B-like	
$1s^2 2s^2 2p^3 (^4S_{3/2})$	4	$1s^2 2s^2 2p (^2P_{1/2})$	2
$2s^2 2p^3 (^2D)(^2P_{1/2})$	12	$2s^2 2p (^2P_{3/2})$	4
$2s^2 2p^3 (^2P_{3/2})$	4	$2s 2p^2 (^4P)$	12
$2s 2p^4 (^4P)$	12	$2s 2p^2 (^2D)(^2P_{1/2})$	12
$2s 2p^4 (^2D)$	10	$2s 2p^2 (^2S)(^2P_{3/2})$	6
$2s 2p^4 (^2S_{1/2})(^2P_{3/2})$	6	$2p^3 (^4S)$	4
$2s 2p^4 (^2P_{1/2})$	2	$2p^3 (^2D)(^2P_{1/2})$	12
$2p^5 (^2P)$	6	$2p^3 (^2P_{3/2})$	4
$2s^2 2p^2 3\ell$	270	$2s^2 3\ell$	18
$2s 2p^3 3\ell$	720	$2s 2p(1/2) 3\ell$	82
$2s^2 2p^2 4\ell$	480	$2s 2p(3/2) 3\ell$	134
$2s 2p^3 4\ell$	1280	$2s^2 4\ell$	32
		$2s 2p 4\ell$	384
C-like		Be-like	
$1s^2 2s^2 2p^2 (^3P_0)$	1	$1s^2 2s^2 (^1S_0)$	1
$2s^2 2p^2 (^3P_1)(^1D_2)$	8	$2s 2p (^3P)$	9
$2s^2 2p^2 (^3P_2)(^1S_0)$	6	$2s 2p (^1P_1)$	3
$2s 2p^3 (^5S_2)$	5	$2p^2 (^3P_0)$	1
$2s 2p^3 (^3D)$	15	$2p^2 (^3P_1)(^1D_2)$	8
$2s 2p^3 (^3P_{0,1})(^1D)(^3S)$	12	$2p^2 (^3P_2)(^1S_0)$	6
$2s 2p^3 (^3P_2)(^1P_1)$	8	$2s 3s/3p$	16
$2p^4 (^3P_{0,2})$	6	$2s 3d$	20
$2p^4 (^3P_1)(^1D_2)$	8	$2p(1/2) 3\ell$	44
$2p^4 (^1S_0)$	1	$2p(3/2) 3\ell$	64
$2s^2 2p 3\ell$	108	$2s 4\ell$	36
$2s 2p^2 3\ell$	540	$2p 4\ell$	192
$2s^2 2p 4\ell$	192		
$2s 2p^2 4\ell$	960		

Table I — Atomic level structure used in the ionization/radiation model for neon, argon, and krypton (only the krypton model has Na-like excited levels).

		F-like	
Na-like			
$1s^2 2s^2 2p^6 3s$	2	$1s^2 2s^2 2p^5 (^2P)$	6
3p	6	$2s^2 2p^6 (^2S)$	2
3d	10	$2s^2 2p^4 3s$	30
4s	2	$2s^2 2p^4 3p$	90
4p	6	$2s^2 2p^4 3d$	150
4d	10	$2s^2 2p^5 3s$	24
4f	14	$2s^2 2p^5 3p$	72
5l	50	$2s^2 2p^5 3d$	120
6l	72	$2s^2 2p^4 4l$	480
		$2s^2 2p^5 4l$	384
		$2s^2 2p^4 5l$	1350
		$2s^2 2p^5 5l$	
		$2s^2 2p^4 6l$	1944
		$2s^2 2p^5 6l$	
Ne-like		O-like	
$1s^2 2s^2 2p^6 (^1S)$	1	$1s^2 2s^2 2p^4 (^3P_2)(^1S_0)$	6
$2s^2 2p^5 3s (3/2)$	8	$2s^2 2p^4 (^3P_1)(^1D_2)$	8
$2s^2 2p^5 3s (1/2)$	4	$2s^2 2p^4 (^3P_0)$	1
$2s^2 2p^5 3p (3/2)$	24	$2s^2 2p^5 (^3P)$	9
$2s^2 2p^5 3p (1/2)$	12	$2s^2 2p^5 (^1P_1)$	3
$2s^2 2p^5 3d (3/2)$	40	$2p^6 (^1S_0)$	1
$2s^2 2p^5 3d (1/2)$	20	$2s^2 2p^3 3l$	360
$2s^2 2p^6 3s$	4	$2s^2 2p^3 3l$	270
$2s^2 2p^6 3p$	12	$2s^2 2p^3 4l$	640
$2s^2 2p^6 3d$	20	$2s^2 2p^4 4l$	480
$2s^2 2p^5 4l$	192		
$2s^2 2p^5 5l$	300		
$2s^2 2p^5 6l$	432		

$$E_T = \frac{3}{2} (1 + Z) N_I kT_e \quad (5)$$

Because the average  $Z$  for reaching the krypton L-shell (26) is greater than that for argon K-shell (16), more energy is required to attain the same temperature. Second, some of the kinetic energy is converted to potential energy via ionization of the plasma ions to the appropriate electron shell. To reach the argon K-shell requires only about 5.9 keV/ion of ionization energy, while to ionize krypton to the L-shell requires 12.65 keV/ion. Third, it has been shown<sup>31</sup> that to effectively "burn through" an electron shell is not a simple matter of supplying enough energy for ionization. Collisional excitations and radiative decay occur on a time scale several orders of magnitude faster than collisional ionization; hence, radiation loss during the ionization phase must be taken into account, and the actual energy required is given by

$$E = E_I + \sum_Z \int P_R^Z (T_e(t)) dt \quad (6)$$

where  $E_I$  is ionization energy and  $P_R^Z$  is the radiation loss of ion  $z$ . Just as the radiative cooling rate for the krypton L-shell exceeds that of the argon K-shell, (see Fig. 1) the krypton M-shell cooling rate exceeds that of the argon L-shell. Thus, efficient radiation from the lower shells of higher- $Z$  materials may necessarily require more powerful generators to attain the same conditions as higher shells of lower- $Z$  loads.

Finally, it was shown that "spectral fill-in" can be obtained by mixtures using appropriate concentrations of complementary constituents, resulting in smoother photon distributions in the line spectrum. However, it may be necessary to carefully tailor the temperature gradient in the dense plasma to allow all the relevant ions to contribute to the broadband emission spectrum.

continuous line emission from 0.9 to 4.0 keV. In fact, at plasma temperatures below 600 eV, the argon L- and krypton M-shell emission would fill in the spectrum below 0.8 keV, as well; it would take very careful tailoring of the load and generator characteristics, however, to maintain an imploded plasma with a temperature gradient ranging from a few hundred electron volts up to 2.5 keV!

#### IV. CONCLUSIONS

An investigation of the radiative yield of puffed-gas mixtures has been initiated in which the temperature and concentration effects have been studied. The main result of the simulations is that the yield of the mixtures is always less than one can obtain by using one or the other of the constituents in pure form. Consequently, the only hope of producing enhanced emission via this approach would be if the plasma mixture attained a higher temperature, higher density, or increased mass participation than that obtainable from the pure constituents (earlier experiments on a lower-power machine have indicated some evidence of temperature enhancement using mixtures). Although that study is the next step in our investigation of radiation enhancement, and requires a combined radiation/hydrodynamics model to characterize the plasma dynamics, some general statements can be made regarding the radiative performance of the load.

Essentially, the goal of maximizing the photon yield is attained by efficient conversion of kinetic energy of the imploding plasma to radiation. In general, the hotter and denser the plasma becomes the greater will be the yield, although the temperature dependence is subject to the problem of burn-through of the atomic shell structure. This is easily overcome, however, by going to higher Z materials. In fact, it has often been suggested that one can obtain more emission in, for example, the  $h\nu > 1.5$  keV range by going to the krypton L-shell as opposed to the argon K-shell. From Fig. 1 it is obvious that if the plasmas can be made to implode to the same temperatures, densities, and sizes, the krypton plasma radiates at a much higher power level than argon. However, to obtain the same conditions in both plasmas requires more energy for krypton since a number of obstacles must be overcome. First, some of the plasma kinetic energy is converted to thermal energy.



significantly harder in the mixture than in the pure krypton case. Presumably, one could then infer that much higher temperatures were attained in the mixture than in pure krypton. Due to the low concentration, the krypton ion density was down from  $3.5 \times 10^{19} \text{ cm}^{-3}$  in pure krypton to  $2.7 \times 10^{17}$  in the mixture, and, hence, so was the total yield, from about 250 Joules down to 110 Joules (most of the photons were of  $h\nu < 400 \text{ eV}$ ). The interesting question that emerges is whether significant temperature increases can still be maintained at krypton concentrations of 5% or greater. As seen in Fig. 6, if the plasma temperature is below 1.0 keV, an increase of only 100 eV can greatly enhance the yield of photons above 1.5 keV. Thus, smaller generators may be able to enhance the production of krypton L-shell lines by using helium/krypton mixtures. The same situation would apply to argon K-lines (see Fig. 5) if the temperature enhancement was evident in mixtures of helium/argon.

#### c. Spectral Enhancement

Another advantage of using gas-puff loads comprised of mixture is the so-called "spectral fill-in" phenomenon. By clever choice of complementary constituents, the natural "gaps" between different electron shell emissions that appear in the line-dominated spectra of imploded Z-pinch plasmas can be eliminated. This produces a smoother distribution of photon energy over a given frequency range which is advantageous for a number of applications of the radiation source. Note, for example, the way the L-shell emission from krypton and the K-shell emission from argon combine in Fig. 7 to provide almost continuous line emission from 1.6 keV to 4.0 keV. The spectrum in Fig. 7 was generated by assuming a steady-state temperature profile from 1.0 to 2.5 keV exists in the puffed-gas implosion. This is a necessary requirement in order to obtain radiation from all eight ions in the krypton L-shell; the two argon K-shell ions, on the other hand, radiate over a wide temperature range (see Fig. 1). Similarly, in Fig. 8, a neon/krypton mixture can be used to obtain line emission from 0.9 keV up to 2.8 keV with the appropriate concentration and temperature conditions (approximately 10:1 neon to krypton at about 1 keV). Conceivably, one could mix neon, argon, and krypton to obtain

of higher temperature or higher density, or more mass to participate in the implosion as compared to the pure substances. These possibilities will be discussed in more detail in the next section.

Although the main emphasis here has been on photon energies above a kilovolt, for the sake of completeness, the total yield is shown in Fig. 4 for neon/argon mixtures. Again, the total is the solid lines while the broken curves represent the argon emission. Qualitatively, Figs. 2 and 4 and very similar in their behavior. Quantitatively, we see that the lower temperatures produce more argon yield than the higher ones up to 2 keV, where the K-shell emission begins to peak (see Fig. 1). This is due simply to the fact that, at this density, the L-shell of argon is a more efficient radiator than the K-shell (see Ref. 18 for a complete discussion of L- and K-shell competition for photon production as a function of density).

The last two mixtures studied were helium/argon and helium/krypton. The results of these mixed loads are shown in Figs. 5 and 6; here, the solid lines represent the total radiation from the higher-Z constituent while the broken lines indicate the soft x-ray component (no helium emission is shown since that constituent is fully ionized). Since helium is such a light ion, the total mass of the mixture is almost all due to the higher-Z material at even rather low concentrations (see Table II). Thus, the yield curves rise quickly in Figs. 5 and 6 to values approaching the maximum at concentrations of only 20%. In fact, only a 5% concentration of the higher-Z constituent gives a yield which is down by only a factor of two from the maximum. Once again, the same message is communicated by the graphs: no radiation enhancement is possible over that of the pure gas load by using a helium mixture unless the lower concentrations can be imploded to higher density or higher temperature.

In an experiment on a smaller generator (5 kJ at 30 kV), Bailey<sup>17</sup> reported on yield measurements for pure helium, helium/krypton mixtures, and pure krypton where the ion number concentration of krypton was kept at 1.5% for the mixture. The most significant observation was a large increase in the total emission over that of pure helium. Measured electron densities were about  $10^{20} \text{ cm}^{-3}$ , five times that of pure helium, and the minimum radius about a factor of two smaller. Also, it was determined that the average ionization stage was higher and the radiation spectrum

yields shown in Fig. 1 scale with density approximately as  $N_I^2$  since the relevant ion ground states are close to coronal equilibrium at the densities commonly encountered in gas-puff Z-pinches. Note that while the argon K-shell and krypton L-shell line emission are both near their maxima in the temperature range of 2-6 keV, the neon and argon will not emit strongly together at the same temperature in the photon energy region of interest, intimating that argon/krypton mixtures may be better radiators. On the other hand, based on past performance of the large pulse power generators, it is not clear that plasma loads can be heated in bulk to temperatures much above 2 keV. Thus, actual radiative performance of the two mixtures may not differ significantly in actual machine conditions.

Considering now the radiative output of the mixtures, the results are presented as the yield (in the relevant photon range) as a function of ion number concentration of the higher-Z constituent for several temperatures spanning the operational range of the machines. The results of the neon/argon study are shown in Fig. 2 for  $h\nu > 0.9$  keV; the solid lines are the neon plus argon output while the output of argon alone is depicted by the broken lines (thus, both curves at the same temperature merge at 100% argon concentration). In Fig. 2, it is shown that the neon radiation falls off above 500 eV; this explains the behavior of the yield with temperature at 0% concentration of argon. Conversely, argon yield rises with temperature above 500 eV, explaining the cross-over of the solid curves. As expected the argon emission rises rapidly with concentration and asymptotes with the neon + argon curve. The main point to be emphasized from Fig. 2, however, is that no possible mixture of the two constituents results in a soft x-ray yield which exceeds the larger of the two pure yields. Stating it another way, under the assumption that all loads of a fixed mass of two constituents will implode to the same temperatures, there appears to be no way to enhance the yield of a load by using mixtures above that which could be obtained from one or the other of the pure substances. This conclusion is verified in Fig. 3 for argon/krypton mixtures (with  $h\nu > 1.5$  keV), where very similar behavior of the yield with concentration is seen. This is a rather unexpected result from the point of view of radiation enhancement of superkilovolt photons using mixed loads. Of course, the gas mixture may still be shown to affect the implosion dynamics in a positive way, such as allowing either an attainment

densities of  $2-5 \times 10^{19}$  are not uncommon for high-yield shots. Having fixed the total mass density, the actual ion densities used in the calculation are given in Table II for the concentrations analyzed.

At this point, it may be worthwhile to point out that this strategy of parameter variation may differ from actual experimental procedures. In the laboratory it is common to obtain cylinders of gas mixtures at fixed concentrations, and, by varying the diaphragm diameter on the fast-opening valve of the gas-puff nozzle, study the radiation yield as a function of initial mass density. The reason for not adopting this technique is due to our stationary equilibrium model. Varying the initial mass of the load will likely alter the implosion dynamics and, hence, the final temperature and density. Thus, a meaningful calculation of the load performance would require complete modeling of the flow effects which is beyond the intent of this paper. However, we plan to eventually couple the radiation/ionization/mixture model to a 1-D MHD code for the purpose of assessing the cooperative radiative-hydrodynamic effects on radiation enhancement.

#### b. Radiative Yields

As was discussed in the previous section, the radiation output of the mixtures was calculated as a function of the electron temperature and constituent concentration for fixed mass density. Two radiative yield measurements are of interest: the total radiative output, and that above a spectral cutoff energy, 900 eV for neon, 1.6 keV for krypton, and 3.0 keV for argon. Thus, the yield above cutoff will be the spectral output at about a kilovolt and greater, since no strong krypton lines occur between 900 and 1600 eV and no strong argon lines occur between 900 and 3000 eV. Studies of radiation enhancement via mixtures at photon energies below 1.0 keV require different experimental configurations and are not considered in optimum conditions here. In order to acquaint the reader with the temperature variation of radiative yields for pure gases, the optically thin power densities for (a) neon K-lines ( $h\nu > 0.9$  keV), (b) argon K-lines ( $h\nu > 3.0$  keV), and (c) krypton L-lines ( $h\nu > 1.6$  keV) are shown in Fig. 1 for a fixed density of  $10^{18}$  ions/cm<sup>3</sup>. This figure will be very useful in explaining the variation in yields from the mixture gases as the electron temperature of the mixture is increased. The line radiation

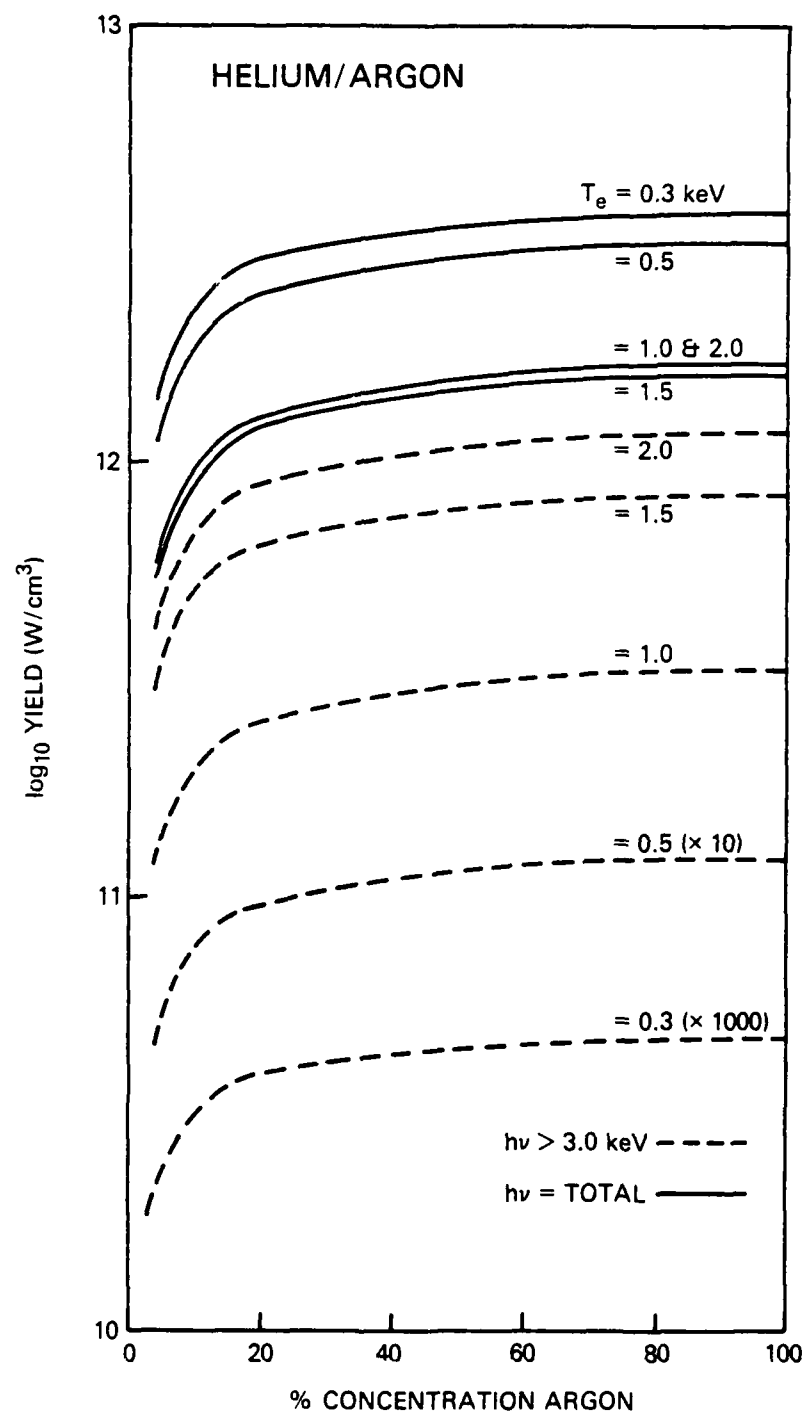


Fig. 5. Radiation yield versus argon concentration for helium/argon mixtures; solid curves are total radiation, broken curves are for  $h\nu > 3.0 \text{ keV}$ .

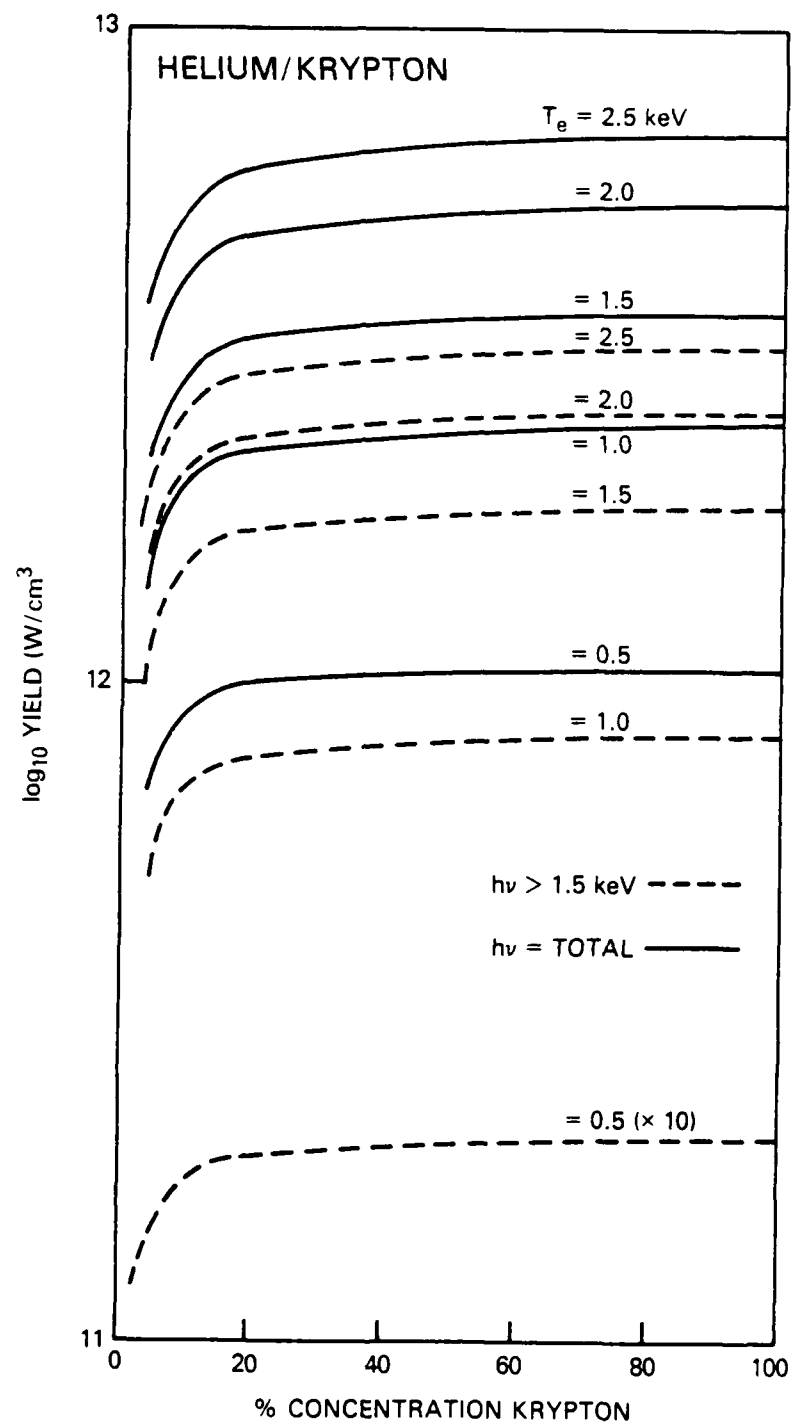


Fig. 6. Radiation yield versus krypton concentration for helium/krypton mixtures; solid curves are total radiation, broken curves are for  $h\nu > 1.5 \text{ keV}$ .

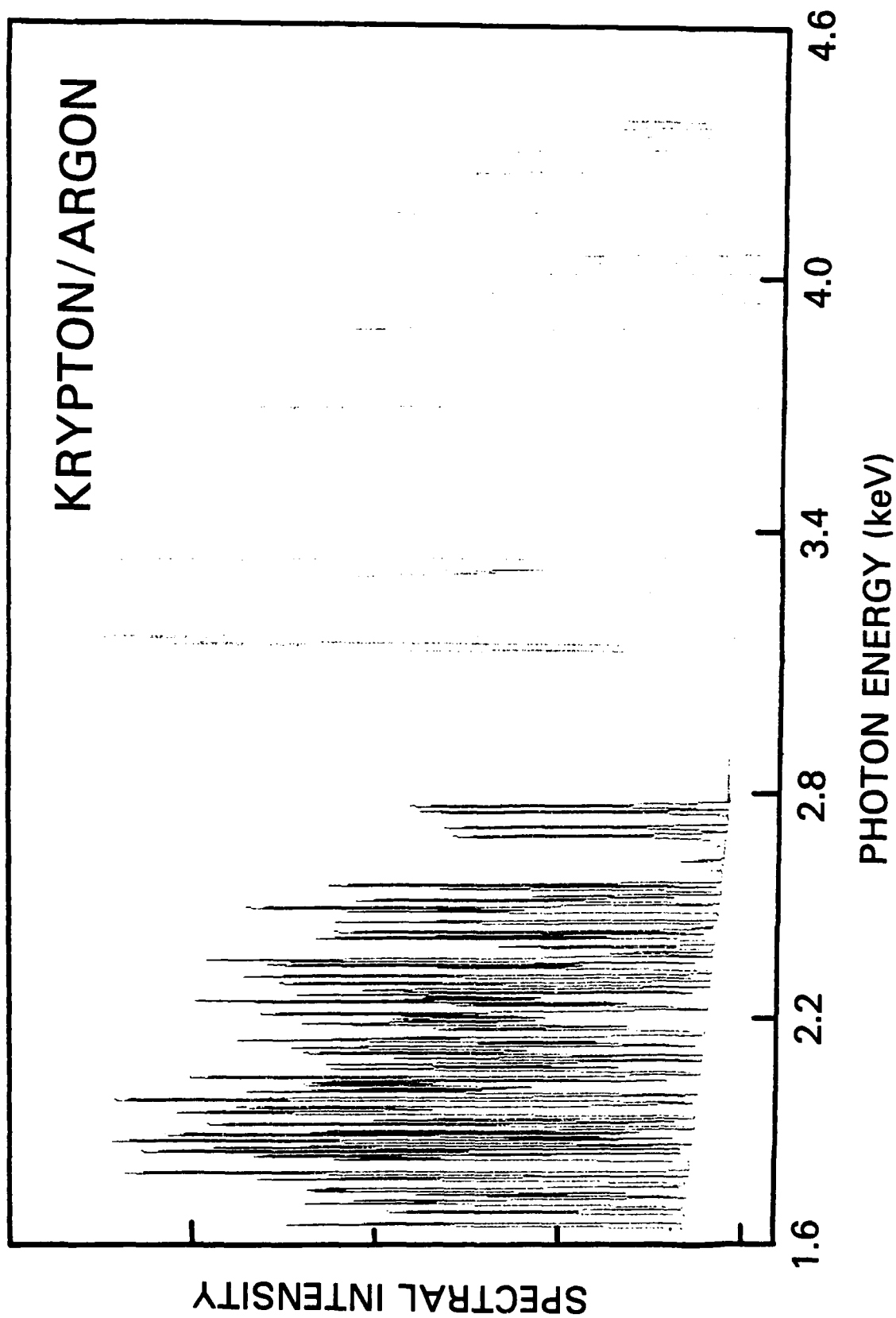


Fig. 7. Radiation spectrum resulting from an imploded argon/krypton mixture.

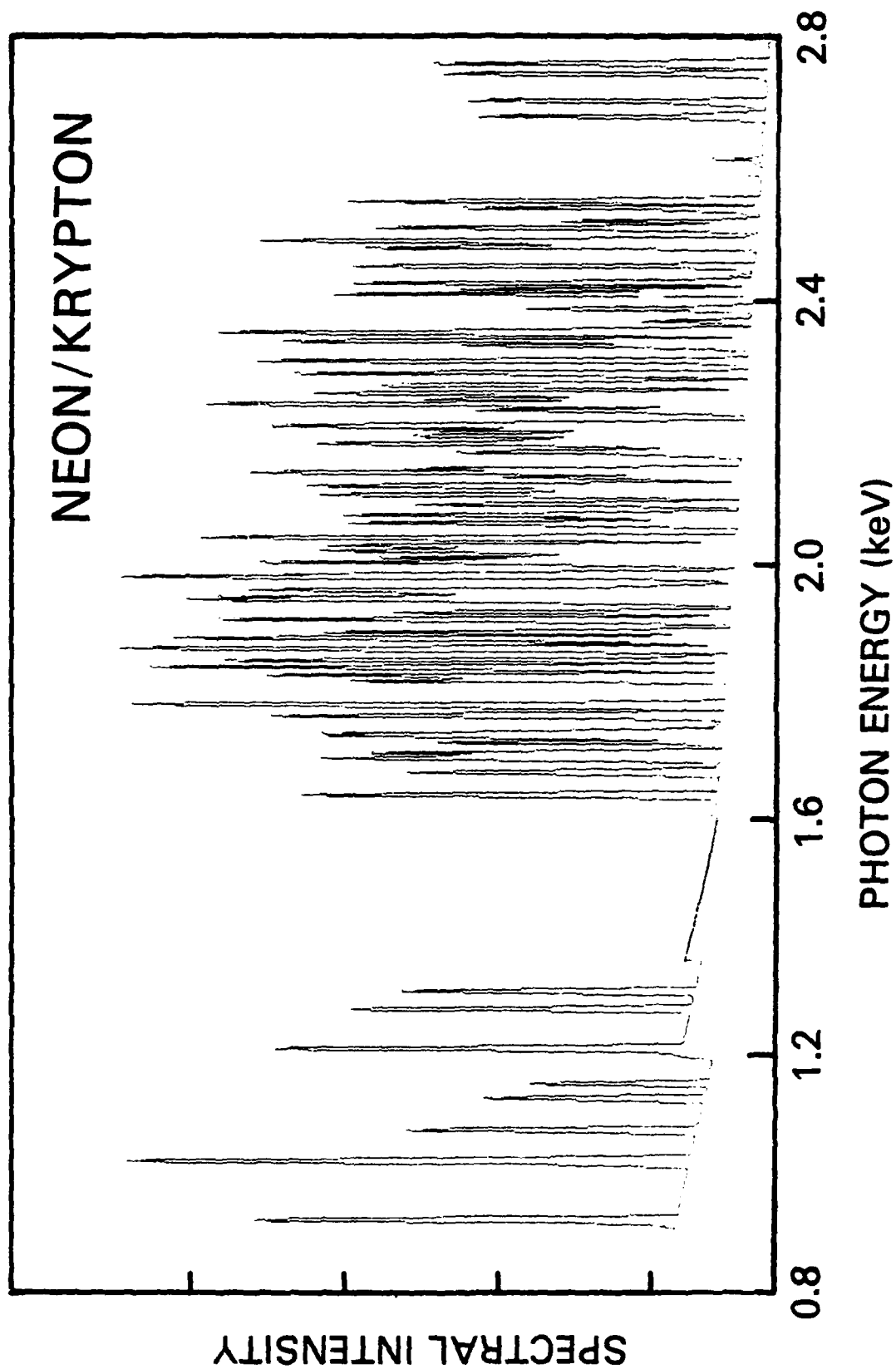


Fig. 8. Radiation spectrum resulting from an imploded neon/krypton mixture.



### References

1. P. G. Burkhalter, C. M. Dozier, and D. J. Nagel, Phys. Rev. A 15, 700 (1977).
2. W. L. Baker, M. C. Clark, J. H. Degnan, G. F. Kiuttu, C. R. McClenahan, and R. H. Reinovsky, J. Appl. Phys. 49, 4624 (1978).
3. J. Davis, D. Duston, and P. Kepple, NRL Memorandum Report 3879, November, 1978 (unpublished).
4. J. Shiloh, A. Fisher, and N. Rostoker, Phys. Rev. Lett. 40, 515 (1978).
5. P. Burkhalter, J. Davis, J. Rauch, W. Clark, G. Dahlbacka, and R. Schneider, J. Appl. Phys. 50, 705 (1979).
6. P. Burkhalter and J. Davis, NRL Memorandum Report 3934, March, 1979 (unpublished).
7. P. G. Burkhalter, J. Shiloh, A. Fisher, and R. D. Cowan, J. Appl. Phys. 50, 4532 (1979).
8. C. Stallings, K. Childers, I. Roth, and R. Schneider, Appl. Phys. Lett. 35, 524 (1979).
9. J. D. Perez, L. F. Chase, R. E. McDonald, L. Tannenwald, and B. A. Watson, J. Appl. Phys. 52, 670 (1981).
10. M. Gersten, J. E. Rauch, W. Clark, R. D. Richardson, and G. M. Wilkinson, Appl. Phys. Lett. 39, 148 (1981).
11. R. F. Benjamin, J. S. Pearlman, E. Y. Chu, and J. C. Riordan, Appl. Phys. Lett. 39, 848 (1981).
12. J. S. Pearlman and J. C. Riordan, J. Vac. Sci. Technol. 19, 1190 (1981).
13. D. Duston, J. Davis, and P. C. Kepple, Phys. Rev. A 24, 1505 (1981).
14. D. Duston and J. Davis, J. Quant. Spectros. Radiat. Transfer 27, 267 (1982).
15. S. Maxon and T. Wainwright, preprint UCRL-88956, Lawrence Livermore National Laboratory, March, 1983 (unpublished).
16. R. E. Marrs, D. D. Dietrich, R. J. Fortner, M. A. Levine, D. F. Price, R. E. Stewart, and B. K. F. Young, Appl. Phys. Lett. 42, 946 (1983).
17. J. E. Bailey, Ph. D. dissertation, University of California, Irvine, 1983 (unpublished).

18. D. R. Bates, A. E. Kingston, and R. W. P. McWhirter, Proc. R. Soc. London, Ser. A 267, 297 (1960), and R. W. P. McWhirter, in Plasma Diagnostic Techniques, edited by R. H. Huddleston and S. L. Leonard (Academic, New York, 1965), pp 201-264.
19. D. Duston and J. Davis, Phys. Rev. A 21, 1664 (1980); Phys. Rev. A 23, 2602 (1981).
20. D. Duston, presented at Second International Conference/Workshop on Radiative Properties of Hot, Dense Matter, Sarasota, Florida, Oct. 1983 (to be published in J. Quant. Spectrosc. Radiat. Transfer).
21. J. Davis (to be published).
22. R. D. Cowan, Phys. Rev. 163, 54 (1967); J. Opt. Soc. Am. 58, 808 (1968).
23. A. K. Bhatia and U. Feldman, J. Appl. Phys. 53, 4711 (1982).
24. See J. Davis, P. C. Kepple, and M. Blaha, NRL Memorandum Report 2939, November, 1974 (unpublished).
25. R. E. H. Clark, D. H. Sampson, and S. J. Goett, Astrophys. J. Suppl. Series 49, 545 (1982).
26. A. K. Pradhan, D. W. Norcross, and D. G. Hummer, Phys. Rev. A 23, 619 (1981); Astrophys. J. 246, 1031 (1981).
27. M. Blaha and J. Davis, J. Quant. Spectrosc. Radiat. Transfer 19, 227 (1978); NRL Memorandum Report 3682, 1977 (unpublished).
28. K. Reed and A. Hazi, preprint UCRL-87014, Lawrence Livermore National Laboratory, December, 1981 (unpublished).
29. J. Davis, J. Quant. Spectrosc. Radiat. Transfer 14, 549 (1974).
30. P. C. Kepple (private communication).
31. J. Cooper, Rept. Prog. Phys. 29 35 (1966).

## B. Modeling of K-Shell Yields

### I. INTRODUCTION

It has long been a DNA goal to maximize the K-shell x-ray yield obtained in plasma discharges created with pulsed-power generators such as BLACKJACK 5 and PITHON. During FY85 important strides were taken in both comprehending previous results and in new concept development.

A key achievement in assessing the contributory factors to previously obtained K-shell yields and projecting the yields expected from future, higher-power machines, is described in the attached NRL Memorandum Report No. 5406, "K-Shell Yield Scaling Law for Conventional PRS Loads." This report is self-explanatory and requires no elaboration here.

We have also performed a detailed, quantitative assessment of the possibility of yield enhancement through use of optically thick mixtures of elements with similar atomic number, and find the concept to be very promising. In a similar study of optically thin mixtures, discussed elsewhere in this report, it was found that no yield increase was possible, but the spectral distribution could be tailored to the needs of the simulation by employing elements of widely divergent atomic number.

The present study is concerned with a considerably different mixture scenario: the plasma is optically thick and the atomic numbers very close. In this case, opacity effects do influence the total yield at the expense of spectral filling since the spectral lines from the various shells of the two elements lie fairly close in energy. As seen below, the effects produced by this type of mixture differ considerably from optically thin mixtures of significantly different atomic number.

We consider sodium and neon ions, mixed in varying ratio, and heated to temperatures at which the helium and hydrogen-like ionization stages are by far the dominant species. The choice of sodium and neon is of significant interest not only because of the close atomic numbers, but also because the Na X  $1s^2-1s2p^1P$  line at 11.0027 Å virtually coincides with Ne IX  $1s^2-1s4p^1P$  at 11.0003 Å. Therefore, the effect of direct overlap of high-opacity spectral regions may be ascertained.

The temperatures and densities attained in a pinch with a given current-voltage pulse are largely dependent on the plasma mass which is accelerated. Therefore, a reasonable comparison of the radiative emissivity of a mixture with that of a one-element plasma may be made by holding the mass density constant. Since sodium and neon have nearly the same mass, in the cases presented below we have kept the total ion density constant while varying the sodium/neon ratio, to remain reasonably faithful to the prescription for a meaningful comparison.

For a plasma of a given size, total ion density, temperature and sodium/neon ratio, we solve for the level populations and emitted radiation. The plasmas, which persist for tens of nanoseconds, are assumed to be in collisional-radiation equilibrium (CRE), that is, the level populations reach values which permit them to be in a steady-state consistent with the other level populations, atomic rates, and the ambient radiation field. To perform this calculation the critical elements required are the atomic level model and rates, and a radiation transport algorithm which accounts for two-element opacity overlap.

We consider only sodium-neon plasmas of such temperatures and densities that the K-shell dominates the ionic species. Hence, only ground states are carried in the model for all stages below lithium-like. For the lithium-like stages, the  $1s^2 2s^2 S$  (ground),  $1s^2 2p^2 P$ ,  $1s^2 3s^2 S$ ,  $1s^2 3p^2 P$ ,  $1s^2 3d^2 D$ ,  $1s^2 4l$  and  $1s^2 5l$  levels are included. The helium-like stage carries, in addition to the ground state, the  $1s 2s^3 S$ ,  $1s 2s^1 S$ ,  $1s 2p^3 P$ ,  $1s 2p^1 P$ ,  $1s 3l^3 L$ ,  $1s 3l^1 L$ ,  $1s 4l$ , and  $1s 5l$  levels. The hydrogen-like levels include  $n = 1$  through  $n = 5$ .

The atomic processes populating and depopulating the levels are: spontaneous radiative decay, electron collisional excitation and deexcitation, collisional ionization, 3-body, radiative, and dielectronic recombination. The continuum is optically thin in these plasmas; hence photoionization is neglected. Line photoexcitation is calculated by a self-consistent radiative transfer model.

#### a. K-Shell Output of Optically Thick Mixtures

Calculations have been performed for a variety of assumed plasma conditions to determine the total K-shell resonance line power as a function of the sodium/neon ratio. In each case a cylindrical plasma of length 4 cm of fixed total (sodium plus neon) ion density is assumed. The temperature, diameter, and sodium/neon ratio were varied, and the results are summarized in Fig. 1 and Table I. In Fig. 1 the K-shell power output in J/nsec is plotted as a function of the fractional abundance of sodium ions for a variety of plasma conditions. Note that generally the power output (equivalent to K-shell emissivity) peaks at a sodium ion concentration of 50-75%, and that the emissivity in some cases substantially exceeds that obtained either for pure neon or for pure sodium. The effect is more pronounced as the line opacity of the plasma (roughly proportional to the product of ion density and diameter) increases. Therefore, the K-shell emissivity of an opaque plasma mixture may exceed that for either element alone for similar atomic number elements. The precise nature of this effect is illuminated in Table I, where the power outputs for sodium and neon Ly  $\alpha$  and He  $\alpha$  ( $1s^2-1s2p^1P$ ) lines are given for various plasma conditions. These two lines usually account for more than 65% of the K-shell power. Were the composition of an optically thin plasma to be changed from pure neon to 50% neon, for instance, the line power output would decrease by 50% - ignoring small changes in the electron density due to sodium. However, inspection of the table reveals that the neon lines' output never drops by as much as 50% and in fact usually drops by only about 20%. The one exception is the least opaque plasma of ion density  $10^{19} \text{ cm}^{-3}$ , where the Ne IX He  $\alpha$  power drops by nearly 40%. In this least opaque plasma the Ly  $\alpha$  optical depth is  $\sim 50$ . The same effect exists for sodium. The change of the photon output is due to opacity effects. This results in the greatest emissivity occurring for an intermediate mixing ratio of sodium-to-neon, where there are twice as many lines radiating as in the pure element case and the optical depths of the radiating lines are smaller than for the pure-element case.

## b. Radiation Physics Controlling Power Output

In analyzing the transfer of line photons in laboratory plasmas, the following conceptual picture is often useful. A line photon is "created" when the upper level of the transition is collisionally populated and then decays radiatively. Following its creation in an optically thick plasma the photon will generally be reabsorbed and reemitted a considerable number of times before being quenched or ultimately escaping the plasma. During each reabsorption there is a finite probability  $P_Q$  that the level will be collisionally depopulated and the line photon destroyed. This probability  $P_Q$  is given by  $D/(D+A)$  where  $D(\text{sec}^{-1})$  is the sum of the collisional rates out of the upper transition level times the electron density and  $A$  is the spontaneous decay rate for the line. Following its initial collisional creation the photon will ultimately suffer one of two fates: destruction or eventual escape from the plasma. We denote the probability of eventual escape by  $P_e$ ; the probability of escape on any single flight is given by  $P_e$ . The quantity  $P_e$  may be obtained by considering the condition for a steady-state population  $N$  of the upper level. Letting  $C$  stand for the collisional creation rate this condition is

$$C = N (D + AP_e) \text{ (cm}^3/\text{sec)} \quad (1)$$

where in Eq. (1), radiative reabsorption of the line photon is taken into account by diluting the decay rate by the single-flight photon escape probability. Even in a uniform plasma,  $P_e$  varies with position - Eq. (1) is intended as spatially averaged approximate description of the photon transfer. After a few simple manipulations, Eq. (1) yields, taking into account that  $P_Q = D/(D+A)$ ,

$$\frac{NAP_e}{C} = \frac{P_e(1-P_Q)}{P_Q + (1-P_Q)P_e} \quad (2)$$

However, the left-hand-side of Eq. (2) is the total photon emission rate divided by the total upper level excitation rate; that is, precisely the ultimate escape probability. Therefore,

$$P_u = \frac{P_e(1-P_Q)}{P_Q + (1-P_Q)P_e} \quad (3)$$

in this approximation.

In Figs. (2) and (3) we have plotted the quantities  $P_e$ ,  $P_Q$ , and  $P_e(1-P_Q)/[P_Q+(1-P_Q)P_e]$  vs. sodium ion density and diameter, respectively. These parameters are displayed for the Na X  $1s^2-1s2p^1P$  line for a temperature of 400 eV and, for Fig. 2, a fixed diameter of 1.4 mm. Fig. 3 reflects calculations for a fixed sodium ion density of  $10^{20} \text{ cm}^{-3}$ .  $P_e$  and  $P_Q$  are obtained from Voigt profile formulae and the atomic rates, respectively. The accuracy of the spatial-average approximation is indicated in both Figs. 2 and 3 by also plotting  $P_u$  as numerically calculated from the actual computed line photon output power. As is obvious, excellent correspondence is obtained with the probabilistic, spatial-average approximation of Eq. (3). This is especially significant in light of the fact that even though the plasma temperature and density are assumed spatially uniform, the presence of a boundary guarantees a significant degree of nonuniformity in both the photon field and the spatial profile of the level populations.

The important feature of Fig. 3 relevant to the mixture emissivity is the behavior of  $P_u$  with respect to opacity. Optical depth varies approximately linearly with plasma diameter. The electron density in a sodium-neon plasma is very nearly constant with sodium/neon mixing ratio provided the total ion density is constant. Therefore, halving the diameter of a pure sodium plasma would lead to an increase in  $P_u$  very similar to that which is obtained by comparing a pure sodium plasma to one of the same ion density which is half sodium, half neon. The profile of Fig. 3 indicates that  $P_e \sim \tau^{-1/2}$  for optically thick K-shell sodium plasmas of ion density  $10^{20} \text{ cm}^{-3}$  in the 1-10 mm range. Therefore, halving the optical depth by reducing the sodium fraction from 1.0 to 0.5 results in  $P_u$  increasing by 40%. The other sodium and neon lines experience a similar - through not identical - increase in  $P_u$ , which accounts for the curves of Fig. 1.

c. Implications for DNA Objectives

The above results show convincingly that the K-shell emissivity of a plasma may be increased by employing mixtures of elements of similar atomic number - where the total mass employed in a machine such as BLACKJACK 5 would remain the same as that used on a conventional single-element shot. The mechanism that increases the emissivity is that the optical depths of each element are less, allowing more photons out - and twice as many lines are present in the K-shell region. The choice of sodium and neon does not mean that these promising results would be confined to these elements. Indeed, the physics would be very similar for mixtures such as aluminum-silicon, magnesium-aluminum, argon-titanium, or calcium-titanium. We recommend that a series of experiments using one or more of the above mixtures be carried out to test these concepts. Conceivably, the use of three or more elements could, by further enhancing the photon escape and multiplying the number of K-shell lines, result in even greater increases in power output than calculated here for the sodium/neon mixture.



TABLE I: Power (Outputs (J/nsec) for Ly  $\alpha$  and He  $\alpha$

$$d = 5.6 \text{ mm}, T_e = 400\text{eV}, N_I = 5 \times 10^{19} \text{ cm}^{-3}$$

	<u>Pure Na</u>	<u>75Na, 25Ne</u>	<u>50Na, 50Ne</u>	<u>75Ne, 25Na</u>	<u>Pure Ne</u>
Ne IX He $\alpha$	---	58.	74.	85.	94.
Ne X Ly $\alpha$	---	286.	364.	420.	467.
Na X He $\alpha$	303.	251.	197.	133.	---
Na XI Ly $\alpha$	867.	759.	638.	467.	---

$$d = 2.8 \text{ mm}, T_e = 400\text{eV}, N_I = 10^{20} \text{ cm}^{-3}$$

	<u>Pure Na</u>	<u>75Na, 25Ne</u>	<u>50Na, 50Ne</u>	<u>75Ne, 25Na</u>	<u>Pure Ne</u>
Ne IX He $\alpha$	---	36.	44.	50.	54.
Ne X Ly $\alpha$	---	171.	214.	245.	270.
Na X He $\alpha$	167.	141.	112.	79.	---
Na XI Ly $\alpha$	480.	423.	357.	268.	---

$$d = 1.4 \text{ mm}, T_e = 400\text{eV}, N_I = 10^{20} \text{ cm}^{-3}$$

	<u>Pure Na</u>	<u>75Na, 25Ne</u>	<u>50Na, 50Ne</u>	<u>75Ne, 25Na</u>	<u>Pure Ne</u>
Ne IX He $\alpha$	---	14.	18.	20.	22.
Ne X Ly $\alpha$	---	68.	85.	97.	106.
Na X He $\alpha$	63.	53.	43.	31.	---
Na XI Ly $\alpha$	183.	159.	134.	100.	---

$$d = 2.8 \text{ mm}, T_e = 400\text{eV}, N_I = 10^{19} \text{ cm}^{-3}$$

	<u>Pure Na</u>	<u>75Na, 25Ne</u>	<u>50Na, 50Ne</u>	<u>75Ne, 25Na</u>	<u>Pure Ne</u>
Ne IX He $\alpha$	---	6.	10.	13.	16.
Ne X Ly $\alpha$	---	29.	45.	57.	66.
Na X He $\alpha$	51.	39.	28.	15.	---
Na XI Ly $\alpha$	87.	67.	46.	23.	---

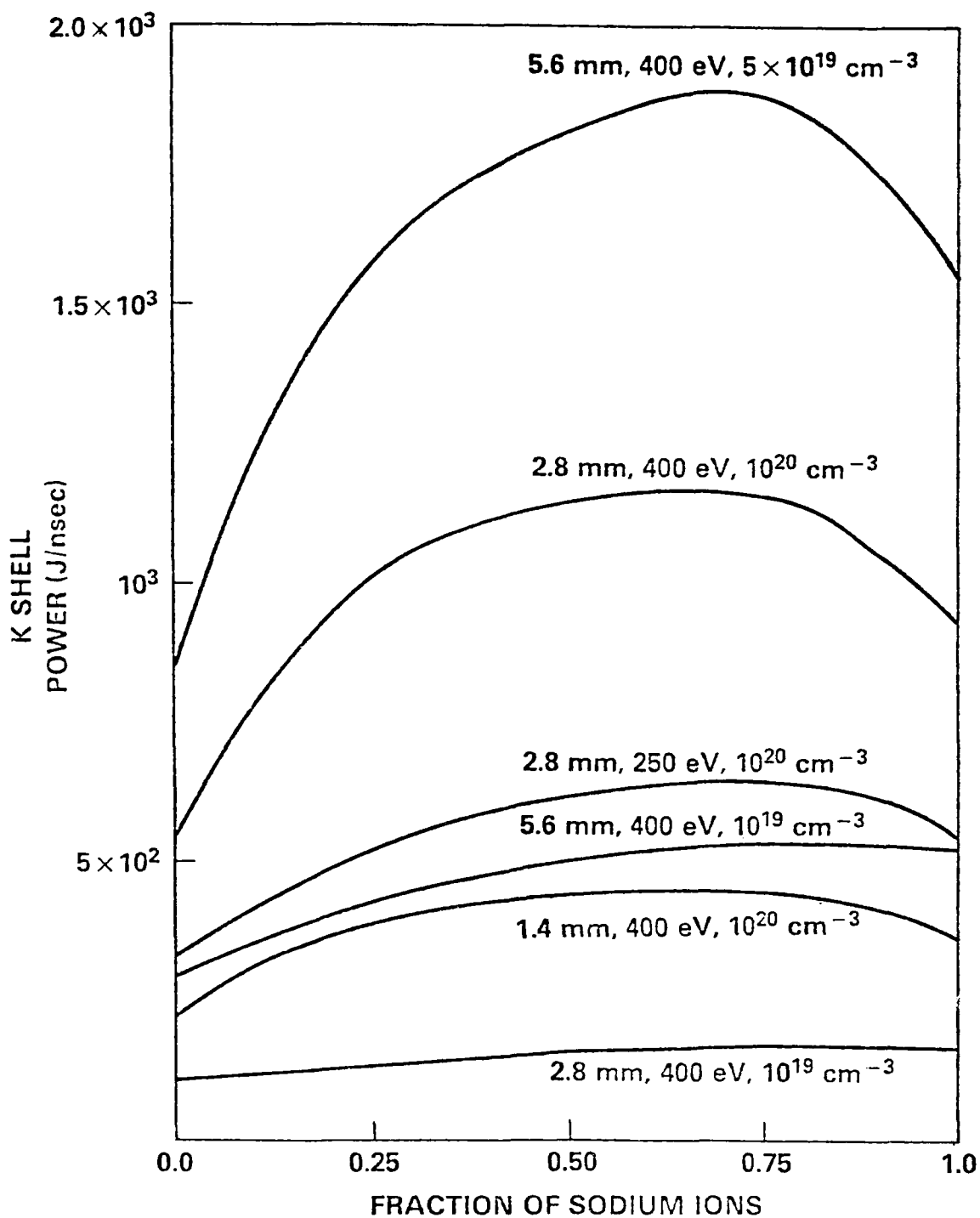


Fig. 1. The total K-shell power output in J/nsec from a sodium-neon plasma is plotted against fractional abundance of sodium for a range of indicated plasma conditions. In each case the plasma is assumed to be a 4 cm-long cylinder with fixed total ion density (sodium plus neon ions).

A typical problem mesh consists of 32 zones in the R direction and 14 zones along Z. This relatively coarse grid is dictated at present by both memory and run time considerations of the atomic physics model. After initialization, the 2-D PRISM code was run with the atomic physics package turned on. Although, at present, there is no radiation transport in the 2-D runs. As a comparison, several runs were also made without the atomic physics model.

Figure 3 shows density contours out to the 95% mass line (i.e., 95% of the mass lies inside of the last contour) at 1.12  $\mu\text{sec}$ . The 2-D run was initialized at 1.05  $\mu\text{sec}$ . In this figure and in the figures which follow, the wavelength,  $\lambda$ , is 1 cm. The contours are separated logarithmically by 0.25 or by one quarter of a decade. As discussed above, the shell is roughly 1 cm in thickness and can be defined by one full decade (i.e., four contour lines) centered near 3.5 cm. The backside has begun to show signs of an instability at 1.13  $\mu\text{sec}$  as evidenced by the contours near  $R = 8$  cm ( $Z=0$ ) in Fig. 4. By 1.24  $\mu\text{sec}$ , the disturbance has penetrated to the fourth contour as shown in Fig. 5. Figure 6 shows density contours computed from the mesh at the same time but the contours only go out to the 80% mass line. The same quarter decade contour separation in the density contours has been used so that comparisons can be made. It can be seen that at this time the region near the 80% mass line has only been slightly perturbed. In Fig. 7, the contours are shown just prior to assembly on axis. Contours are again shown out to the 95% mass line and indicate that the perturbation has grown significantly at the rear of the shell. However, the interior portion of the shell, which at this time lies within 1 cm, still remains unperturbed and intact. Figure 8 shows the contours out to the 80% mass line at this time. At this time, the disturbance has penetrated only slightly more into the shell than at 1.24  $\mu\text{sec}$ . We would expect this from looking at the 1-D plots in Fig. 2 where it is seen that even near the time of implosion, the regions where  $rB_\theta$  and  $\rho$  cross is very narrow. This is characteristic of a "snowplow" implosion where all the mass of the shell and the background gas interior to the shell is swept up by the field. Since this effect creates only a narrow region with large gradients near the backside of the shell, this has been referred to as "snowplow stabilization". In comparison, Fig. 9 shows the shell out to the

## b. Two-Dimensional Implosion Modeling

An important issue for high velocity Z-pinch PRS loads is the stability of the plasma shell as it is accelerated under the action of the axial magnetic field. In the case of an accelerating shell, the backside is unstable in the region where the density gradient is of opposite sign to the acceleration. The issues are then twofold: (1) how much of the shell mass is in this unstable configuration; and (2) what is the magnitude of the growth rate of the instability and how does this compare to the implosion time. A summary of our results obtained from modeling a representative load is given below. A more detailed description will follow under separate cover.

The load we have chosen to model is a 120  $\mu\text{g}/\text{cm}$  argon gas shell initially at 20 cm and with a width of roughly 3 cm. Ten percent of the mass lies within 15 cm and represents the background gas. The current pulse rises to 3.6 MA at 1  $\mu\text{sec}$  and then drops to a small value by 1.3  $\mu\text{sec}$ .

We modeled this problem in two steps. First, a 1-D PRISM run was made with all the relevant physics, including radiation transport, turned on. Second, the output from this run was then used to initialize several 2-D runs. Figure 1 shows a plot of several mass radii versus time. The mass percentile values indicate how much mass lies inside that mesh line. From this plot, we can see that the shell does not become fully compressed and accelerated until about 0.9  $\mu\text{sec}$ . This is slightly before peak current. Figure 2 shows density and  $rB_\theta$  profiles for three separate times. At 1.05  $\mu\text{sec}$  the width of half-maximum of the shell is approximately 1 cm. A density "foot" is seen to extend another 1 cm in front of the shell. The backside region where the gradients are in opposite directions lies within a region less than 1 cm.

The 2-D runs were initialized by expanding the 1-D profiles at a selected time in the Z-direction and then adding a perturbation which is centered around the density peak of the imploding shell. Symmetry allows the Z domain to extend from 0 to  $\lambda/2$  where  $\lambda$  is the perturbation wavelength. The quantity  $A/\lambda$ , where A is the amplitude of the perturbation, was fixed at 0.1 for all wavelengths considered.

## Gamble II Implosion Time

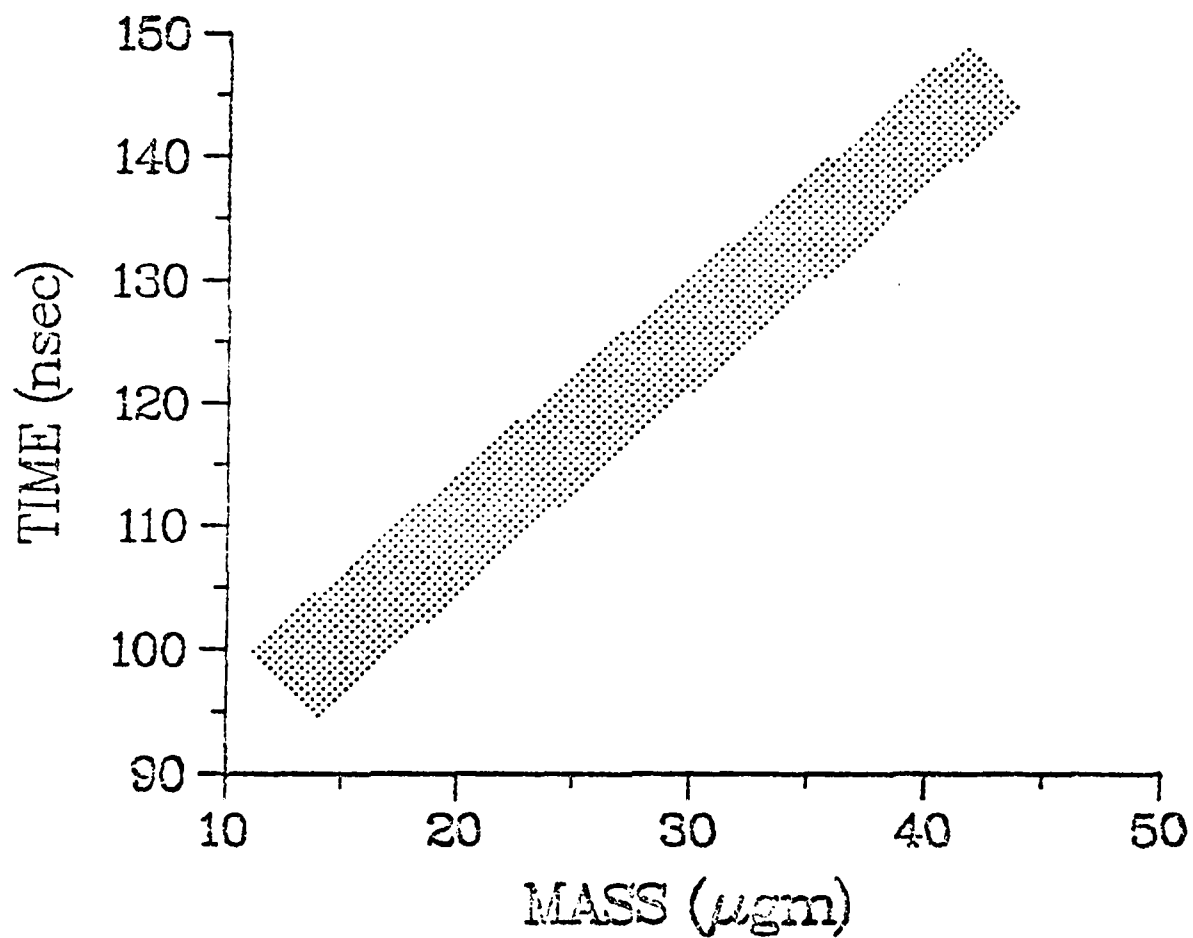


Fig. 5 — GAMBLE II implosion time as a function of mass .

## Gamble II K-Line Yield

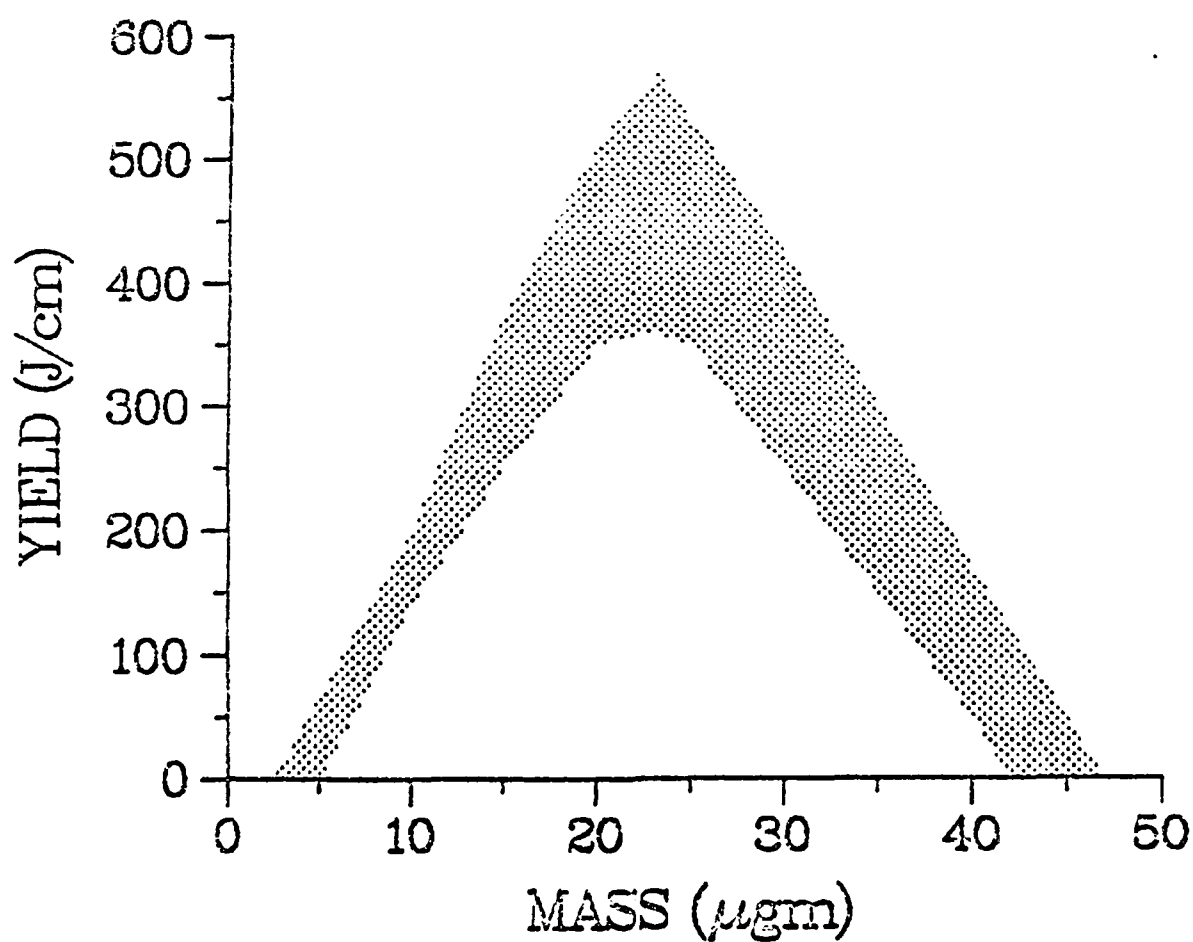


Fig. 4 — K-line yield as a function of mass for GAMBLE II .

20  $\mu\text{gm}$

# R vs TIME

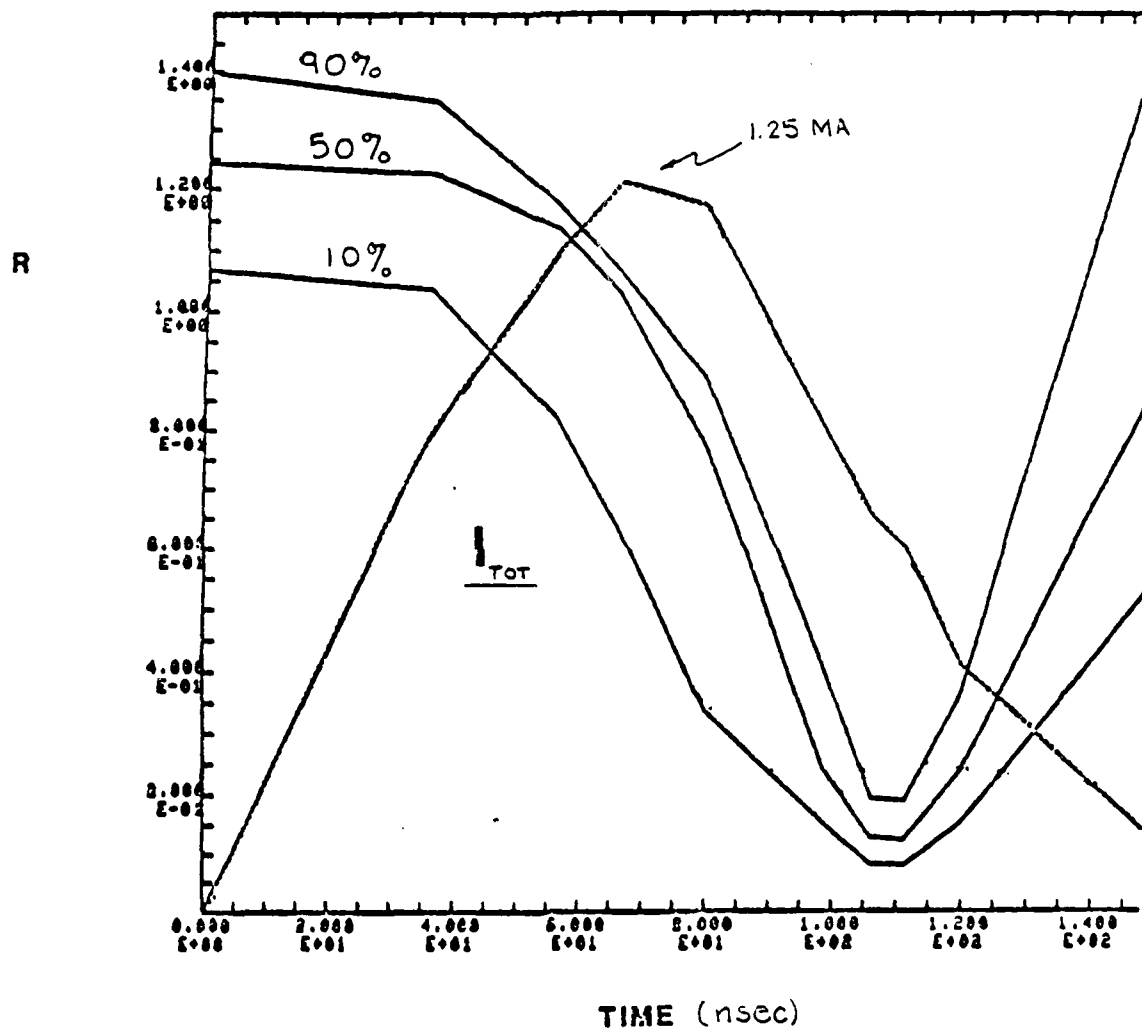


Fig. 3 — Time history of several mass lines for a 20  $\mu\text{gm/cm}$  GAMBLE II implosion.  
Also shown is the time history of the total current,  $I$ .

$\rho$        $rB_\theta$   
 $10^{-4} \text{ gm/cm}^3$     $10^5 \text{ (G-cm)}$

20  $\mu\text{GM}$

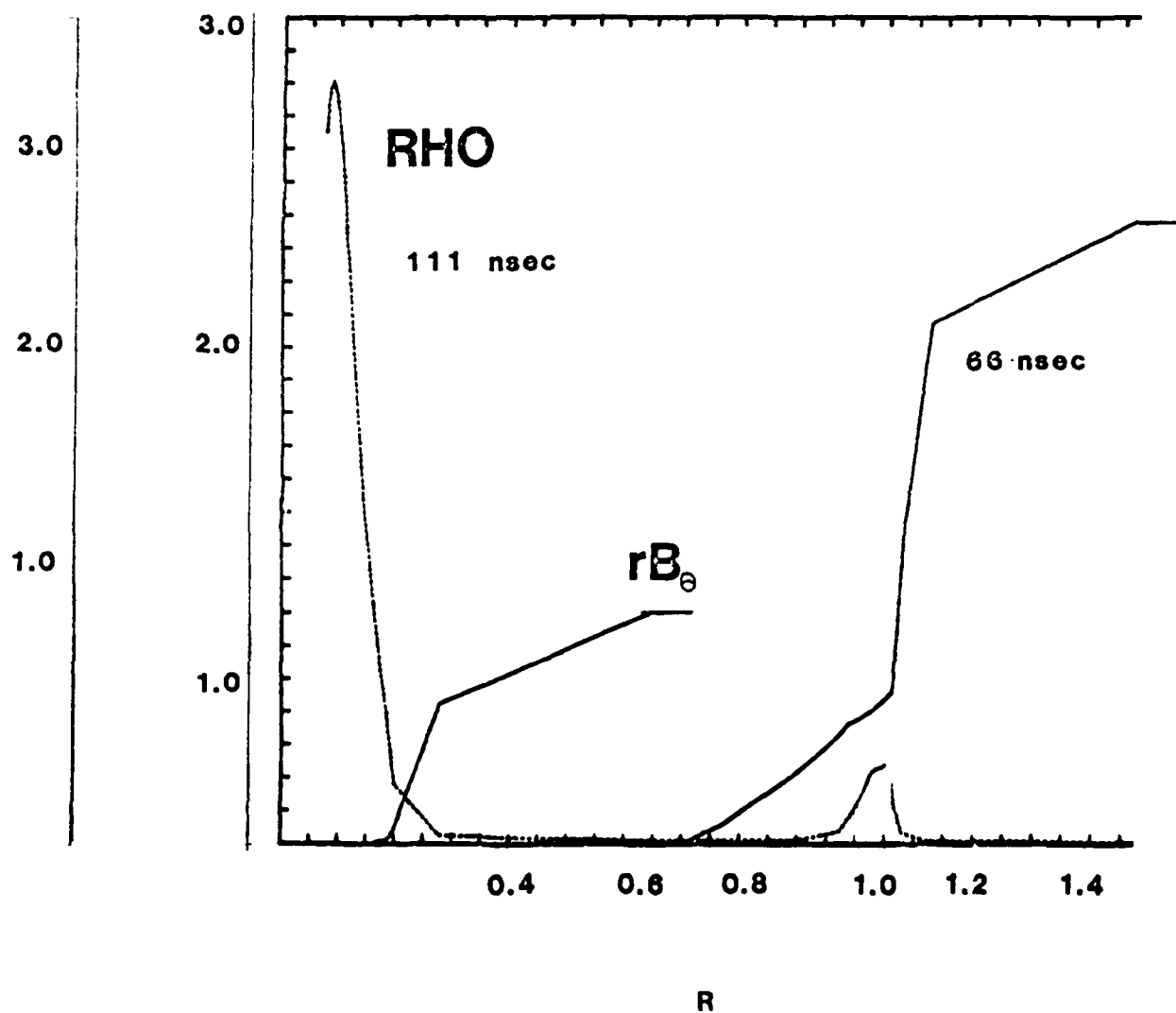


Fig. 2 — Density and magnetic field profiles at two separate times for a 20  $\mu\text{gm/cm}$  GAMBLE implosion.



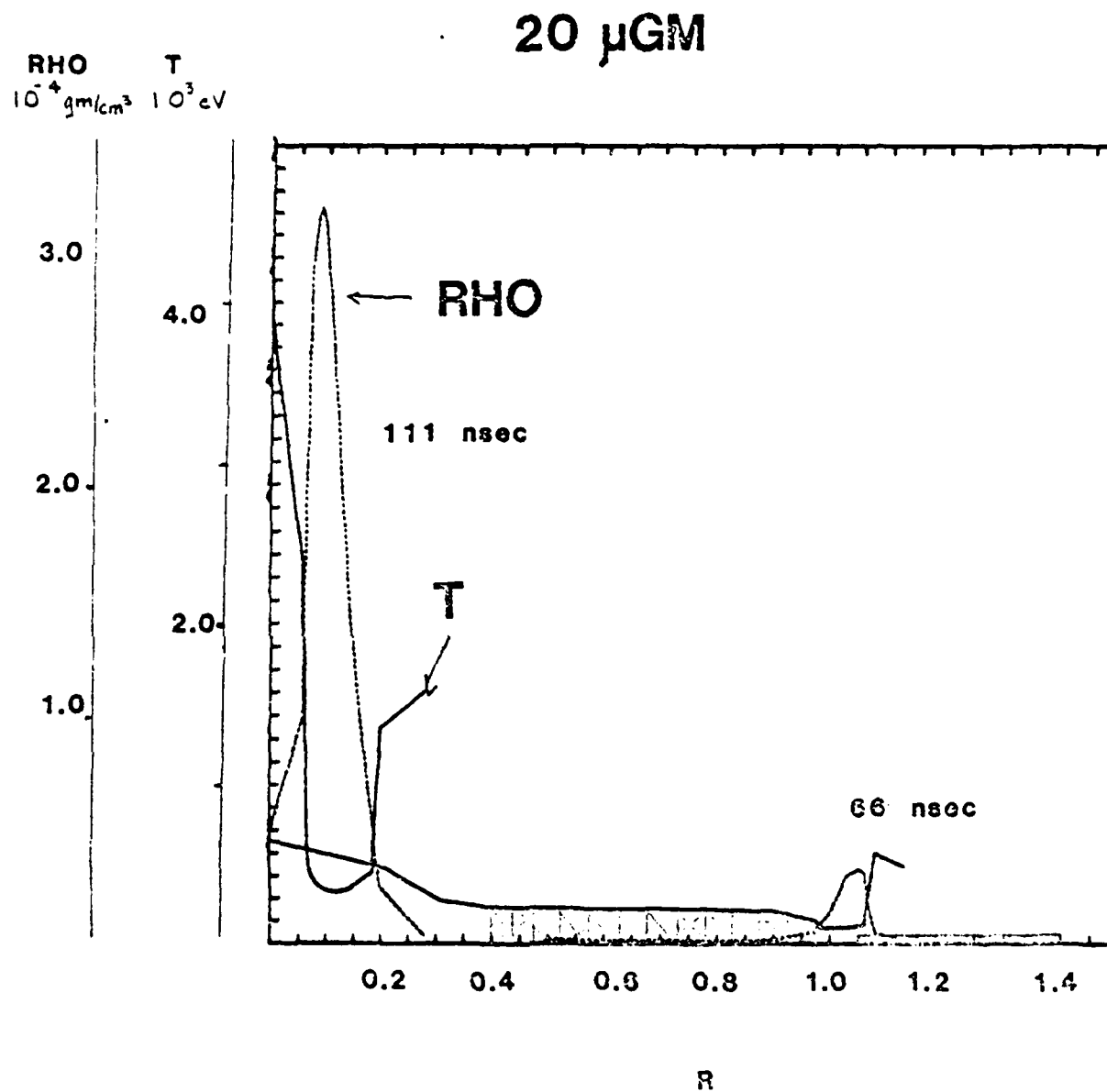


Fig. 1 — Density and temperature profiles at two separate times for a 20  $\mu$ gm/cm GAMBLE II implosion. The cross-matching indicates the region where radiation is being absorbed.

2 kJ over the 4 cm length. Overall, the yield values displayed in this figure overlap those given by the experiment. The qualitative picture is of a peaking of the yield with mass, followed by a rollover of the yield curve. At low mass, the yield is a function of the amount of material which is available to radiate. At higher masses (i.e. greater than 30  $\mu\text{g}/\text{cm}$ ) it becomes increasingly more difficult to accelerate the shell so that the mass is driven to lower peak temperatures during the implosion process.

The dispersion near the peak yield is due to the fact that at an optimum temperature, the yield is sensitive to both the density at that temperature as well as the amount of mass. Since the power goes as the density squared, the integration over an effective volume and time interval gives a yield which is proportional to the average density. Thus, changes in the average density of roughly 20% can account for the difference between the mean yield and the maximum yield if the temperature is assured to be constant during the implosion. It should be remembered that the density changes by roughly two orders of magnitude during the implosion. Also, we have ignored important variations due to temperature, opacity, and other dynamical effects in the above discussion. Therefore, the best that one can hope for out of a study such as this is a qualitative picture which quantifies values within a sensitivity range as shown in Fig. 4.

Figure 5 shows the implosion time as a function of mass. Again, a large number of runs were used in making this plot and a spread of approximately 10 nsec is seen for a given mass value. The implosion times for masses in the 20  $\mu\text{g}$  to 35  $\mu\text{g}$  range are consistent with the values obtained in the experiment.

The time history of the implosion for several mass radii is shown in Fig. 3. The current waveform is also shown. A snowplow is seen to develop between 40 nsec and 60 nsec. It is important to note that the plasma is still at 90% of its initial radius at the time of peak current. The implosion itself occurs at 110 nsec when the total current is substantially reduced. Disassembly occurs rapidly after this time. The shell is within 30% of its initial radius for 30 nsec and this roughly defines the time span of the radiation pulse.

Figure 4 shows the power output as a function of time. Four curves are shown and represent total yield and K-line yield for the 20  $\mu\text{gm/cm}$  case with the radiation transport turned on and with the radiation transport turned off. There are several salient features in this figure. First, one notes that in the case without transport, there is significant power output between 40 nsec and 90 nsec. This feature disappears when the radiation transport is turned on. Most of this radiation comes from the L-shell but is severely inhibited by opacity effects in the case with transport. This is evidenced by the previously discussed cross-hatched region that appears in Fig. 1.

Another feature is the difference in the implosion time and peak power output between the two cases. Again, these effects can be explained by the fact that the opacity tends to keep the temperature higher. This tends to slow down the implosion because of an increased "back" pressure pushing against the inward moving gas shell. The larger K-shell output occurs because the fraction of the shell which contributes to the radiative yield during the implosion phase reaches a higher temperature with opacity effects included.

Figures 4 and 5 show the composite results of roughly 25 computer runs. Variations were made in mass (increasing along the horizontal axis in both figures) as well as turning the radiation transport on and off, adjusting a multiplier on the magnetic field diffusion coefficient, and varying the initial temperature of the plasma.

The K-line yield displayed in Fig. 4 shows a peak near 22  $\mu\text{gm/cm}$  with a mean value of 450 J/cm. Over a 4 cm experimental length, this corresponds to a total yield of 1.8 kJ. By varying the parameters in the proper fashion, it can be seen that it is possible to obtain greater than

## C. Dynamics of Imploding Z-Pinch

### I. GAMBLE II MODELING

During the past year, we have modeled the Gamble II experiment with a one-dimensional version of our radiation hydrodynamics simulation code, PRISM. This version of the code employs: (1) radiation transport where opacity effects are important, (2) equation of state utilizing non-LTE atomic physics and (3) an input current wave form coupled with a diffusive equation for the magnetic field,  $B_\theta$ . We have also used the two-dimensional version of PRISM to model the later phase of the implosion near axis. At present, this version of the code does not transport radiation and is therefore only valid in the thin limit.

#### a. 1-D Modeling

The NRL Gamble II neon gas puff experiment has a current risetime of approximately 65 nsec with a peak current of 1.25 MA. The initial central radius of the gas shell formed by the supersonic nozzle is assumed to be 1.25 cm with a 3 mm width. Thus, a mass of 20  $\mu\text{gm/cm}$  corresponds to an initial density of 7.31  $\mu\text{gm/cm}^3$  in the shell. Here we have assumed that the density inside the shell is ten percent that of the shell.

Figure 1 shows the evolution of a Z-pinch implosion utilizing Gamble II parameters. Density and temperature profiles are displayed. Two times are shown corresponding to a time near peak current and a time near implosion. The cross-hatching under the temperature profile indicates that this region is a net absorber of radiation. The effect of this feature is to help maintain the temperature of the core. Figure 2 shows the same density profiles with the magnetic field (actually  $rB_\theta$ ). The sharp gradient in  $rB_\theta$  is due to the fact that the hot core increases the conductivity (i.e.  $\sigma \sim T^{3/2}$ ) and prevents diffusion of the field. It can also be seen that the total current,  $I = \frac{c}{2}(rB_\theta)$ , has decreased dramatically at the later time as dictated by the current waveform.

Clearly, a very good fit is obtained for an ion density of  $4 \times 10^{19} \text{ cm}^{-3}$  and assumed neon plasma temperature of 165 eV. The other three calculated outputs clearly demonstrate the sensitivity of these conditions, relative to the line power outputs produced.

A pinched ion density of  $4 \times 10^{19} \text{ cm}^{-3}$  with a diameter of 1.8 mm implies a total K-Shell radiating mass is 34 micrograms ( $\mu\text{g}$ ) per centimeter. The nozzle puff calculations carried out by NRL's Plasma Technology Branch suggest total puffed masses of 35-50  $\mu\text{g}/\text{cm}$  for this shot. Therefore, this preliminary analysis suggests that Gamble-II is very efficient at incorporating most of the puffed mass into a K-shell-radiating pinch. This is consistent with the very low L-shell yields that have been observed on this shot series. It also contrasts with the previous BLACKJACK 5 and PITHON series where, typically, 10-25% of the cold loaded mass ultimately radiated K-shell photons. This very interesting and promising preliminary result must be further validated by more shot analyses before it can be accepted as fact.

## II. GAMBLE-II NEON SPECTRUM ANALYSIS

At this writing, one Gamble-II neon gas puff shot (#2533) spectrum has been reduced to absolute intensities for the principal K-shell radiating lines. We have analyzed this spectrum using the collisional-radiative model described above.

In shot 2533, a total neon K-shell yield of 2.1 kJ was produced. Of this 2.1 kJ, 680 J appeared in the Ne IX  $1s^2-1s2p^1P$  ("He  $\alpha$ ") line, and 1040 J appeared in the Ne X  $1s-2p$  line ("Ly  $\alpha$ "). Since these lines obviously dominate the yield, we have concentrated our analysis on reproducing this power output.

In each case, the pinch is assumed to have a length of 4 cm. A series of four spectra were calculated, for various assumed temperatures and densities. The diameter was set equal to 1.8 mm, in accordance with the pinhole imaging, for all five of these spectral calculations which attempted to fit the measured power output. The results are summarized in Table II below.

Table II: Gamble-II Shot 2533, Calculations and Measurements

$N_I$	$T_e$	<u>He <math>\alpha</math> power (J/nsec)</u>	<u>Ly <math>\alpha</math> power (J/nsec)</u>
--	--		
$4 \times 10^{19} \text{ cm}^{-3}$	175 eV	20	22
$6 \times 10^{19}$	160	20	37
$6 \times 10^{19}$	170	26	33
$4 \times 10^{19}$	165	16	25
Shot 2533 Measured -----		17	26

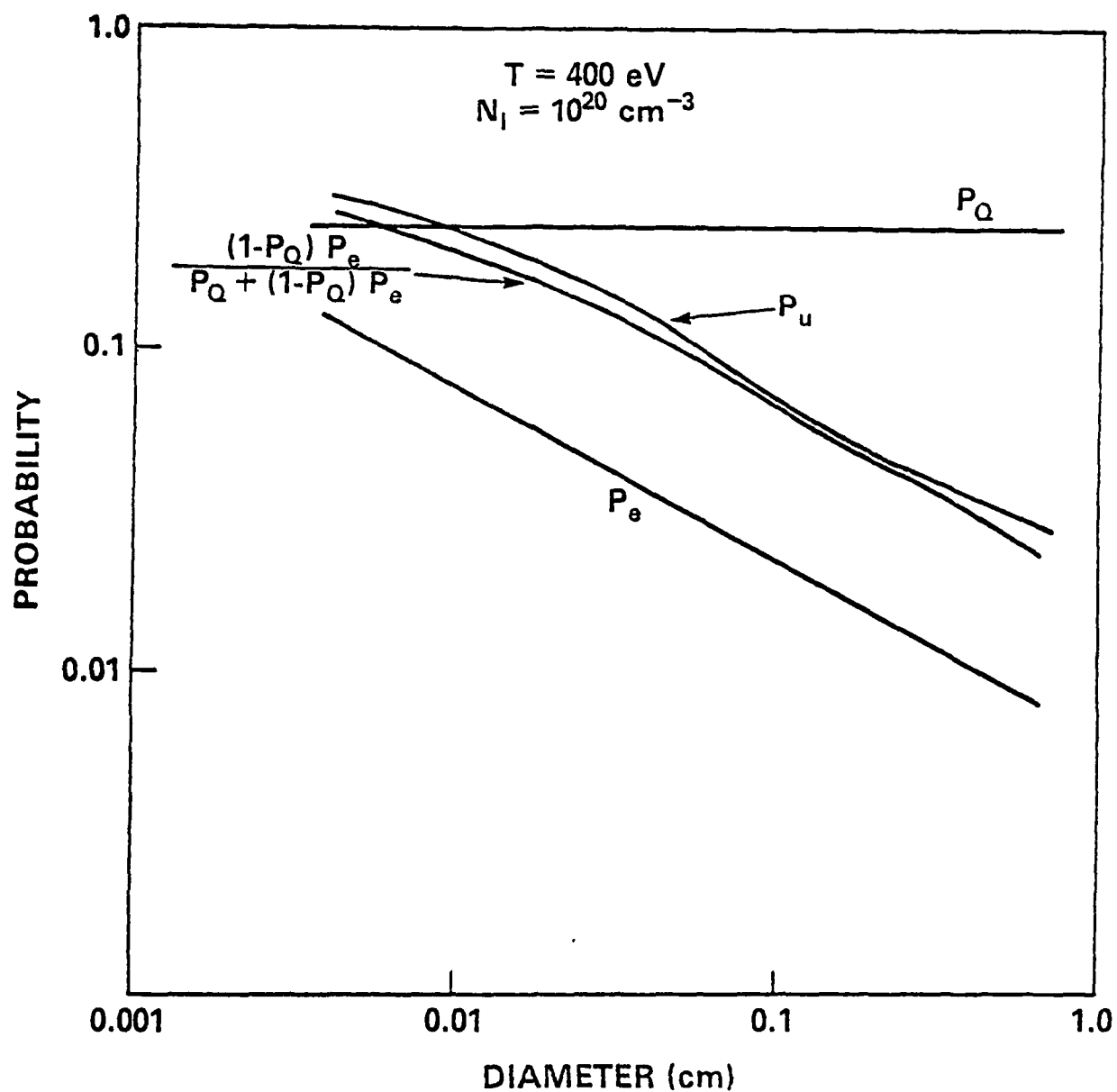


Fig. 3. Same as Fig. 2, except the quantities are plotted against cylindrical plasma diameter for a sodium ion density of  $10^{20} \text{ cm}^{-3}$  at a temperature of 400 eV.

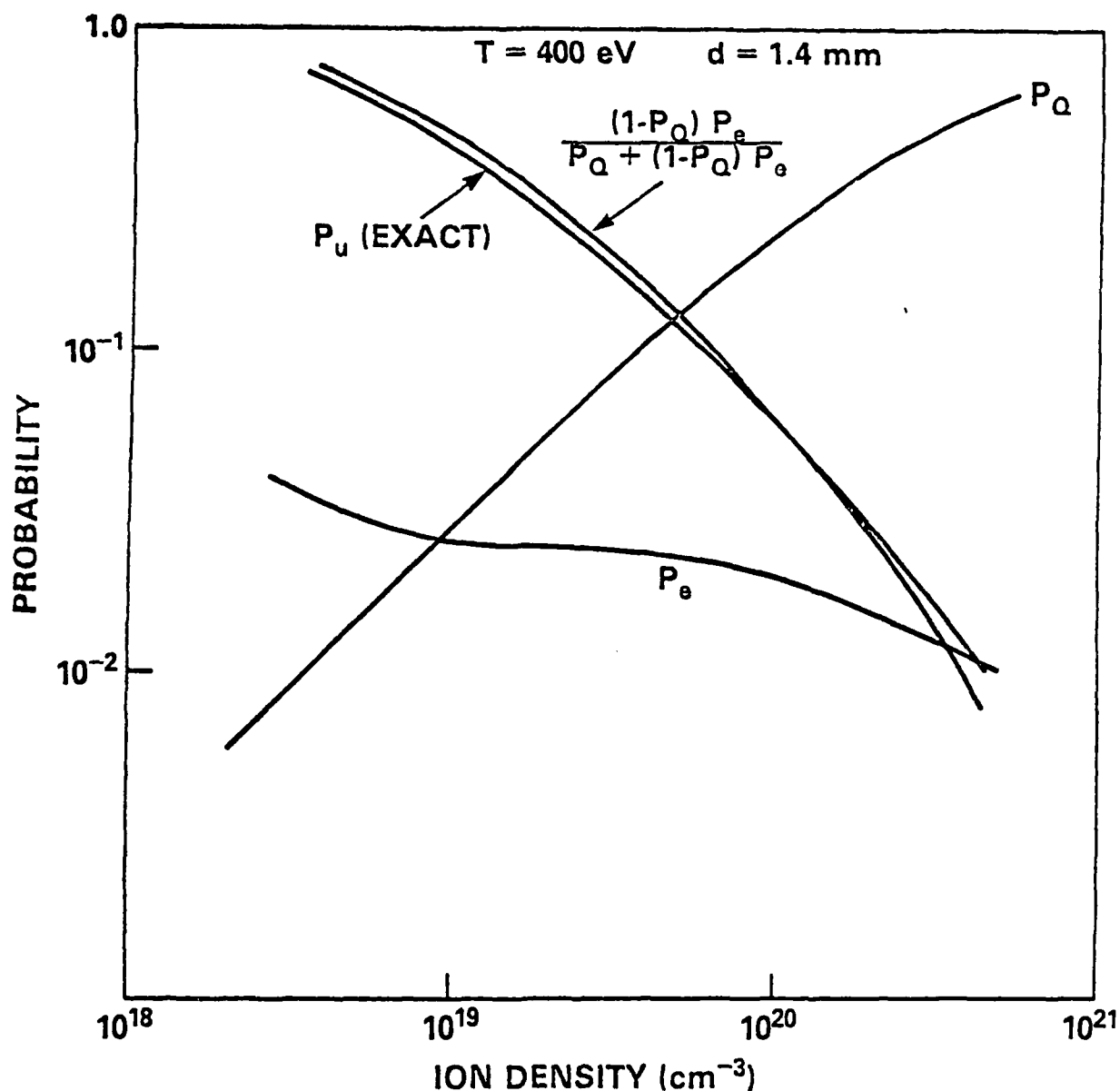


Fig. 2. The spatially averaged single-flight escape probability  $P_e$ , the collisional photon quenching probability per scattering  $P_Q$ , and the approximate analytic ultimate escape probability are plotted against ion density for a 400 eV cylindrical sodium plasma of diameter 1.4 mm. Also shown is the exact computed numerical ultimate escape probability  $P_u$ .



50% mass line where little or no disturbance is seen. Thus, a large fraction of the shell (e.g., greater than or equal to 50%) is seen to remain intact.

The growth of the backside of the shell is illustrated in Fig. 10. The growth rate can be calculated by measuring the difference between the 90% mass lines at  $Z = 0$  cm and at  $Z = 0.5$  cm. Both of these points are modes which are constrained to move only in the  $R$  direction. The approximately linear growth of the amplitude is apparent in this figure. At the 95% mass line, the growth of this difference is nearly identical to that of the 90% mass line. However, at the 80% mass line the growth is reduced as shown in Fig. 11. This is also apparent in Figs. 6 and 8. The growth at the 50% mass line is so small that it cannot be accurately measured from a plot such as this.

The growth rate results are summarized in Fig. 12 for several wavelengths. As discussed above, the growth rates are calculated by comparing the radial position of the 90% mass line at  $Z = 0$  and  $Z = \lambda/2$ . A second set of data is shown in which the procedure for running the 2-D calculations outlined above was duplicated except that the atomic physics packages were turned off in both the 1-D initializing run and in the 2-D perturbation runs. These runs were made for comparison purposes. The error bar denotes a typical variance in measuring the growth rate using data from different time sequences.

The results show that the growth rate peaks near 1 cm. This is approximately the thickness of the imploding shell. At long wavelength, the growth rate drops off nearly as the square root of  $\lambda^{-1}$ . This is the dependence of the classical Rayleigh-Taylor growth rate for a sharp boundary between two fluid layers of semi-infinite extent. At longer wavelengths, the shell thickness and, consequently, the gradient scale lengths are small compared to the wavelength so that this correspondence is reasonable. The decreasing growth rate at short wavelengths is also a phenomena which has been seen before in calculations of Rayleigh-Taylor instabilities in shells.<sup>1</sup> This can be attributed to the fact that the instability samples only a small portion of the shell as contrasted to the classical case of a sharp interface where the instability "feels" the entire density gradient.

The two sets of data points shown in Fig. 12 exhibit the same qualitative behavior except that the peak growth rate is lower and occurs at a slightly longer wavelength when the atomic physics is turned off. Both of these effects can be attributed to the fact that without the atomic physics the thermal energy of the shell and background gas are higher. Consequently, the pressure is also higher. This limits the compression of the shell as well as the acceleration of the shell. The thicker shell accounts for the shift in the peak growth rate and the lower acceleration accounts for lowered growth rates since  $\gamma_{cl} \sim \sqrt{ka}$  where  $\gamma_{cl}$  is the classical growth rate,  $k$  is the wavenumber, and  $a$  is the acceleration. A peak growth rate of  $1.5 \times 10^7 \text{ sec}^{-1}$  implies a growth period or e-folding time of 67 nsec. Thus, over the approximately 300 nsec where one would expect the instability to be active (i.e., the time frame over which the shell is accelerated inward), there would be 4.5 growth periods. This corresponds to an amplitude increase of 90. An initial amplitude of 0.01 cm would then grow to 0.9 cm. This growth is dramatically reduced at shorter wavelengths (i.e., high- $k$ ) modes. Also, the shell is unstable over only a small region. Most of the shell is stabilized due to the snowplow effects of the magnetic field. The largest fraction of the K-shell radiation can be expected to come from the dense inner part of the shell which is raised to the highest temperatures during the implosion. Therefore, these results lead one to expect that there is minimum degradation in the K-line output from this effect since it appears that at least 50% or more of the shell remains intact.

#### References

1. C. P. Verdon, R. L. McCrory, R. L. Morse, G. R. Baker, D. I. Meiron, and S. A. Orszag, Phys. Fluids 25, 1653 (1982).

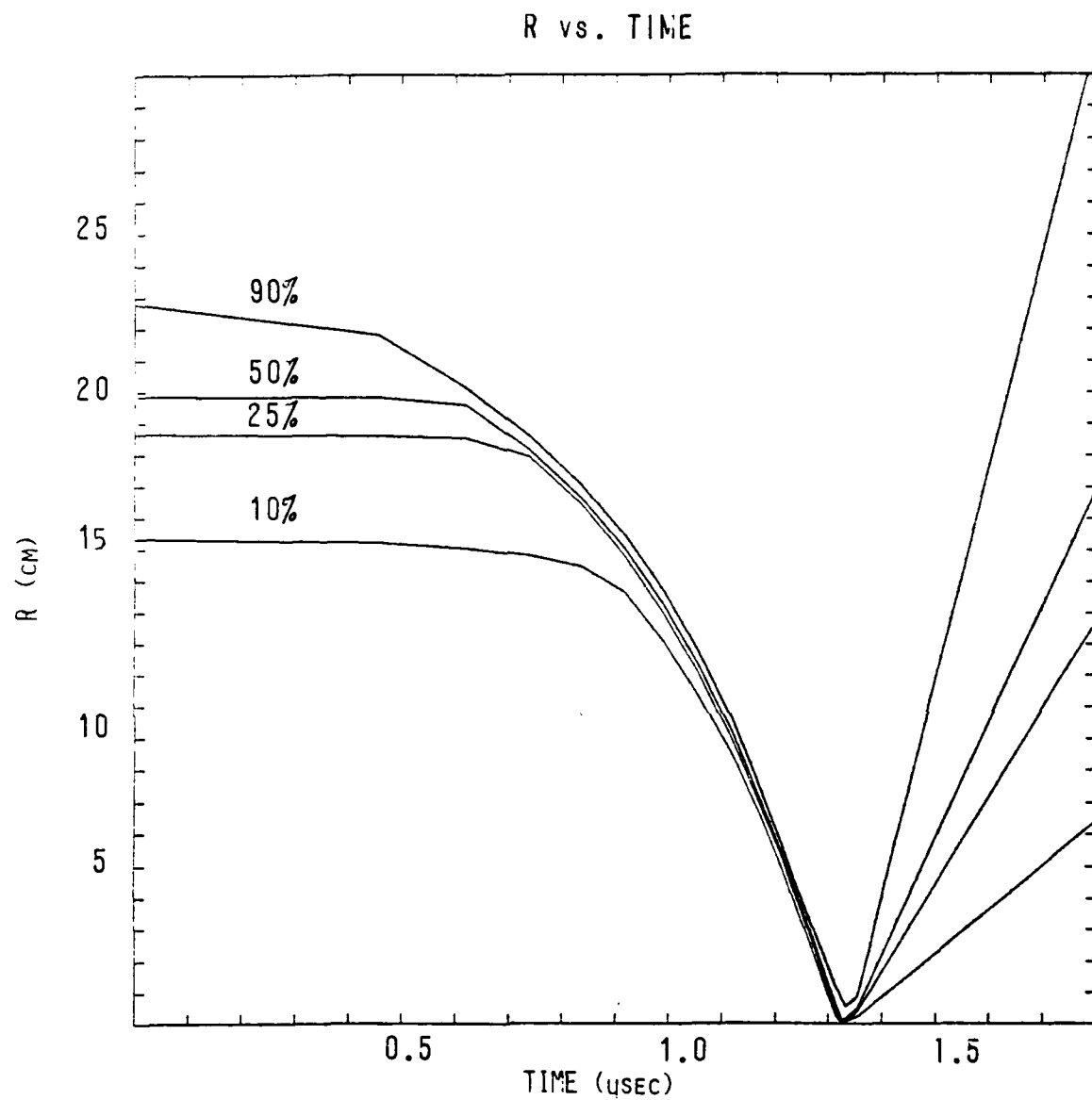


Fig. 1. Time history of several mass lines for the 120  $\mu$ g/cm Argon implosion.

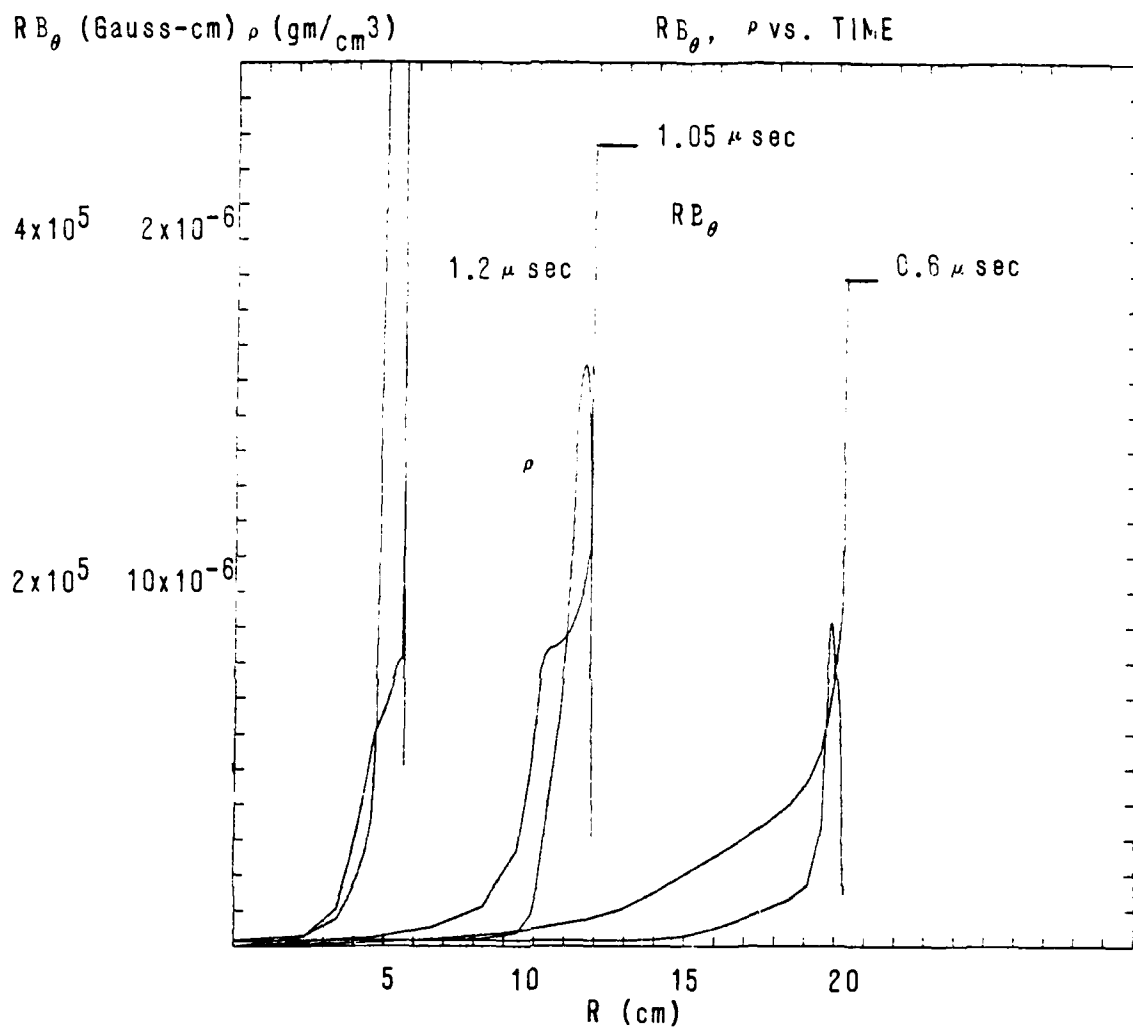


Fig. 2. Magnetic field and density profiles at several times for the 120  $\mu$ gm/cm Argon implosion.

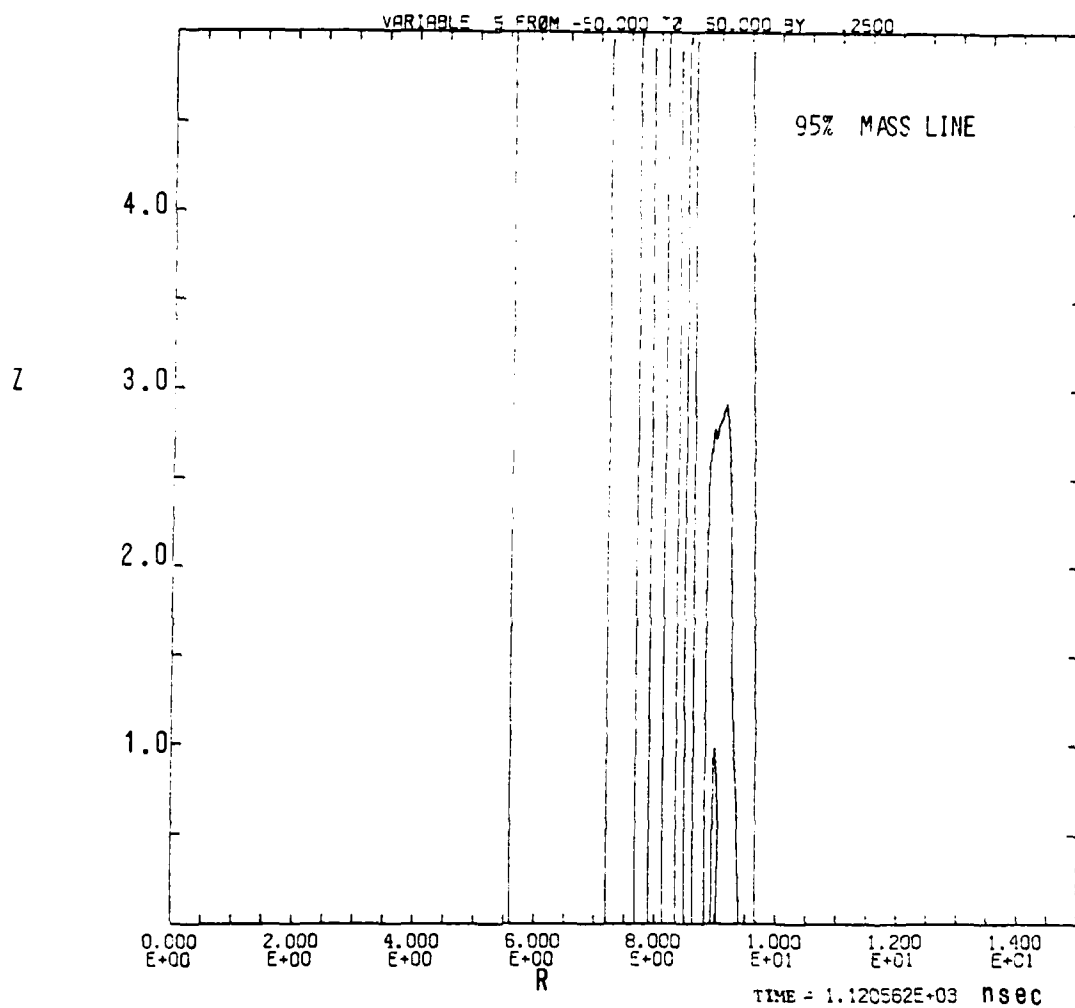


Fig. 3. Density contours out to the 95% mass line at 1.12  $\mu$ sec.

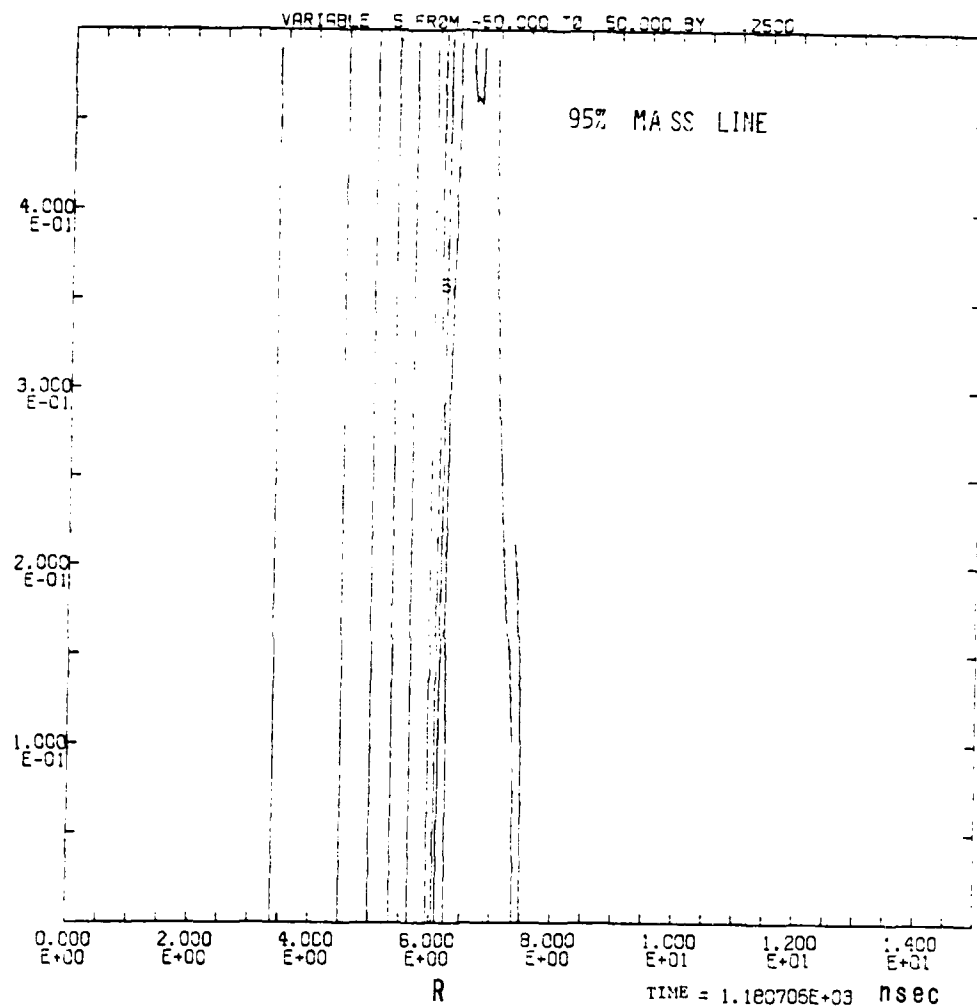


Fig. 4. Density contours out to the 95% mass line at 1.18  $\mu$ sec.

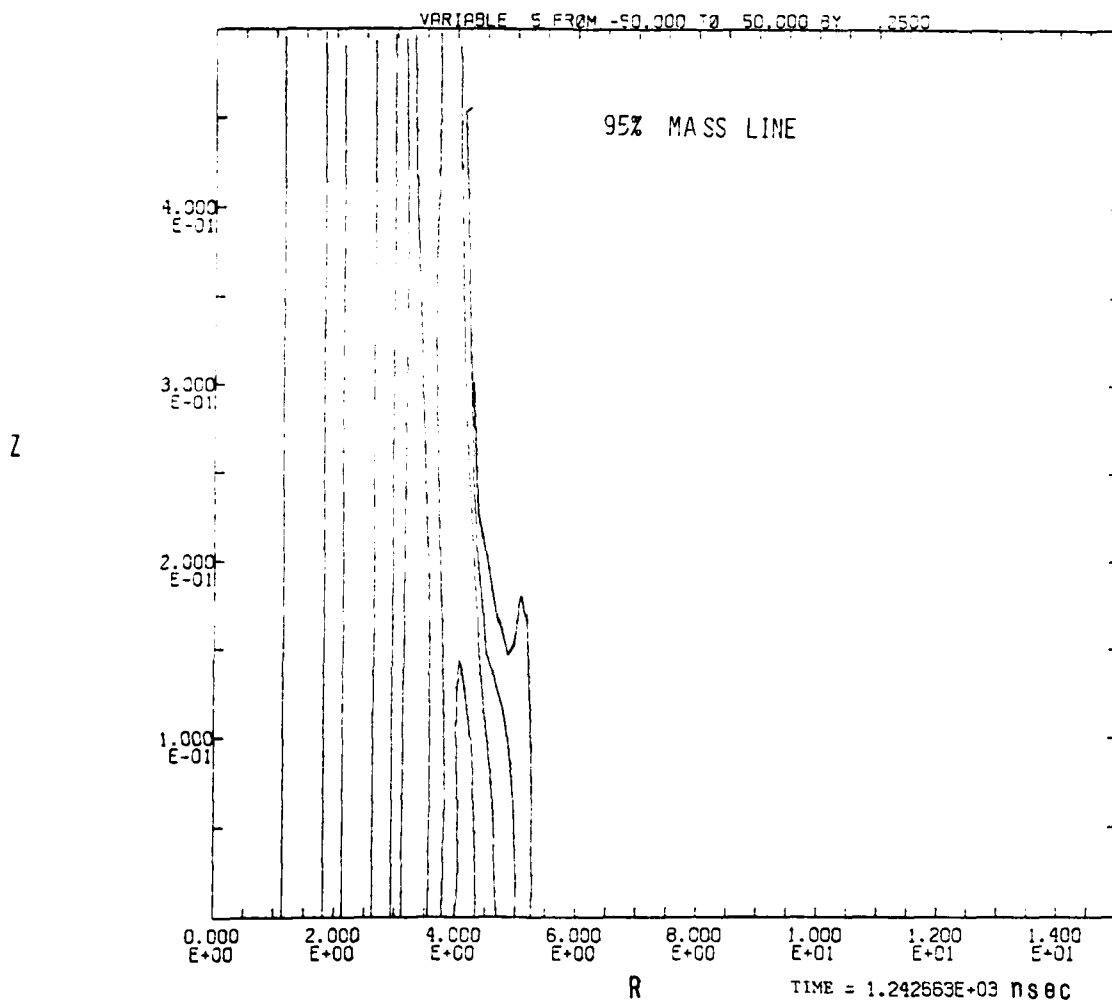


Fig. 5. Density contours out to the 95% mass line at 1.24  $\mu$ sec.

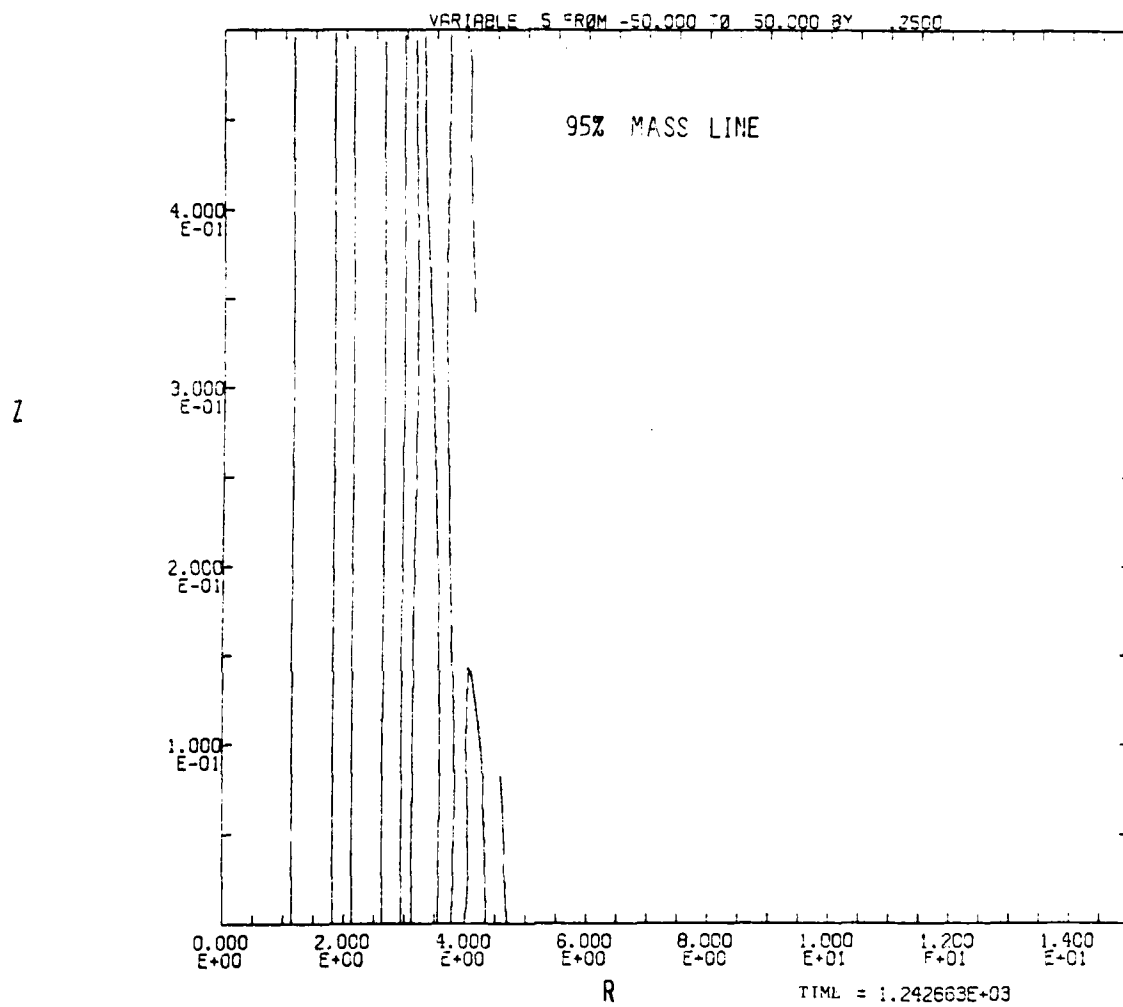


Fig. 6. Density contours out to the 80% mass line at 1.24  $\mu$ sec.



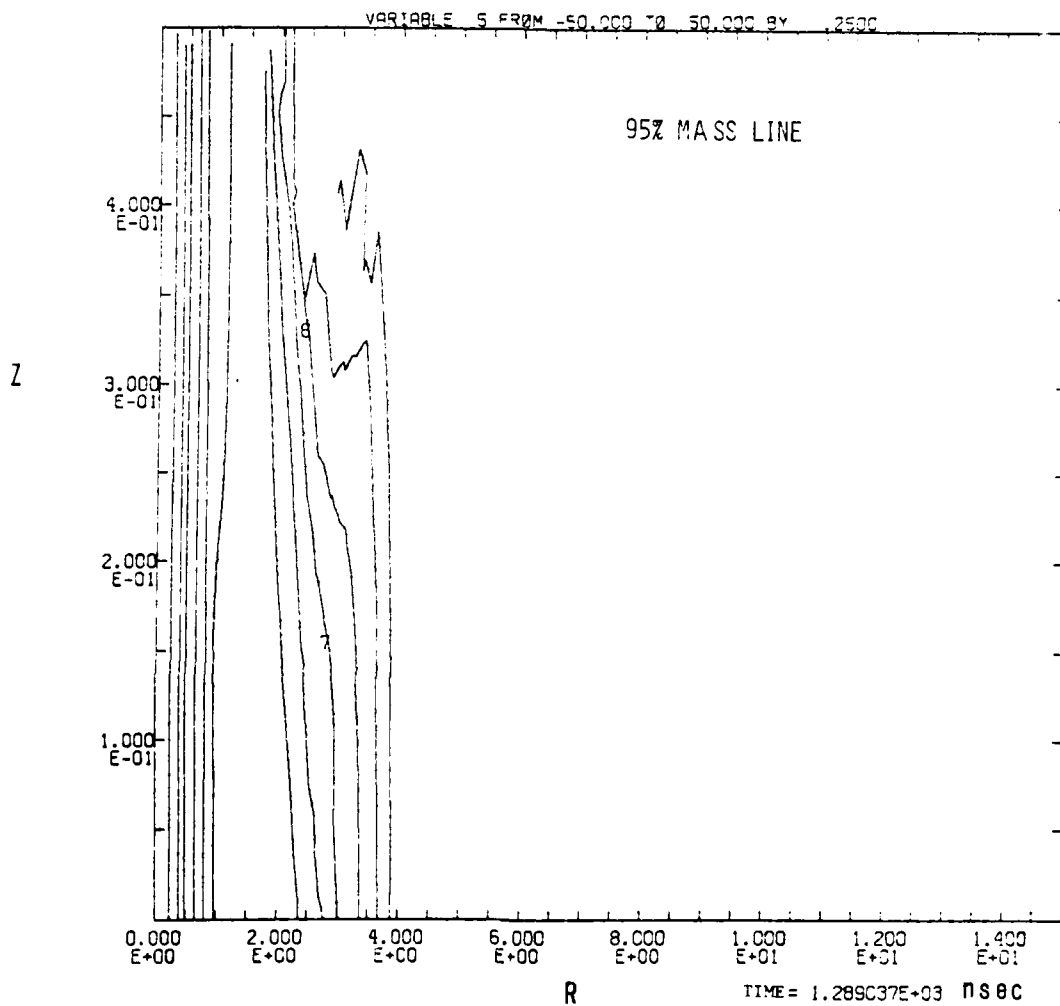


Fig. 7. Density contours out to the 95% mass line at 1.29  $\mu$ sec.

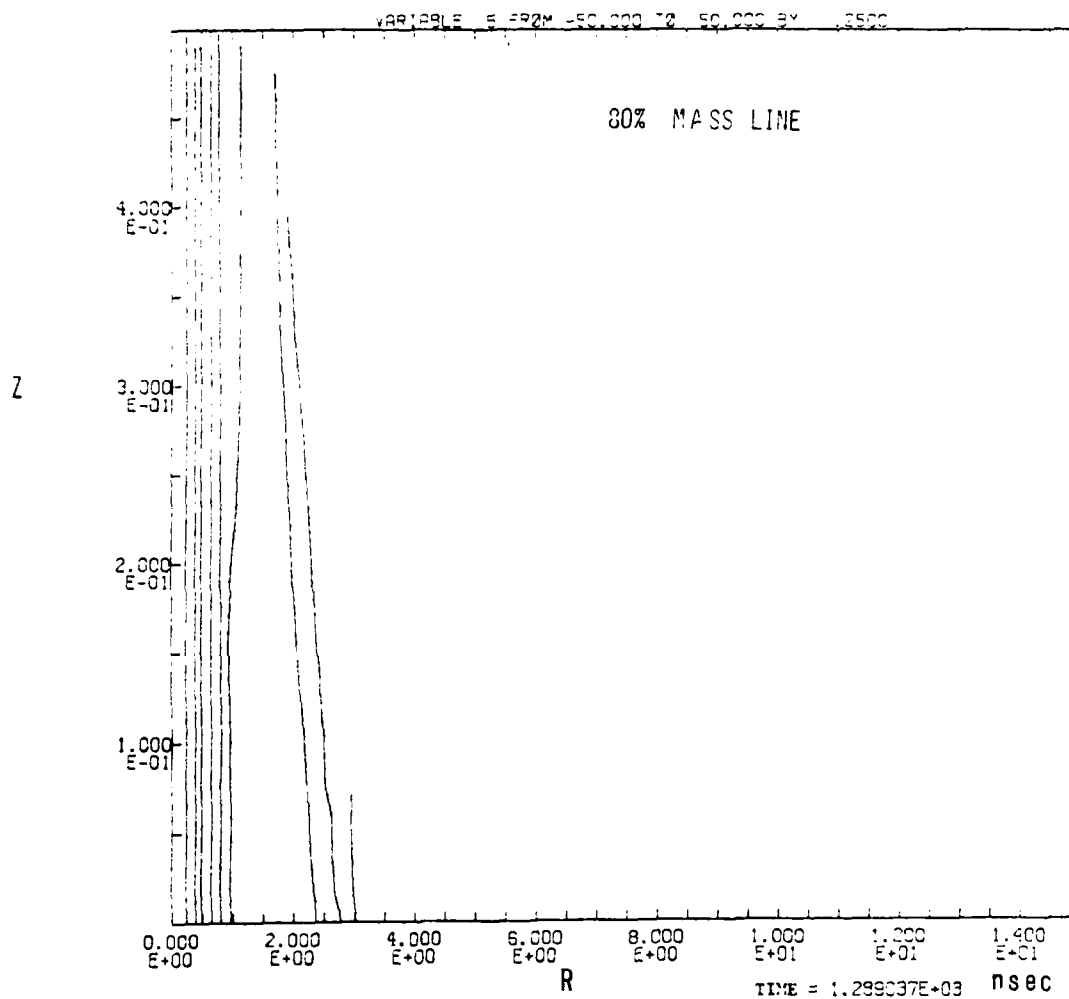


Fig. 8. Density contours out to the 80% mass line at 1.29  $\mu$ sec.

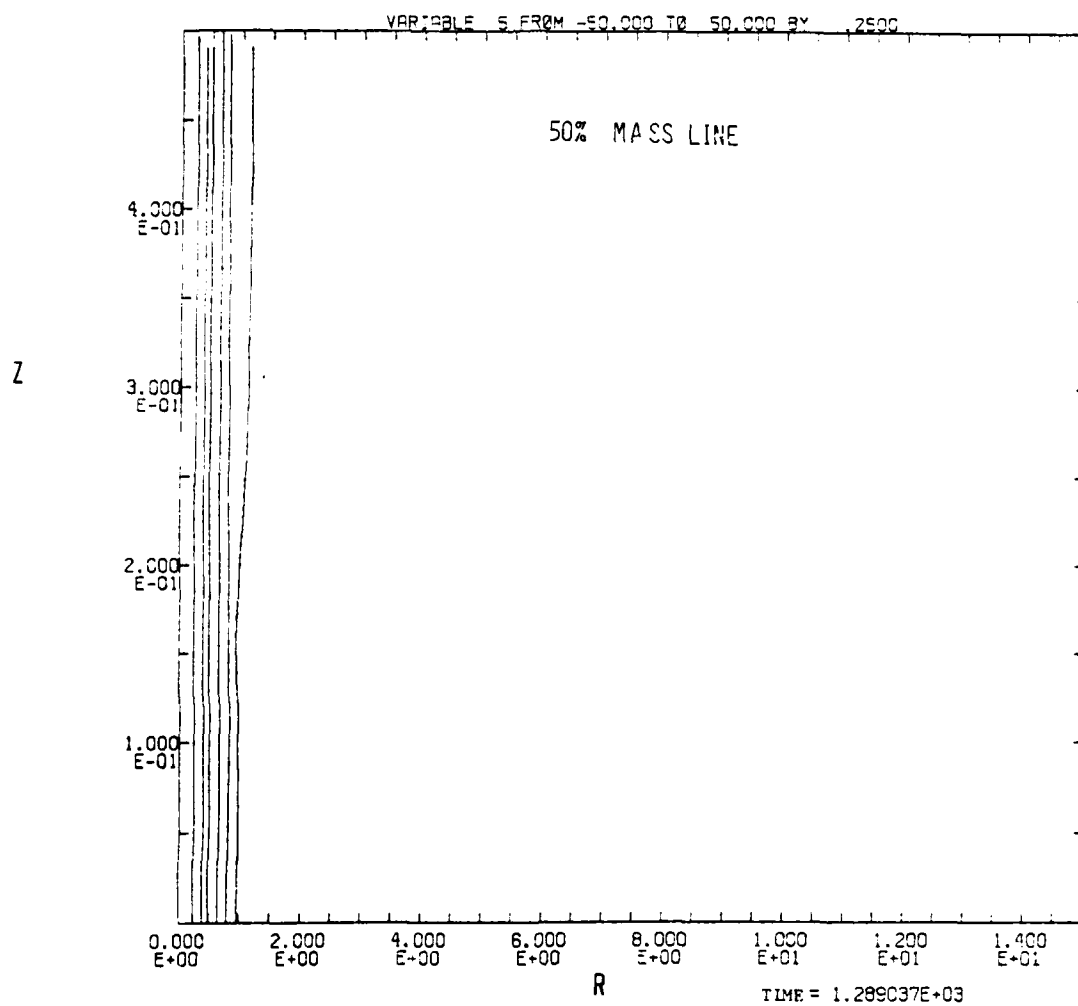


Fig. 9. Density contours out to the 50% mass line at 1.29  $\mu\text{sec}$ .

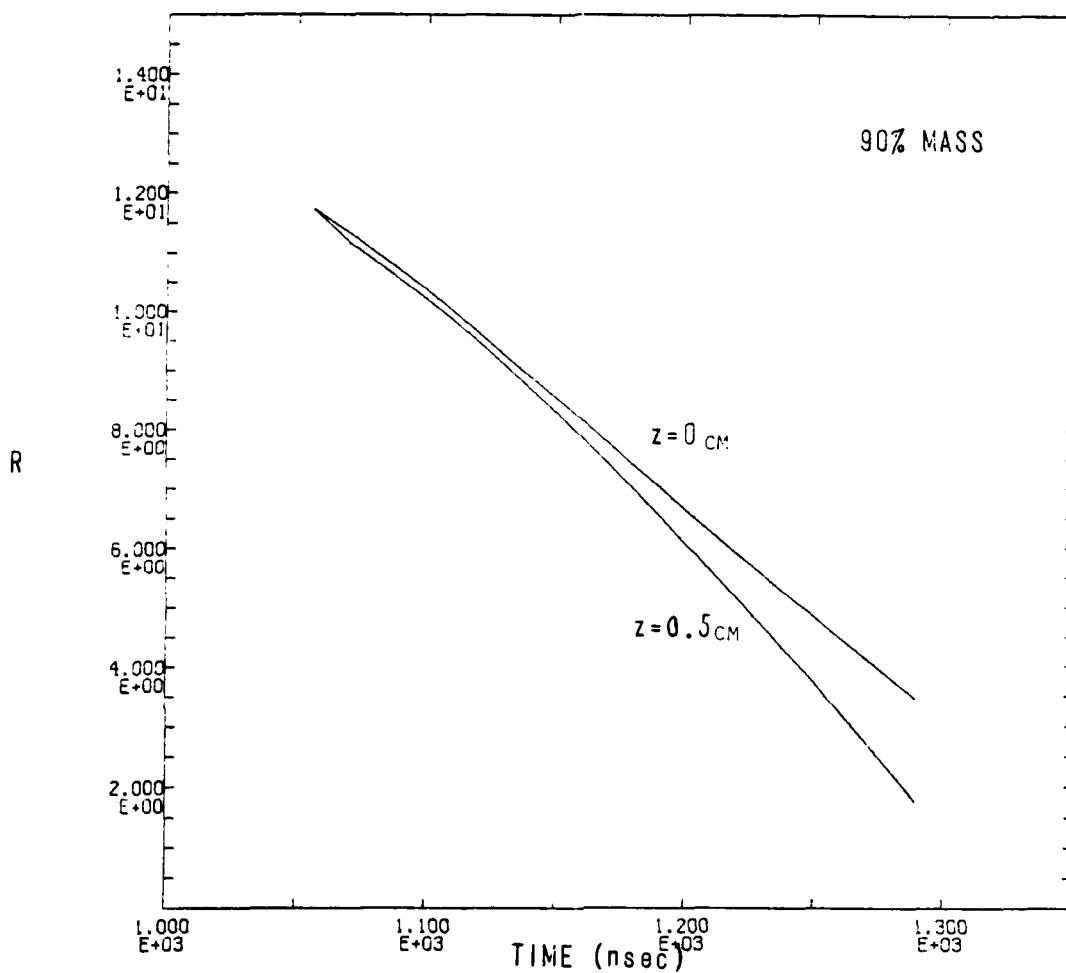


Fig. 10. Time of history of  $z=0 \text{ cm}$  and  $z=0.5 \text{ cm}$  modes of the 90% mass line.

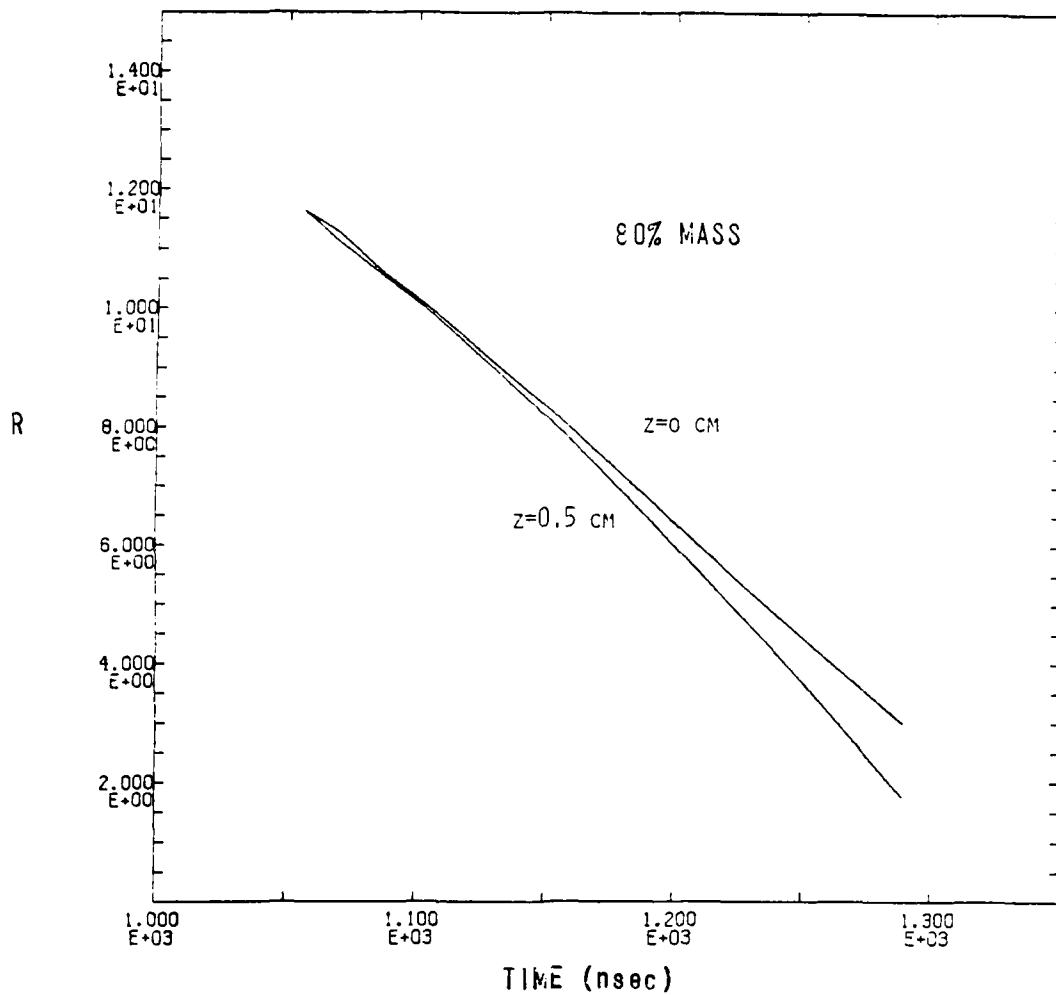


Fig. 11. Time history of the  $z=0$  cm and  $z=0.5$  cm modes of the 80% mass line.

# GROWTH RATE

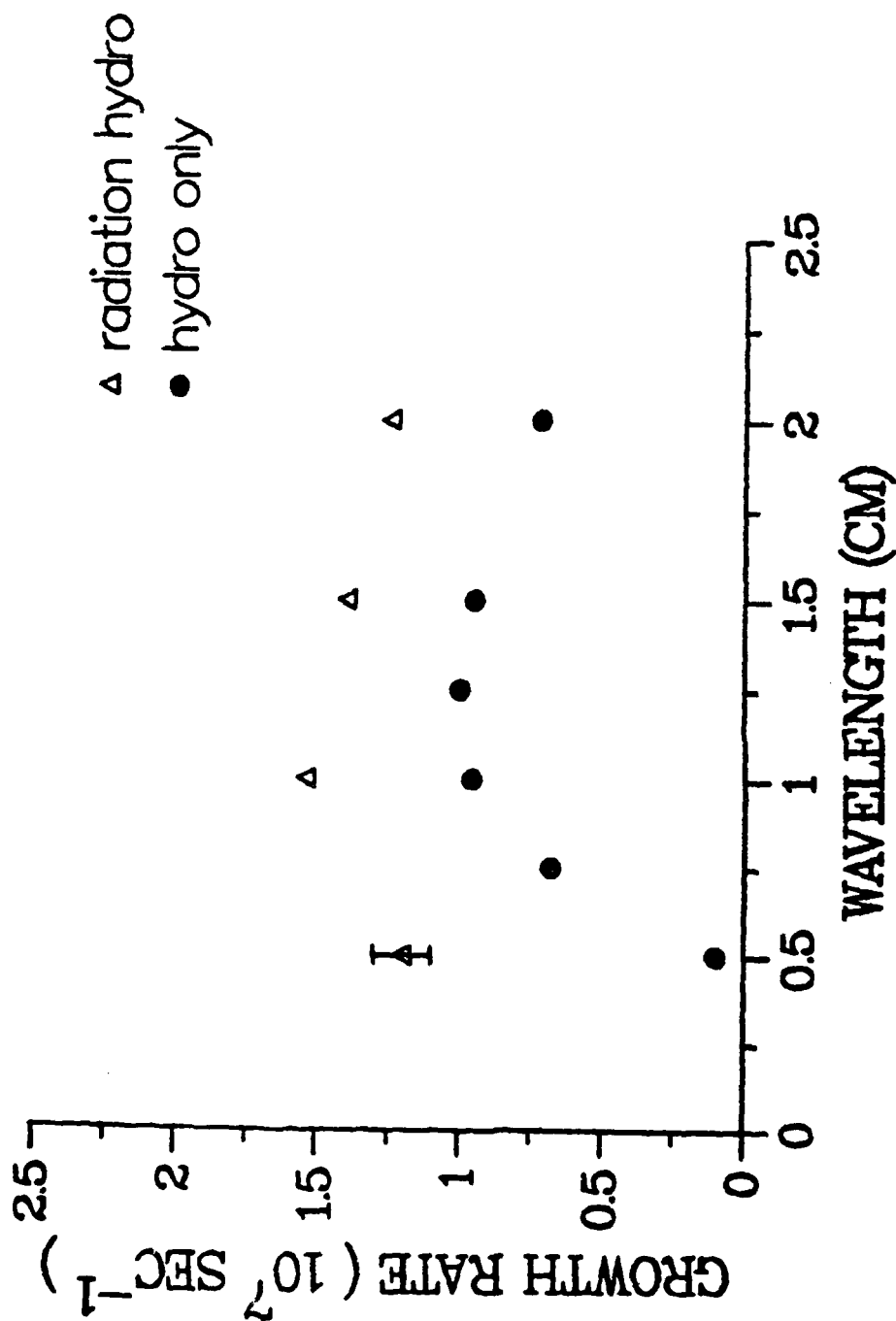


Fig. 12. Growth rate curves for several runs with and without radiation turned on. The error bar depicts a typical variance in measuring the growth rate at different times.

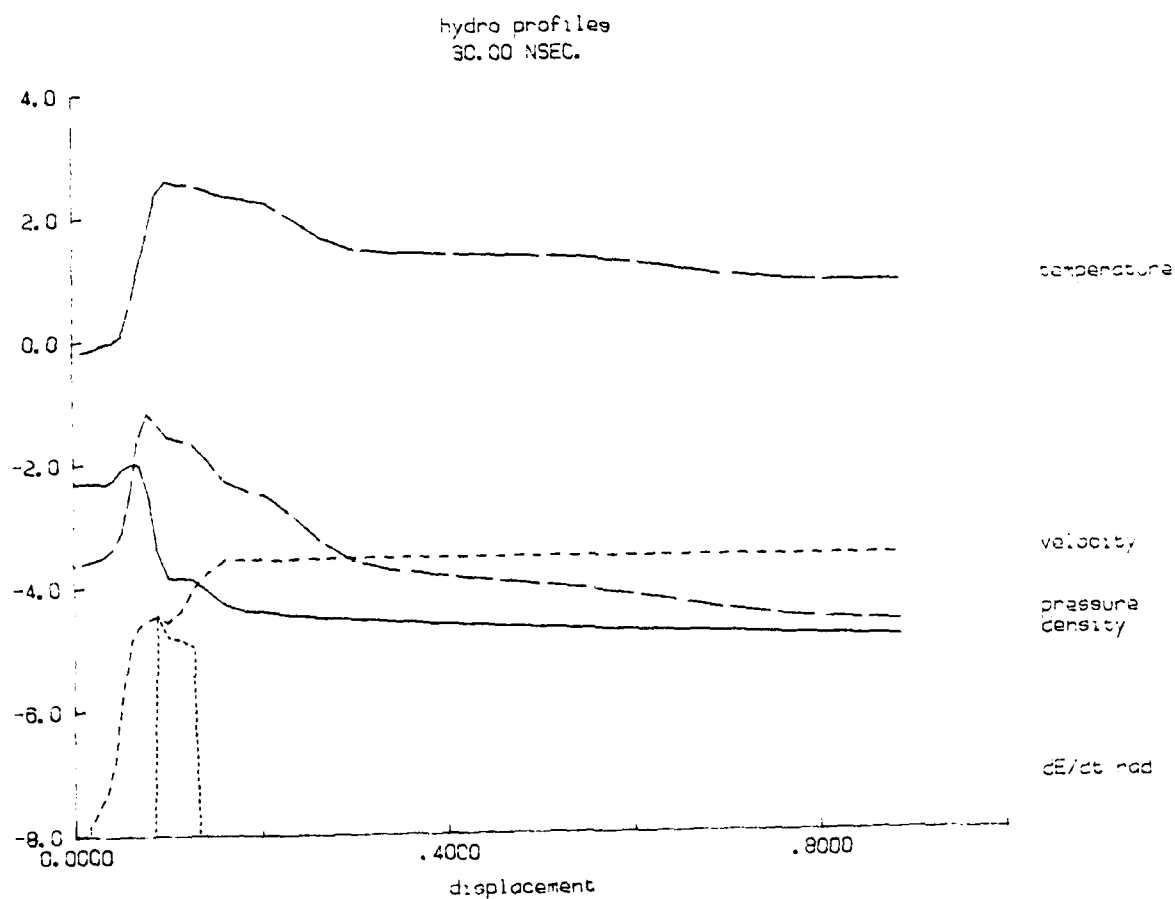


Fig. 5. Profiles at 30.0 nanoseconds. Peak temperature exceeds 300 eV. Shocks propagating radially inward in core plasma and radially outward in puff-gas.

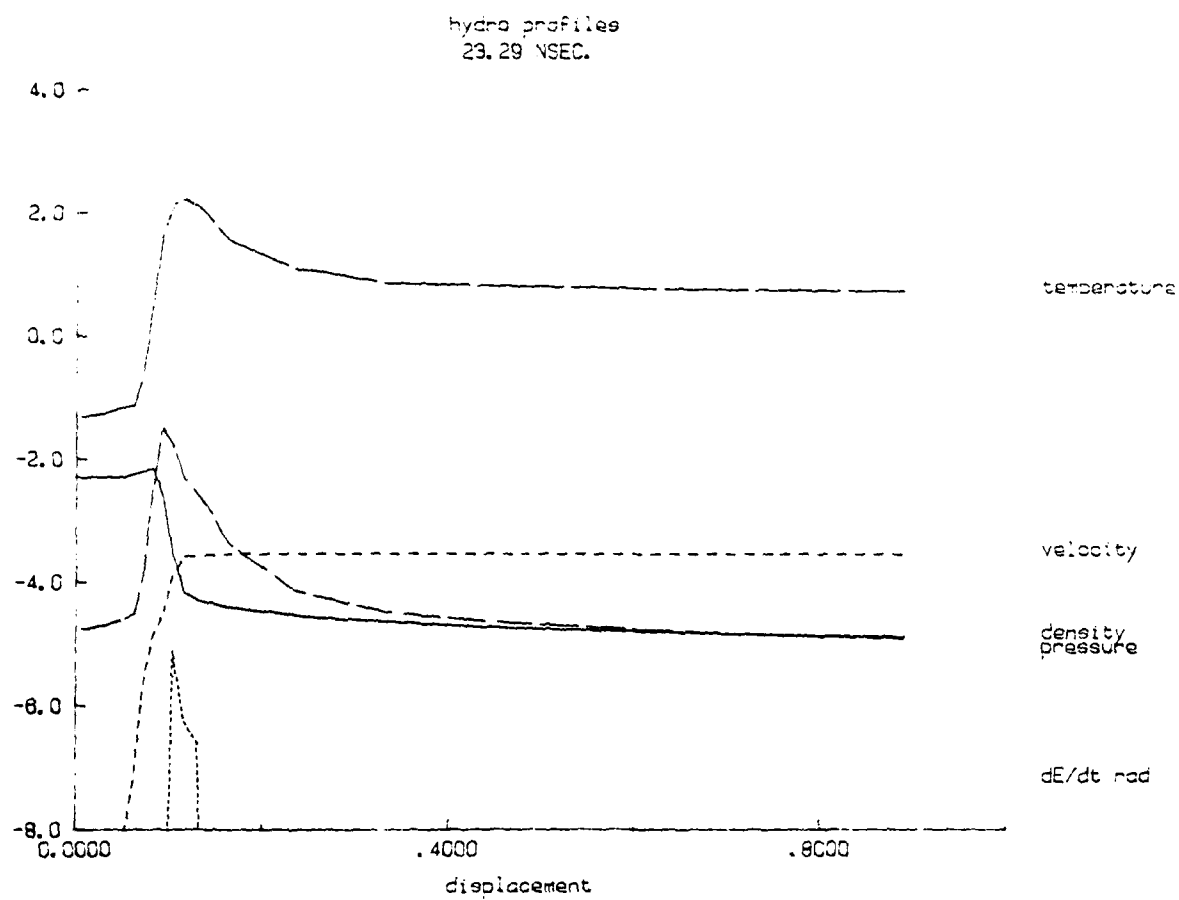


Fig. 4. Profiles at 23.3 nanoseconds. Stagnation phase: contact with central core plasma has commenced. Temperature at interface exceeds 100 eV.



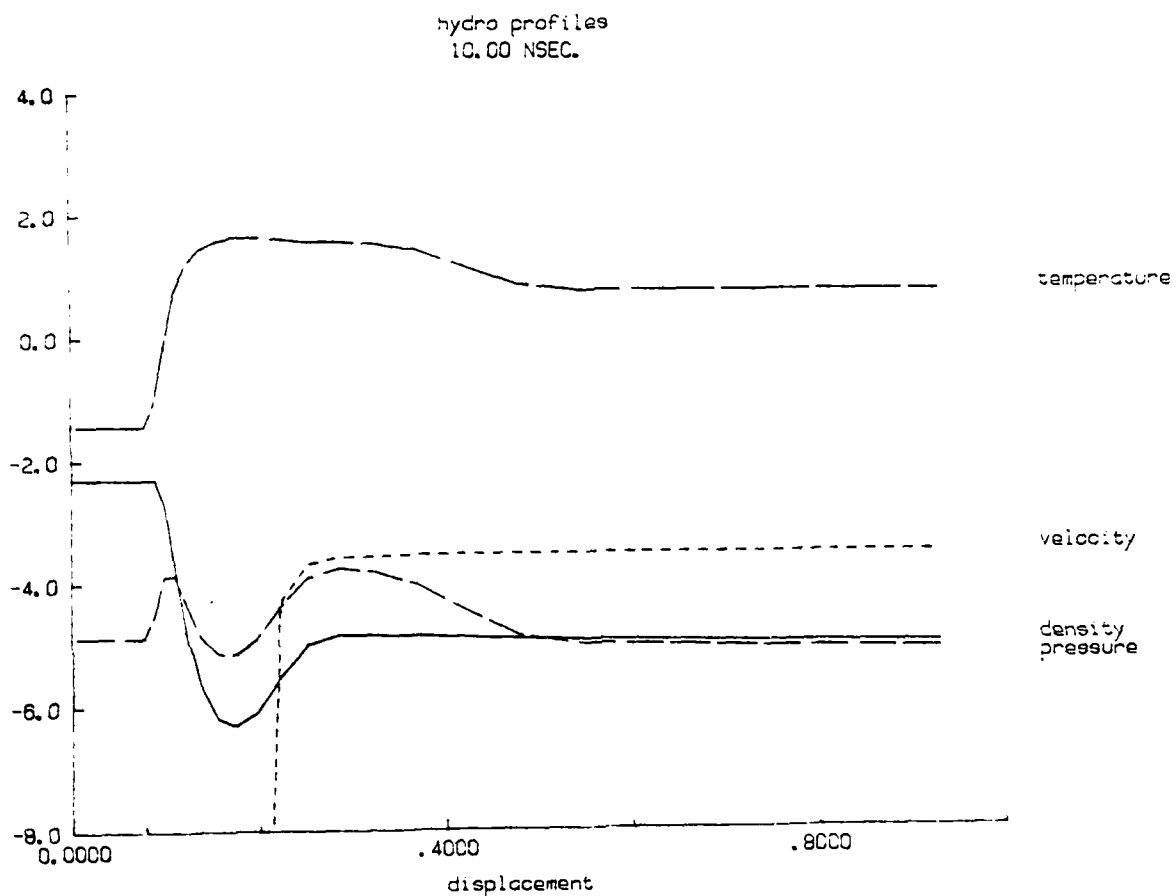


Fig. 3. Profiles at 10.0 nanoseconds. Coasting phase: forward edge of puff-gas has been heated to a few tens of eV through accretion of background plasma.

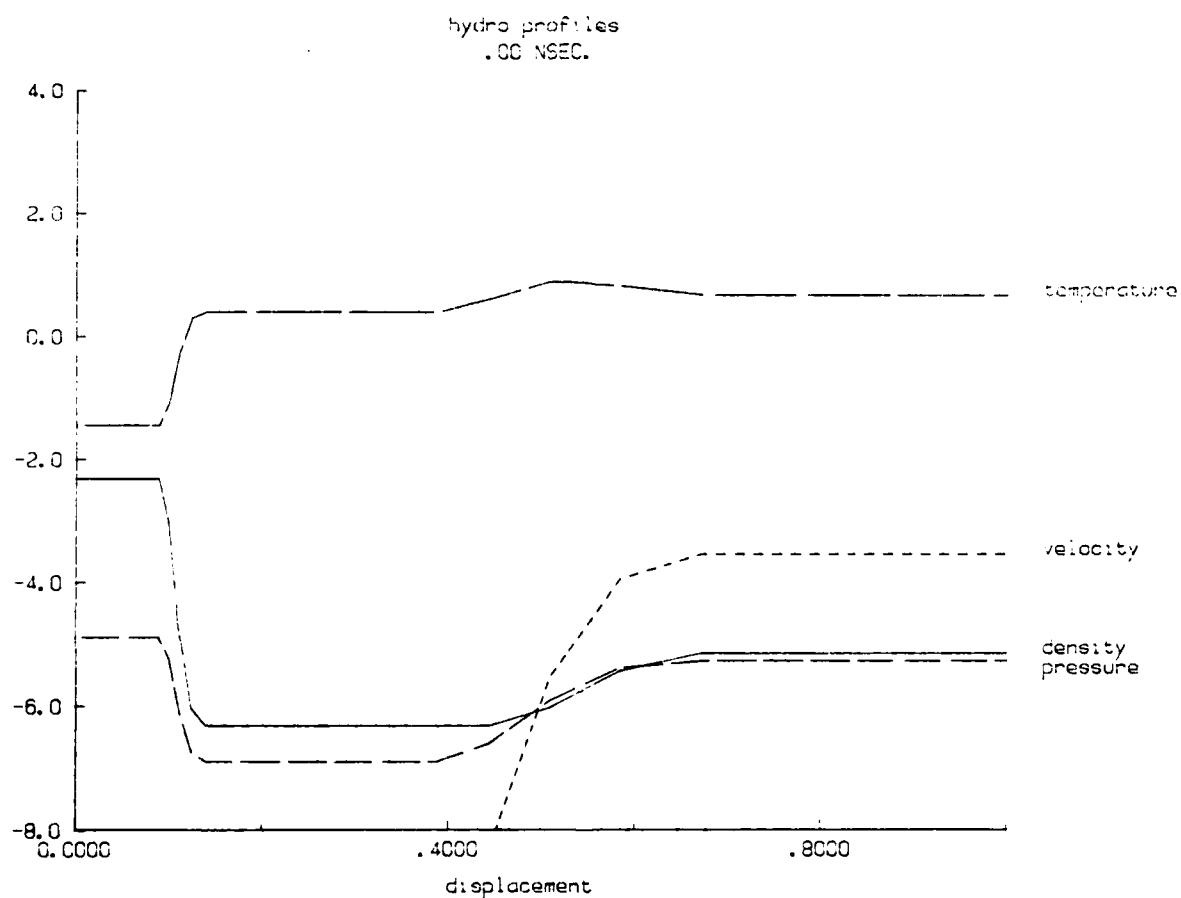


Fig. 2. Profiles at 3.75 picoseconds. Radial displacement is given in cm.,  $\log_{10}$  density in  $\text{g/cm}^3$ ,  $\log_{10}$  temperature in eV,  $\log_{10}$  pressure in  $\text{ergs/cm}^3 \times 10^{-12}$ ,  $\log_{10}$  radial velocity in  $\text{cm/nsec} \times 10^{-2}$  and  $\log_{10} \dot{\epsilon}_{\text{rad}}$  in  $\text{ergs/cm}^3\text{-nsec} \times 10^{-14}$ .

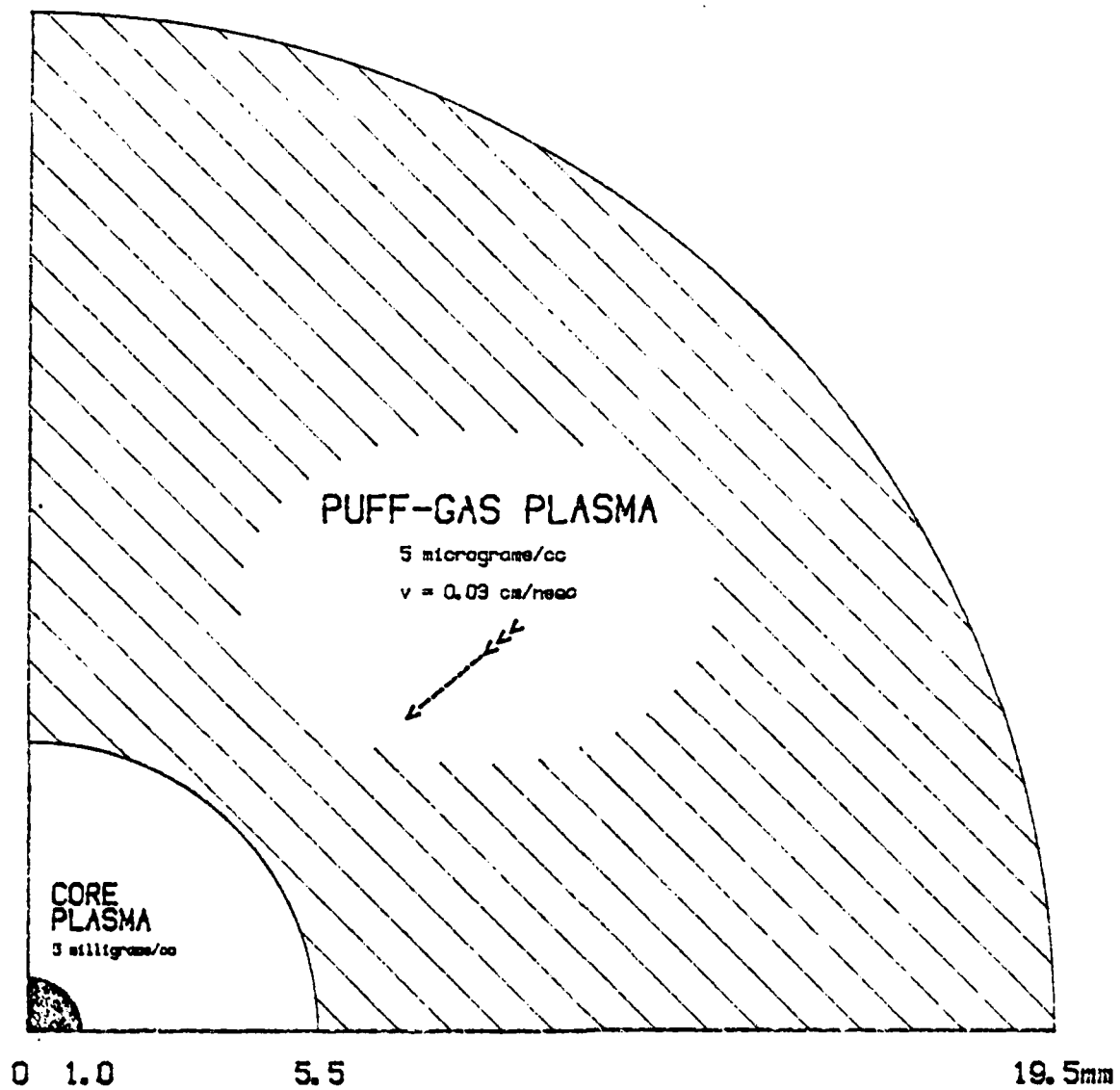


Fig. 1. Initial configuration: Puff gas implosion onto a low density core plasma.

which was compared to the self-consistent simulation, neglected radiation but included ionization dynamics. At certain times and regions, the local energy of ionization and excitation substantially exceeded the local thermal energies. It is probable that a pure "hydrodynamic" calculation with simplified prescriptions for ionization energy and average ionization state would produce a substantially different plasma evolution.

Since radiation plays such a crucial role, it must be generated and transported accurately. As we have shown, optically thin radiation ignores important transport of energy by radiation and grossly overestimates losses. LTE or coronal models for the level populations will also lead to inaccurate energetics. We found that the atomic populations in the regions of peak radiative emission were substantially different from corresponding LTE or coronal populations, in some cases by orders of magnitude.

The neon model which we employed was a relatively modest one, with only 27 atomic levels and 13 emission lines. We have available more extensive neon models with nearly a hundred levels and with hundreds of lines. How much accuracy has been given up by using a reduced model? Experience has shown that simple models can underestimate radiative losses by perhaps a factor of two. Thus, we plan to perform an identical calculation with a full neon model, and it is expected that the radiation yield will be even higher.

Corresponding profiles of density, temperature, pressure and velocity are shown in Figs. 13 and 14. At 30.0 nanoseconds (Fig. 13), the profiles are very similar in the interface region. However, the role of radiation in transporting energy is clearly evident. The dense core is still very cold compared with the complete simulation with radiation transport. Also, the temperatures through the forward half-centimeter of the puff-gas plasma are a factor of about 3 lower than in the full simulation. A comparison with the profiles in Figs. 5 through 7 suggest how greatly "thin" radiation can overestimate energy loss.

In spite of the differences in the calculations, assembly occurs at about the same time. The situation at 50.0 nanoseconds is shown in Fig. 14. There are qualitative similarities with Fig. 7, but substantial differences are also evident. Temperatures and densities differ by at least a factor of two almost everywhere. Also, a substantial portion of the plasma is moving radially outward by this time.

A corresponding energy history of this simulation is shown in Fig. 15. The early history is similar to that shown in Fig. 10. By 30 nanoseconds, however, it is evident that substantially more energy resides in thermal and ionization energies. The relative minimum in kinetic energy occurs earlier and is not as sharp. As can be seen from the radiation curve, if radiation post-processing had been employed, all of the available plasma energy would have been lost within the first 30 nanoseconds.

#### IV. CONCLUSIONS

A puff-gas imploding onto a central core plasma has promise as a reliable way to achieve sufficiently high density and temperature over sufficiently large volumes and timescales to efficiently convert kinetic energy to radiation. In the case we have studied, a neon puff-gas imploding onto a neon core plasma, approximately two-thirds of the total plasma energy was converted to K and L-shell radiation by 100 nanoseconds.

Because the radiative energy loss and the transport of radiation in the plasma substantially modify the hydrodynamic response, a self-consistent calculation, linking radiation and fluid transport with the ionization dynamics, must be performed. The "hydrodynamic" calculation,

The energy history of the plasma throughout the first 120 nanoseconds is shown in Fig. 10. The energy in various categories is shown as a function of time, on a logarithmic scale from  $10^5$  to  $10^{11}$  ergs/cm.

Initially, about 98% of the total energy is kinetic; the other 2% is in thermal and ionization energies. The energy radiated away begins to increase sharply just before 20 nanoseconds, as the puff gas hits the central core. Thermal and ionization energies also begin to increase sharply at this time. Kinetic energy goes through a well defined minimum at about 60 nanoseconds. Although peak compression on axis occurs at about 50 nanoseconds, substantial portions of the puff gas plasma continue to move inwards until about 60 nanoseconds. Notice that by 60 nanoseconds, almost half of the total plasma energy has been radiated away. By 200 nanoseconds, about 2/3 of the total energy has been converted to radiation. This makes it very difficult to justify a "hydro-only" calculation, or a calculation where the radiation energetics are not carefully performed.

Figure 11 shows the calculated emission spectrum from the plasma at 23.3 nanoseconds, just after the puff-gas has contacted the central core. The energy range is 10 eV to 10 keV, and the spectral intensity is in units of ergs/cm-keV-sec. At this time, there is substantial L-shell emission, but little K-shell radiation. Most of the L-shell radiation is coming from the denser, cooler portion of the interface region, while the K-shell radiation is coming mostly from the hotter but less dense portion just outside the core plasma.

At 50.0 nanoseconds (Fig. 12), the emission spectrum shows substantially more power in the K-shell and the L-shell. A broader annulus of plasma, situated outside the core plasma, is producing most of the radiation. Although the very dense plasma on axis is radiating strongly, its volume is small, and the temperature is relatively low.

A similar calculation was performed without radiation cooling, but with detailed atomic physics, so that the ionization energies and average ionization numbers would be self-consistently calculated. Although the radiative cooling was turned off, optically thin radiation was calculated for comparison with the simulation discussed above.

inwards. Some radial compression of the puff-gas is in evidence. Thermal conduction has produced a nearly isothermal region between the outer edge of the core plasma and the forward millimeter of the puff-gas. Radiative effects at this time are negligible.

At  $t = 23.3$  nanoseconds (Fig. 4), the puff-gas is in full contact with the core. The compression at the interface has created a large overpressure, and the temperature in this region exceeds 100 eV. A narrow region of radiative cooling is situated exactly at the interface. Adjacent regions are net absorbers of radiation - they are being heated by the absorption of soft x-rays produced near the interface.

At  $t = 30.0$  nanoseconds (Fig. 5), the peak temperature near the interface exceeds 300 eV. The large overpressure has caused shocks to propagate radially inward in the core plasma, and radially outward in the puff-gas. Heating from the soft x-rays produced in the interface region is evident in the dense core. Radiation heating is also taking place deep in the puff gas. The effects of radiation transport will be more clearly seen when comparison is made with hydro-only profiles.

At 40.0 nanoseconds (Fig. 6), the shocks are more fully developed. Thermal conduction is creating a nearly isothermal region near the leading edge of the puff-gas.

At 50.0 nanoseconds (Fig. 7), the inward-going shock has reached the origin. Although the density approaches solid density on axis, the plasma temperature there is still only a few tens of eV.

By 60.0 nanoseconds (Fig. 8), portions of the plasma, including the dense core, are moving radially outwards. The outward going shock is still in evidence, and the outer edge of the puff-gas is near its minimum radius (about 0.5 cm).

Finally 70.0 nanoseconds (Fig. 9), the entire plasma is moving radially outwards. The core plasma remains cool, since the density is still high enough to retard thermal conduction. Furthermore, the radiative emission of this region is in approximate balance with the radiative absorption.

where  $F_{pk}$  is the rate of energy loss in zone  $k$  due to a discrete radiative process (or frequency group)  $P$ , and  $C_{pkj}$  is the radiative coupling of zone  $k$  to zone  $j$  for that process. The couplings are functions of opacity, integrated over process and photon path. In the probabilistic model, a matrix of couplings must be computed for each bound-bound, bound-free and free-free process; for the multifrequency model, they must be computed for each discrete frequency. In this way, the net cooling and heating by radiation emission and absorption among the various zones of the plasma is accounted for accurately.

### III. RESULTS

We have performed a calculation involving a cylindrical neon puff gas of density  $5 \times 10^{-6} \text{ g/cm}^3$ , with inner radius 0.55 cm and outer radius 1.95 cm, imploding radially at a velocity of  $3 \times 10^7 \text{ cm/sec}$  on a uniform neon central core plasma of density  $5 \times 10^{-3} \text{ g/cm}^3$  and radius 0.10 cm. The initial configuration is as shown in Fig. 1. The temperature of the puff gas is taken to be 5eV initially, and the core plasma temperature is about .04eV. There is assumed to be a tenuous background plasma in between the puff gas and core plasmas, of density  $5 \times 10^{-7} \text{ g/cm}^3$ .

Profiles of density, temperature, total pressure, velocity and radiative cooling at various times in the calculation are given in Figs. 2 through 9. The ordinate in all of the plots is logarithmic, ranging from  $10^{-8}$  to  $10^{+4}$ . The various plasma profiles are suitably scaled so that they can be plotted together: density in  $\text{g/cm}^3$ , temperature in eV., pressure in  $\text{ergs/cm}^3 \times 10^{-12}$ , velocity in  $\text{cm/nsec} \times 10^{-2}$  and radiative cooling in  $\text{ergs/cm}^3\text{-nsec} \times 10^{-14}$ . The abscissa is linear, and ranges from 0.0 (the central axis) to 1.0 cm.

At  $t = 3.75$  picoseconds (Fig. 2), the plasma is very close to the initial configuration. There is a slight warming of the plasma evident at the background-puff gas interface. Note that only the inner 1.0 cm of the calculation is shown; the puff gas initially extends to 1.95 cm.

At  $t = 10.0$  nanoseconds (Fig. 3), the forward edge of the puff-gas has been heated to a few tens of eV through accretion of the background plasma. At this time, the puff-gas plasma is essentially coasting radially



### c. Radiation Emission and Transport

Radiation emission from a plasma and its opacity are dependent on the local atomic level population densities. Except for optically thin plasmas, however, the level populations depend on the radiation field, since optical pumping via photoionization and photoexcitation can produce significant population redistribution. Thus, the ionization and radiation transport processes are strongly coupled and must be solved self-consistently. In this model, an iterative procedure<sup>11</sup> is used, where level populations are calculated using the radiation field from the previous iteration, then using these populations to calculate a new radiation field and recalculating populations until convergence is reached.

Three distinct radiation transport schemes have been developed, and can be used interchangeably in the code: a probabilistic scheme, a multifrequency scheme and a hybrid method. Descriptions of these transport methods have appeared elsewhere.<sup>12,13</sup> The probabilistic model was employed in the present calculation, since the total plasma mass is relatively small.

The probabilistic model<sup>12</sup> forms local angle and frequency averaged escape probabilities for each emission line and for each bound-free process. Free-free radiation is treated with a multifrequency formalism. The radiation transport and emission spectra are calculated from these escape probabilities. The method can treat comprehensive atomic models and provides good overall energetics, but cannot calculate certain spectral details and becomes inaccurate at very high optical depths.

In all of the models outlined above, local ionization state-dependent inner-shell opacities are included, since these processes are very important in the cool, dense plasma regions. Inner-shell photoionization cross sections for the neutral element are taken from the fits by Biggs and Lighthill,<sup>14</sup> and the positions of the ionization-dependent absorption edges are taken from the Hartree-Fock calculations of Clementi and Roetti.<sup>15</sup>

The local rate of energy change in zone  $j$ , due to radiation transport is given by

$$\epsilon_j = - \sum_p (F_{pj} - \sum_k C_{pkj} F_{pk}) \quad (9)$$

## b. Ionization and Atomic Physics

The ionic populations in the plasma may be characterized by a set of atomic rate equations of the form

$$\frac{df_i}{dt} = \sum_j W_{ji} f_j - \sum_i W_{ij} f_i \quad (6)$$

where  $f_i$  is the fractional population of atomic level  $i$ , and  $W_{ji}$  is the net reaction rate describing the transition from initial state  $j$  to final state  $i$ . An equation of this type is constructed for each of the atomic levels included in the model.

For sufficiently dense plasmas of the sort we expect to model with the implosion code, the effective populating and depopulating rates are generally fast compared with the hydrodynamic response. An equilibrium assumption can be justified, which involves dropping the explicit time dependence in Eq. (6). The plasma is then said to be in collisional-radiative equilibrium (CRE),<sup>3</sup> whereby the plasma ionization state responds instantaneously to changes in hydrodynamic quantities.

The rate coefficients that are used to calculate the populating and depopulating rates,  $W_{ji}$ , are calculated using various scattering techniques. The processes included in this calculation and the methods used in calculating the corresponding rate coefficients are summarized elsewhere.<sup>4-10</sup>

Once the set of rate equations (including the radiation transport) has been solved for the level populations,  $f_i$ , the electron density can be calculated,

$$N_e = \sum_i z_i f_i N_I \quad (7)$$

where  $z_i$  is the ionic charge of level  $i$  and  $N_I$  is the total ion density.

The ionization and excitation energy can also be calculated by

$$\epsilon_i = \sum_i \chi_i f_i N_I, \quad (8)$$

where  $\chi_i$  is the energy of level  $i$ , measured from the ground state of the neutral atom.

$$\frac{D\rho}{Dt} = \frac{\partial \rho}{\partial t} + \nabla \cdot (\rho \mathbf{u}) = 0 \quad (1)$$

$$\frac{D(\rho u)}{Dt} = -\nabla P \quad (2)$$

$$\frac{D\epsilon_T}{Dt} = -\nabla \cdot (\mathbf{u}P) + \dot{\epsilon}_{\text{rad}} + \nabla \cdot (\eta \nabla T) \quad (3)$$

where  $\rho$  is mass density,  $\mathbf{u}$  is velocity,  $P$  is pressure,  $\epsilon_T$  is total energy density,  $\dot{\epsilon}_{\text{rad}}$  is the rate of energy loss or gain due to radiation,  $\eta$  is the thermal conductivity, and  $N$  is the ion density. The thermal conduction is calculated implicitly, using an iterative Crank-Nicholson scheme.

Since densities did not exceed solid density in this study, a simple equation of state was assumed with

$$P = \frac{2}{3} (\epsilon_T - \frac{1}{2} \rho u^2 - \epsilon_I) , \quad (4)$$

where  $\epsilon_I$  is the potential energy due to ionization and excitation. A non-ideal equation of state taking account of ionization energy and degeneracy pressure is employed in cases where the density exceeds solid density. A single temperature model was employed,

$$kT = \frac{P}{(\rho/m_I)(1+\bar{Z})} , \quad (5)$$

where  $m_I$  is ion mass, and  $T$  is temperature. The ionization energy,  $\epsilon_I$ , and effective charge,  $\bar{Z}$  are calculated from the ionization-radiation equations which are explained below. A single temperature assumption is valid in the core plasma, where the equilibration time is of the order of picoseconds, and it is adequate in the stagnation region, where the equilibration time can be of the order of nanoseconds. In the blowoff plasma, it is a marginal approximation, but the consequences are small, since little radiation is emitted from this region, and since most of the thermal energy is carried by the electrons in the blowoff.

The local rate of change of energy due to radiation transport,  $\dot{\epsilon}_{\text{rad}}$ , will be discussed below.

## D. Implosion of a Neon Puff-Gas Plasma Onto a Low-Density Plasma

### I. INTRODUCTION

Z-pinch implosions of puff-gas plasmas onto low density foams are presently being carried out at Sandia National Laboratory. The collapse of an imploding puff-gas on a central core produces hot moderate density plasma over reasonably large volumes and timescales. Sandia reports high radiative conversion efficiencies from relatively clean, reproducible implosions. We have simulated a typical Sandia Z-pinch experiment with a self-consistent 1D radiation-hydrodynamic scheme. Such simulations can help in understanding the underlying physics of these experiments, and can lead to diagnostic and predictive capability.

### II. THEORETICAL MODEL

Imploding a cylindrical puff-gas plasma onto a central core can result in the radiative loss of a substantial fraction of the total plasma energy. The radiative emission depends strongly on the local plasma density and temperature. In addition, optical pumping and energy transport by photons of all frequencies can influence the plasma temperature and degree of ionization, and can modify the hydrodynamic evolution of the plasma. Thus, the hydrodynamic development and atomic physics of the puff gas and core plasmas, as well as the transport of radiation, must be calculated self-consistently.

Discussion of the theoretical model can be separated for convenience as follows: (a) hydrodynamics and thermal conduction (b) ionization and atomic physics and (c) radiation emission and transport.

#### a. Hydrodynamics and Thermal Conduction

The basic hydrodynamic variables of mass, momentum, and total energy are transported in one dimension using a numerical scheme with a sliding-zone version of flux-corrected transport.<sup>2</sup> A special gridding algorithm is used which moves zones in a Lagrangian fashion and adjusts the mesh in order to resolve steep gradients in the flow. The hydrodynamic equations solved are

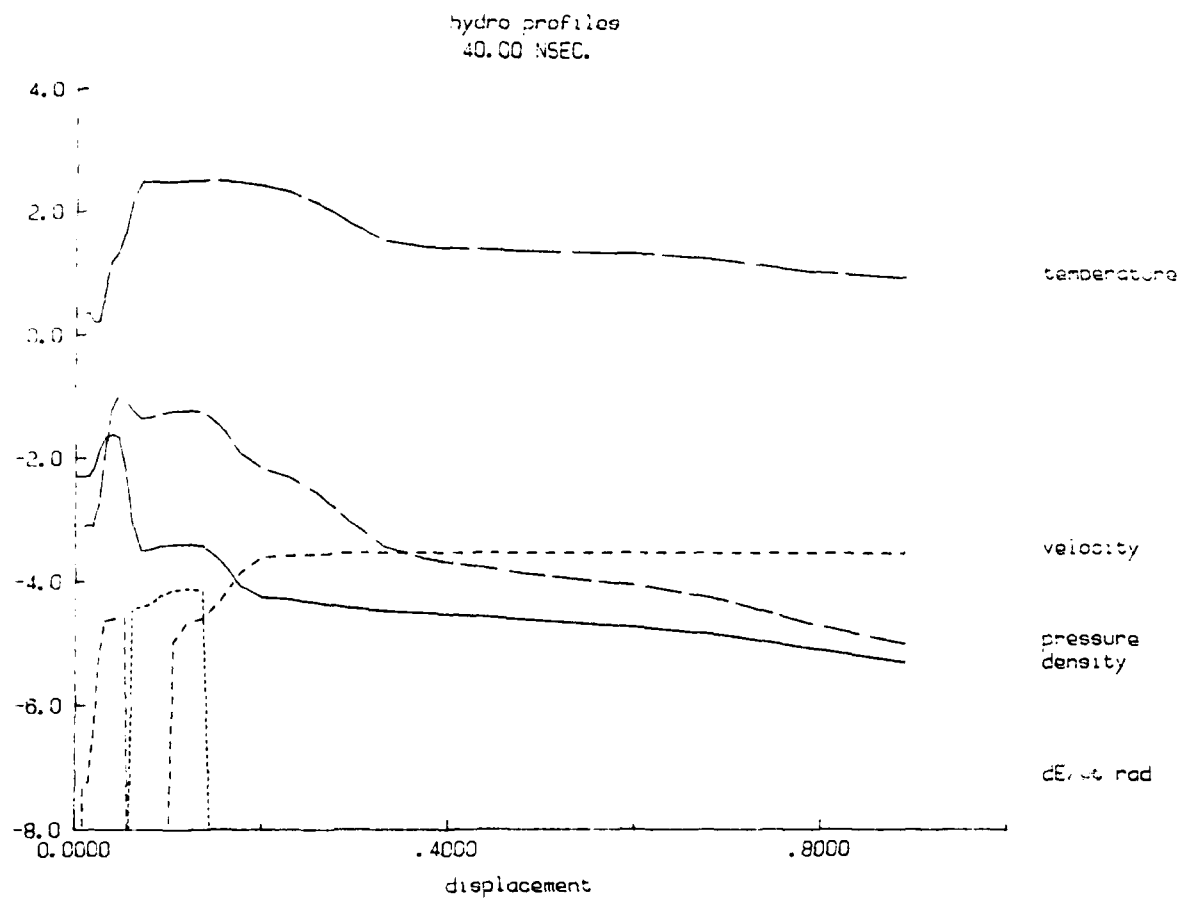


Fig. 6. Profiles at 40.0 nanoseconds. Core plasma heated by soft x-rays from interface region. Radiation energy transport evident in puff-gas out to about 0.6 cm.

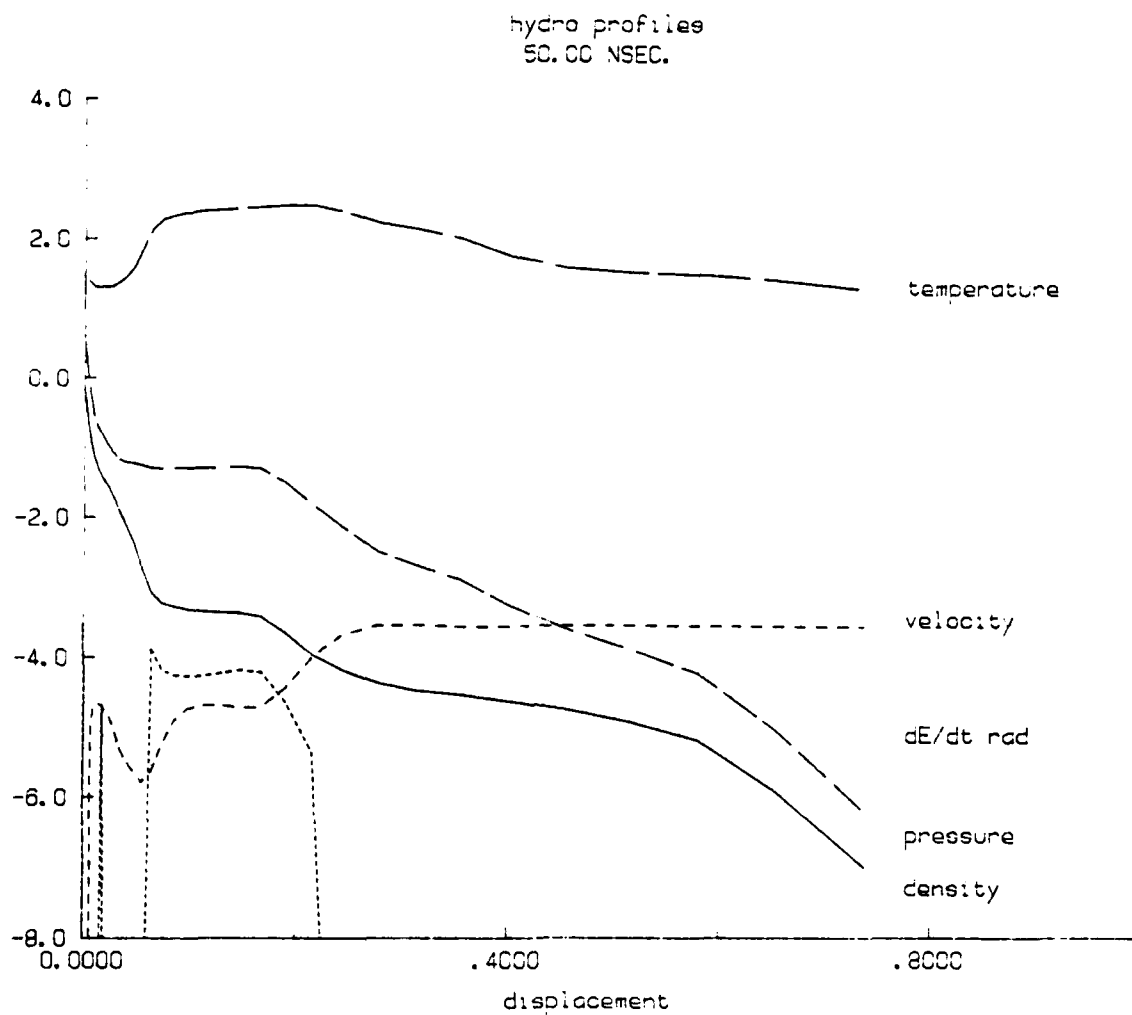


Fig. 7. Profiles at 50.0 nanoseconds. Assembly phase: inward propagating shock arrives at axis; peak density approaches solid density.

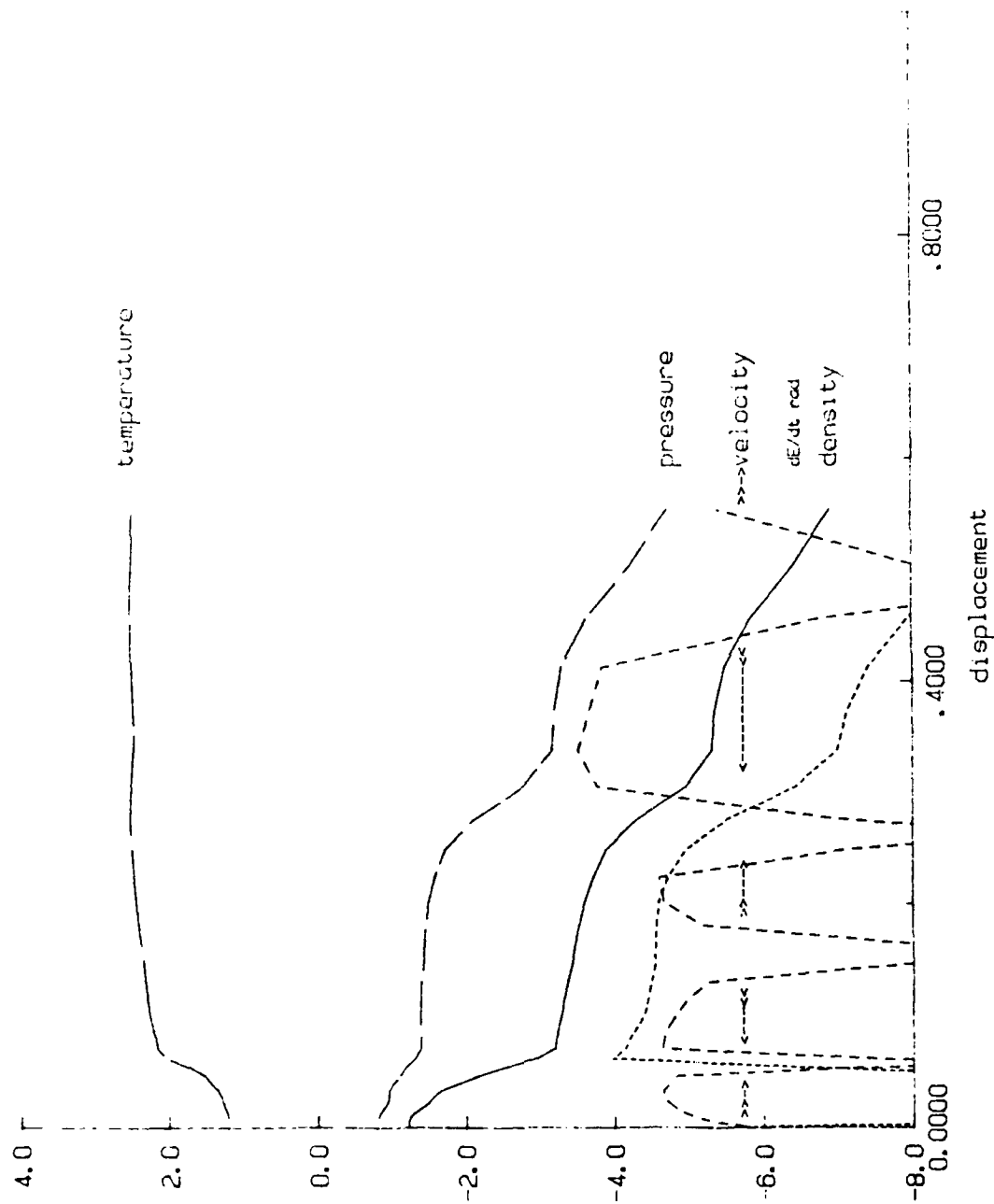


Fig. 8. Profiles at 60.0 nanoseconds. Central core and portions of puff-gas plasmas moving radially outward. Global kinetic energy near minimum value.

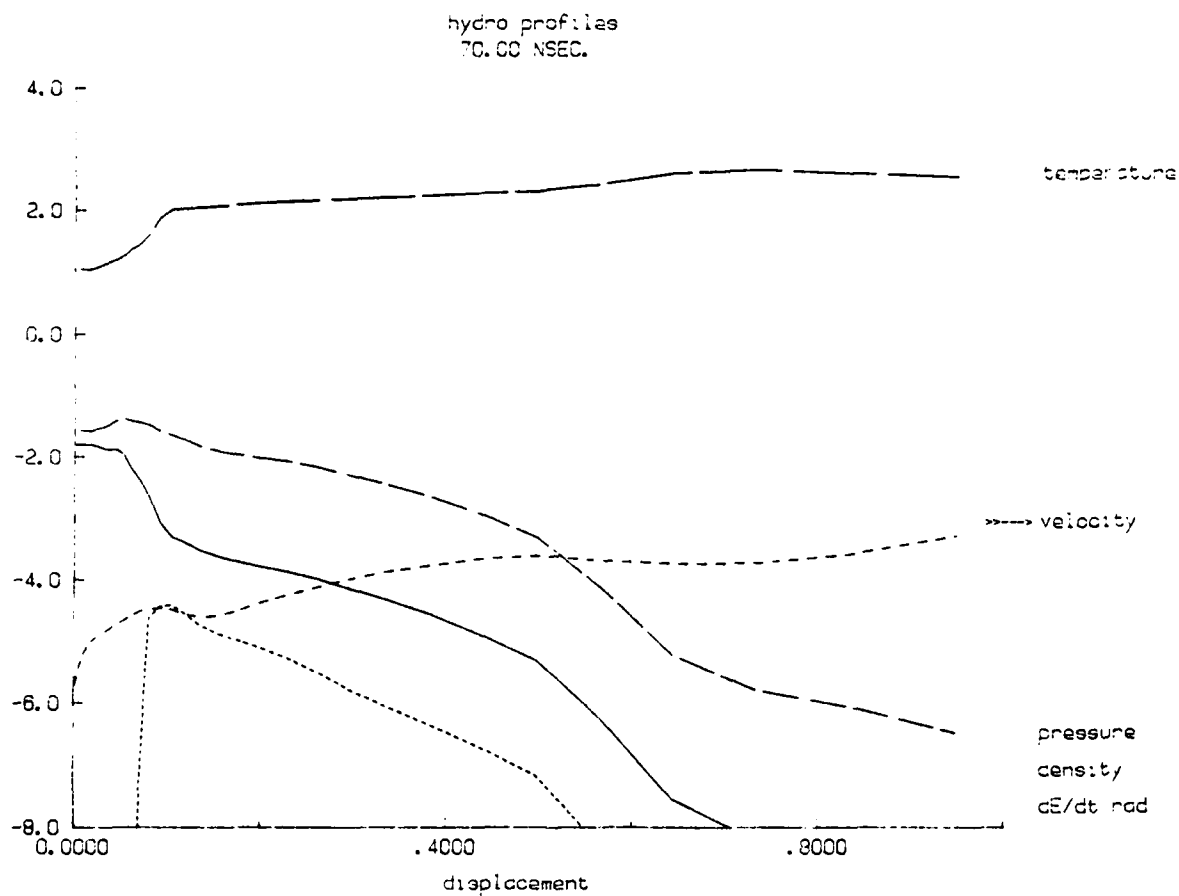


Fig. 9. Profiles at 70.0 nanoseconds. Expansion phase: entire plasma moving radially outward. Core plasma remains relatively cool.



# ENERGY HISTORY

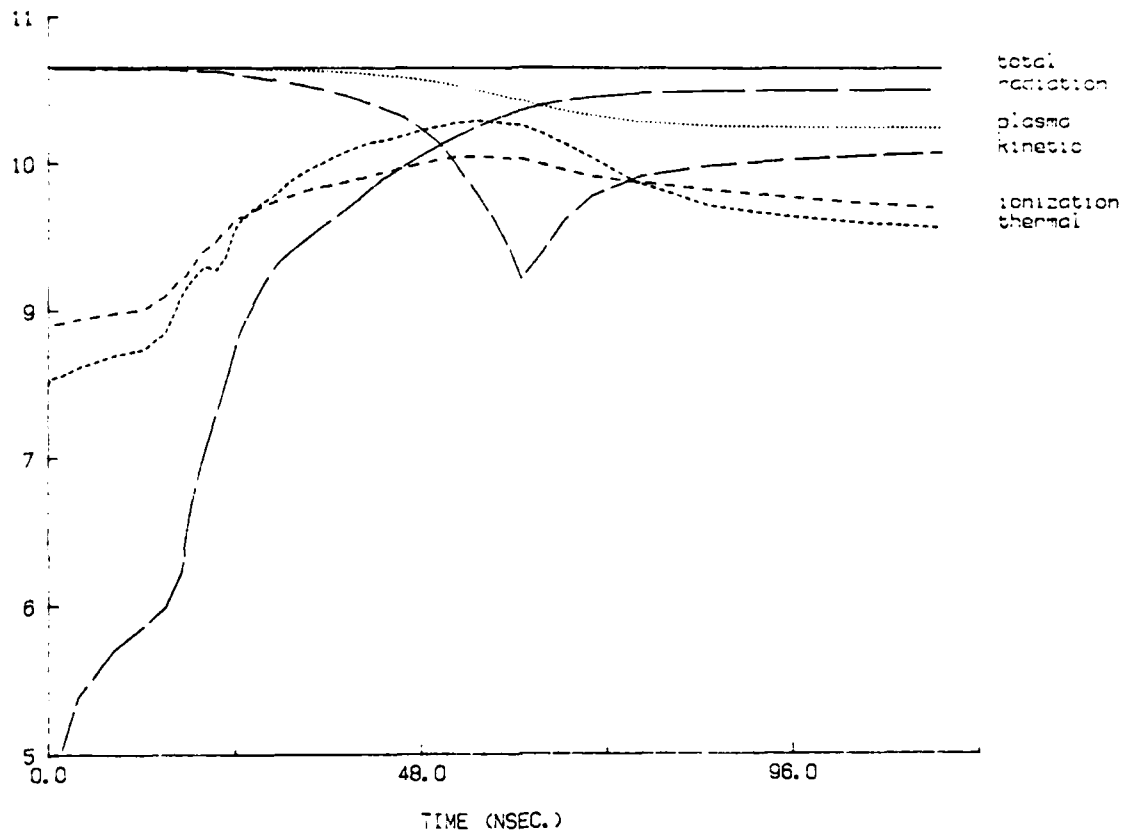


Fig. 10. Energy history of puss gas implosion on central core. For each category, the energy ( $\log_{10}$  energy in ergs) is given as a function of time.

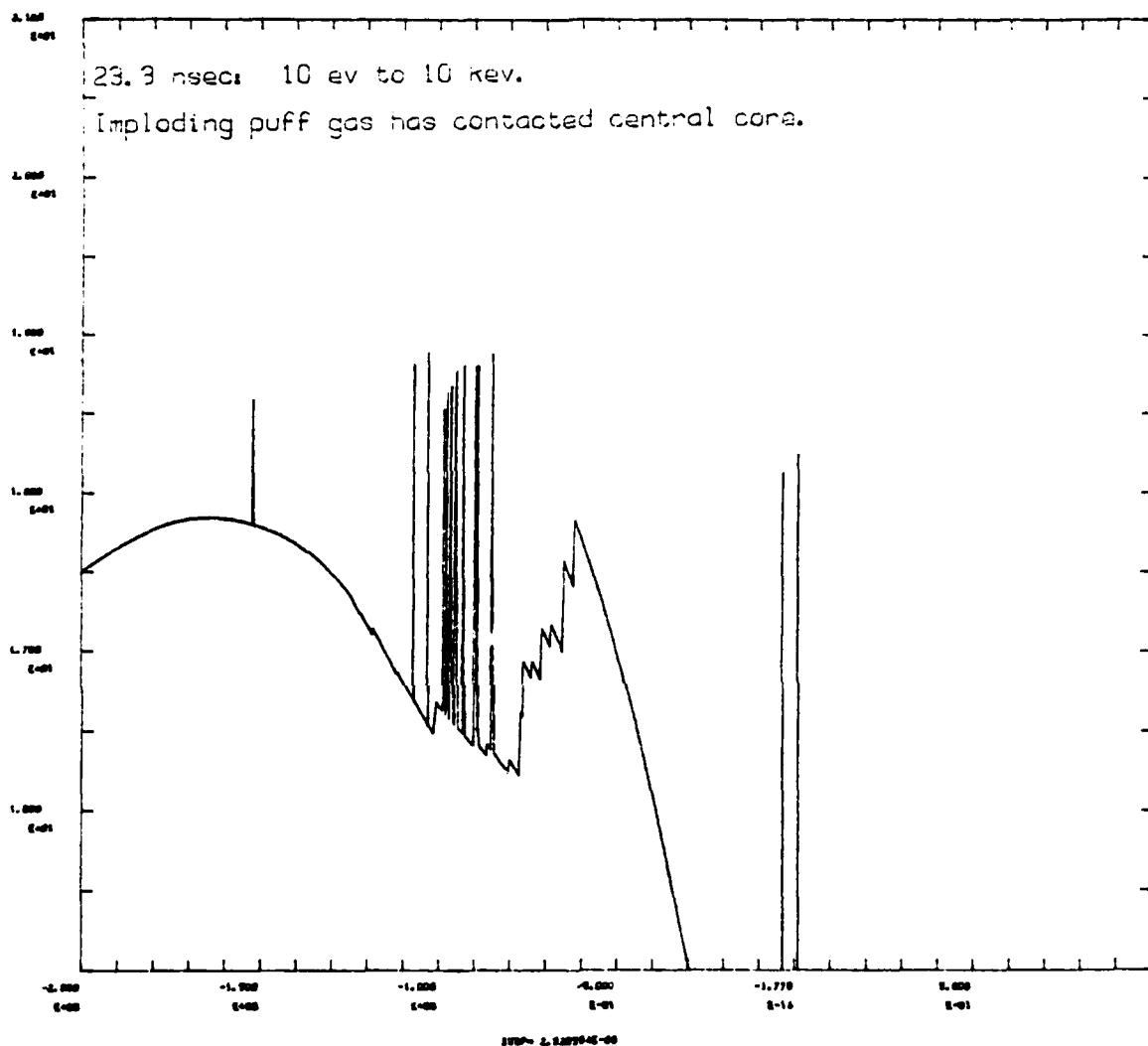


Fig. 11. Emission spectrum at 23.3 nanoseconds. Spectral intensity (from  $10^{15}$  to  $10^{21}$  ergs/sec-cm-keV) is plotted as a function of photon energy (from 10 eV to 10 keV). At this time, L-shell emission dominates.

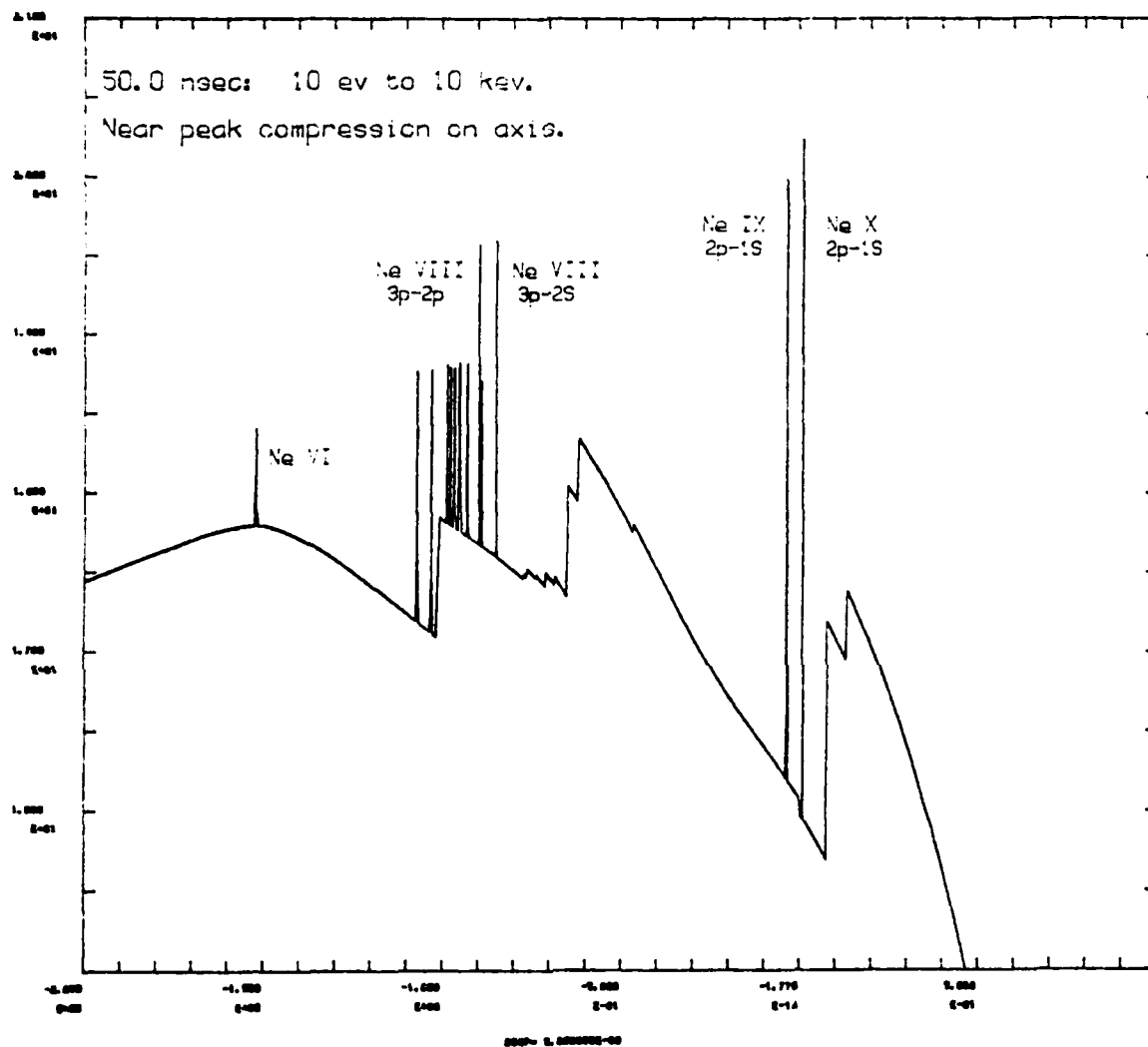


Fig. 12. Emission spectrum at 50.0 nanoseconds. K-shell radiation dominates with most of the power in the indicated H and He-like emission lines.

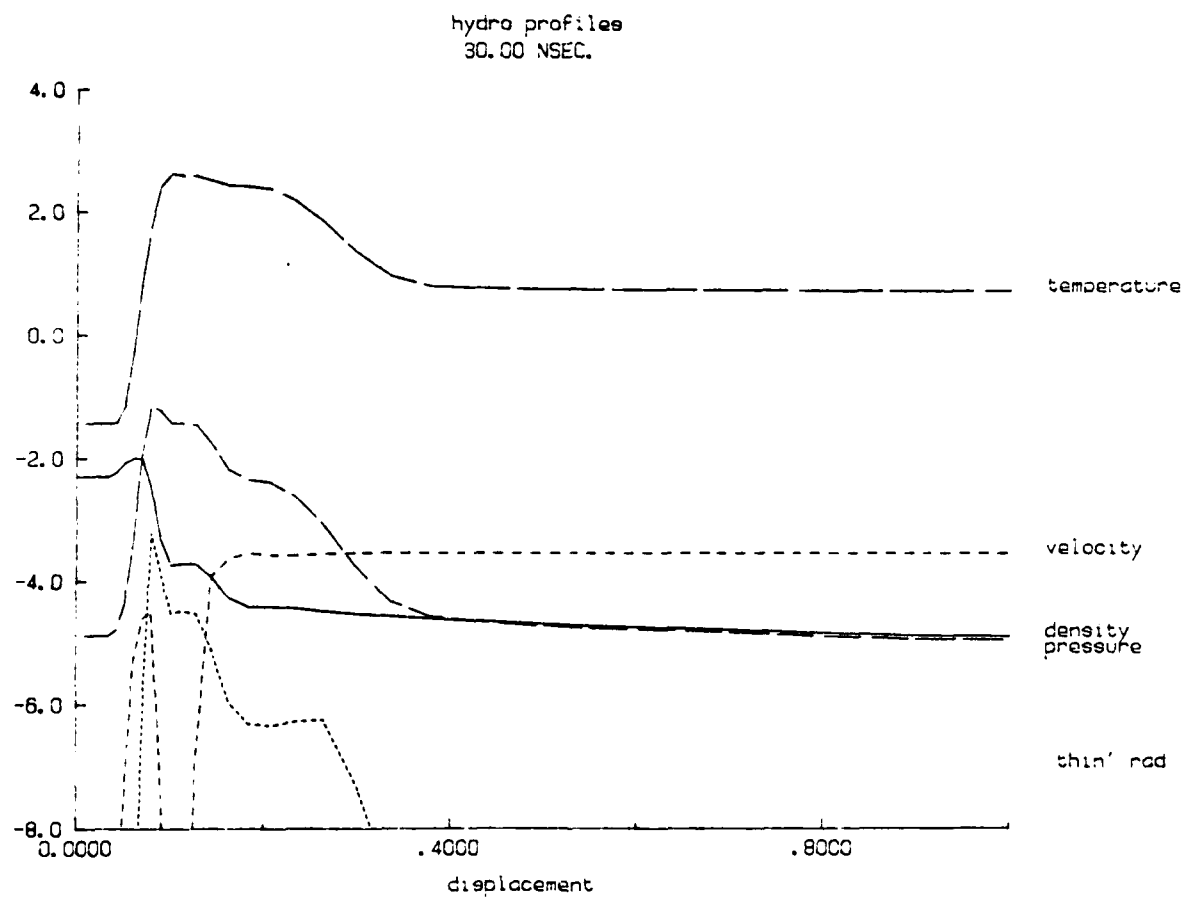


Fig. 13. Profiles at 30.0 nanoseconds neglecting effects of radiation. The core plasma remains very cold, and there is no evidence of heating deep in the puff-gas.

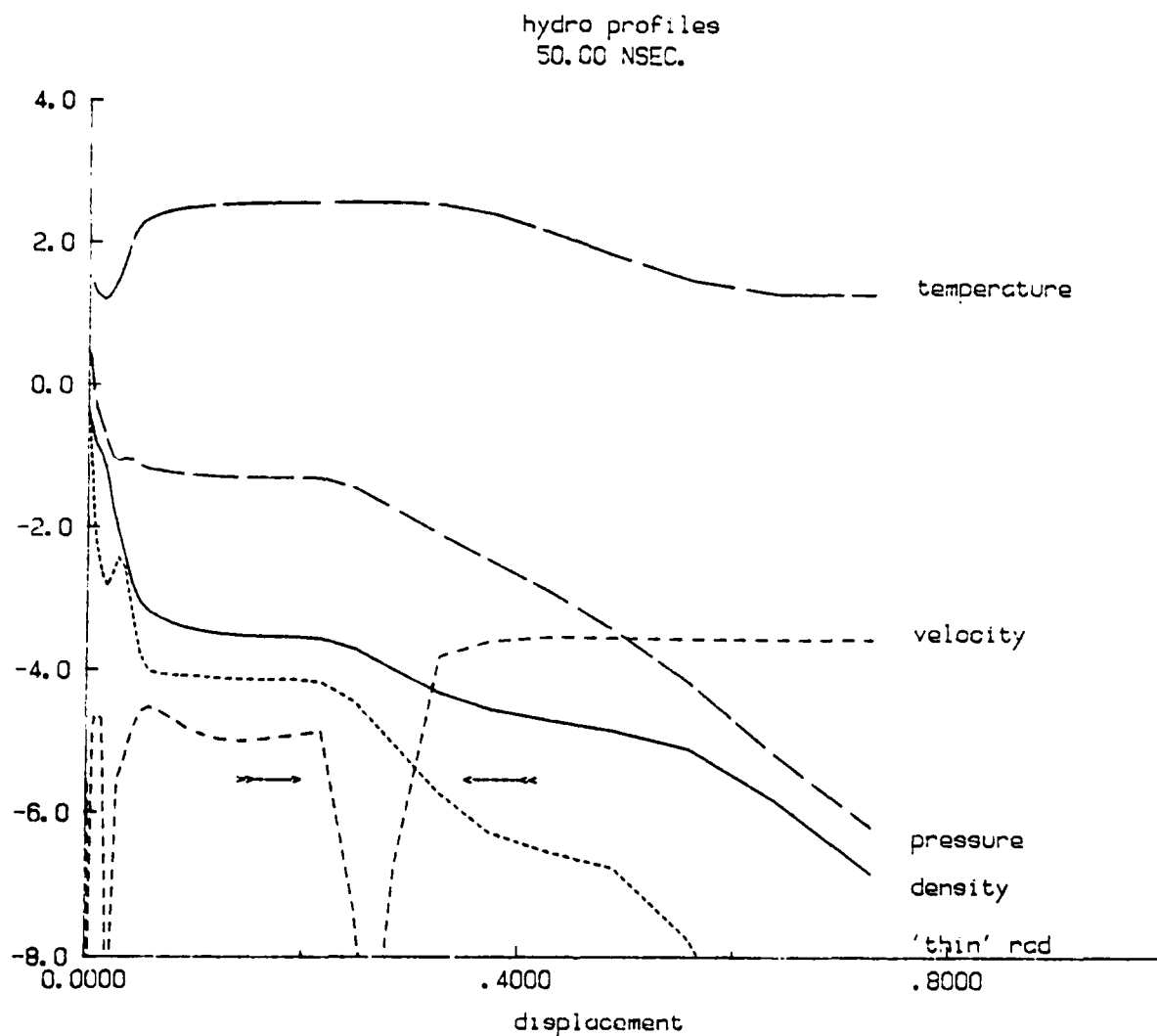


Fig. 14. Profiles at 50.0 nanoseconds neglecting effects of radiation. Assembly on axis occurs at about the same time, but there are substantial differences in the plasma density and temperature profiles.

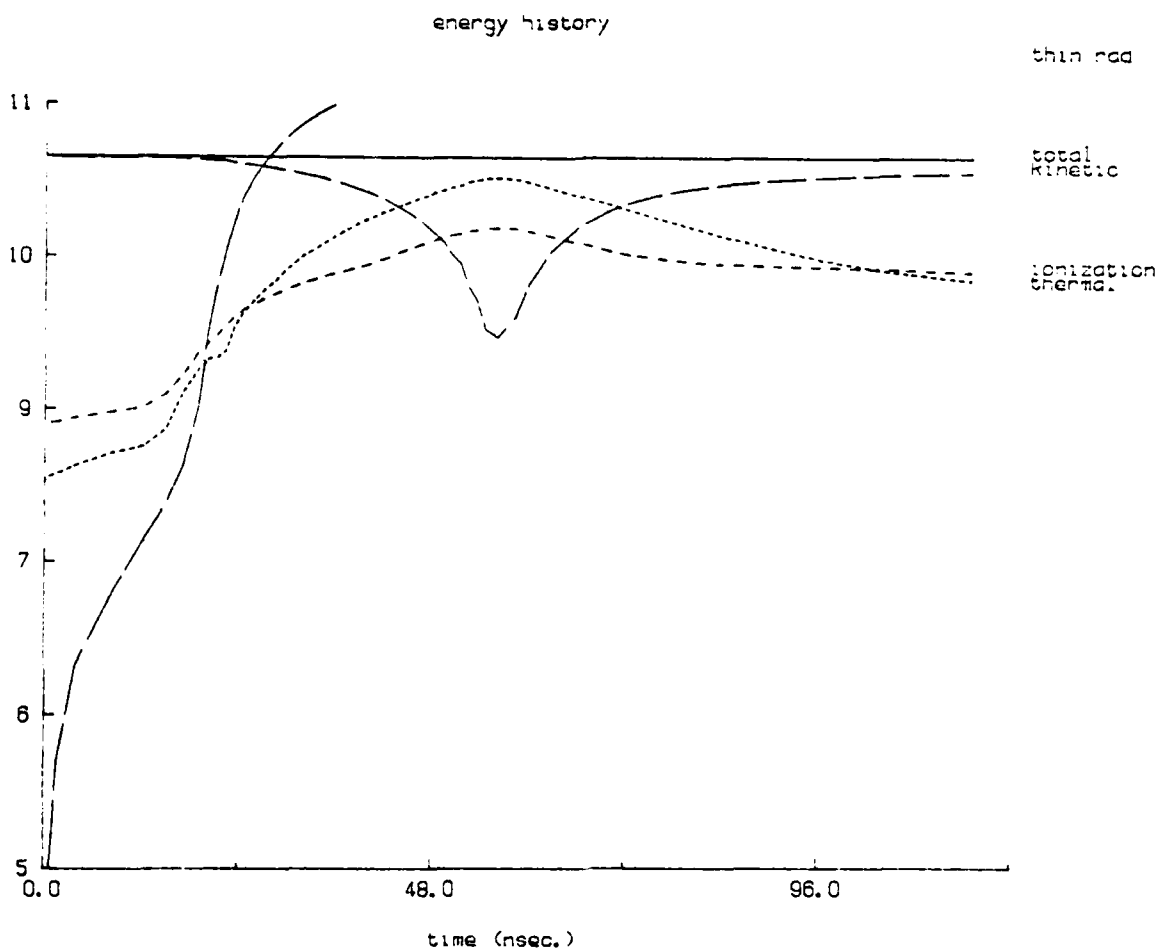


Fig. 15. Energy history of puff gas implosion neglecting effects of radiation. Optically thin radiation is calculated but it does not remove energy from the plasma.

### References

1. R. Spielman and M.A. Palmer, Bull. Amer. Phys. Soc. 24, 1361 (1984).
2. J. P. Boris and D. Book, J. Comput. Phys. 11, 38 (1973).
3. D. Duston and J. Davis, Phys. Rev. A 23, 2602 (1981).
4. D. R. Bates, A. E. Kinston, and R. W. P. McWhirter, Proc. R. Soc. London, Ser. A 267, 297 (1962).
5. A. Burgess, in Proceedings of the Symposium on Atomic Collision Processes in Plasmas, Culham, England, Report No. 4813, 63, 1964 (unpublished); and A. Burgess, H. P. Summers, D. M. Cochrane, and R. W. P. McWhirter, Mon. Not. R. Astron. Soc. 179, 275 (1977).
6. V. L. Jacobs, J. Davis, P. C. Kepple, and M. Blaha, Astrophys. J. 211, 605 (1977).
7. W. J. Karzas and B. Latter, Astrophys. J. Suppl. Ser. 6, 167 (1961).
8. V. L. Jacobs and J. Davis, Phys. Rev. A 18, 697 (1978).
9. J. Davis, P. C. Kepple, and M. Blaha, J. Quant. Spectrosc. Rad. Transfer 16, 1043 (1977).
10. E. Oran and J. Davis, J. Appl. Phys. 45, 2480 (1974).
11. J. R. Apruzese, J. Davis, D. Duston and R. W. Clark, Phys. Rev. A 29, 246 (1984).
12. J. P. Apruzese, J. Davis, D. Duston, and K. G. Whitney, J. Quant. Spectrosc. Rad. Transfer 23, 479 (1980).
13. J. P. Apruzese, P. C. Kepple, K. G. Whitney, J. Davis and D. Duston, Phys. Rev. A 24, 1001 (1981).
14. Frank Biggs and Ruth Lighthill, Sandia Laboratories Report No. SC-RR-71 0507, 1971 (unpublished).
15. E. Clementi and C. Roetti, At. Data Nucl. Data Tables 14, 177 (1974).

## E. Velocity Scaling of the Radiatively Dominated Z-Pinch

### I. THE ELECTRODIFFUSIVE MODEL

For a simple diode the general formulation of a fast Z-pinch implosion model<sup>1</sup> can be schematically represented as shown in Fig. 1. The input current waveform at some radius and the initial plasma load conditions, in any of several possible representations, provide a unique initial value problem. The complete electromagnetic calculation being quite difficult, a common approximation is that of neglecting all displacement currents and the details of capacitive energy storage.

#### a. Diffusive Approximation

If one gives up some information concerning the details of the diode fields and makes the assumption that the incoming and outgoing wave components are in detailed balance, then the Hertz wave equation (for  $Z(r,t)$ ) can be transformed to a diffusion equation<sup>2</sup>

$$\frac{D}{D\tau} E = \{u^{-1} \partial_u u \partial_u E\} \frac{1}{4\pi\hat{\Sigma}} - \hat{E} \partial_\tau \ln \Sigma - \partial_\tau E_{th} - B \partial_\tau \beta, \quad (1)$$

where  $E_{th}$  is the thermoelectric field,  $\Sigma$  is a dimensionless conductivity,  $\beta = v_{fluid}/c$ ,  $E' = E + \beta B$ ,  $\hat{E} = E + \beta B + E_{th}$ ,  $D/D\tau = \partial_\tau + \beta \partial_u$ , and  $u = r/r_0$ ,  $\tau = t/t_0$ ,  $t_0 = ct_0$ . The fluid response to the electromagnetic stresses and heating is embodied in the relations

$$\frac{D}{Dt} v_r = - \frac{\tilde{T}}{\tilde{m}} \partial_r \ln n_I - \frac{\partial_r \tilde{T}}{\tilde{m}} - \frac{J_z B_\theta}{\tilde{m} c n_I} + \frac{\rho \Sigma_r}{\tilde{m} n_I}, \quad (2)$$

$$\frac{D}{Dt} \theta_e = - \frac{2}{3} T_e (\nabla \cdot \nabla) + \{ (\nabla \cdot (x_e \partial_\tau T_e)) + \nabla \cdot (\beta_\Lambda^T u_z) \} \left( \frac{3}{2} z n_I \right)^{-1}$$



$$+ \frac{2}{3zn_I} (J_z \cdot E'_z) + \frac{2m_e}{m_I} \left( \frac{T_I - T_e}{T_e} \right) + Q_{\text{Rad}}, \quad (3a)$$

$$\begin{aligned} \frac{D}{Dt} T_I = & -\frac{2}{3} T_I (\nabla \cdot \mathbf{V}) + \left( \frac{3}{2} n_I \right)^{-1} \nabla \cdot (\chi_I \partial_r T_I) \\ & + \frac{2zm_e}{m_I} \left( \frac{T_e - T_I}{\tau_e} \right). \end{aligned} \quad (3b)$$

In these expressions  $\theta_e T_e + (2/3)\epsilon_I/z$ ,  $\tilde{T} = T_I + zT_e$ ,  $\tilde{m} = M_I + z_{\text{max}}m_e$ ;  $\chi_e, I$  is the thermal conductivity.  $\tau_e$  the plasma relaxation time,  $E_r$  the ambipolar radial field (with  $\rho$  its induced charge density), and  $Q_{\text{rad}}$  is the net (local) radiative heating or cooling. The radial electric field is established as a solution to an integral equation derived from the radial component of Ohm's law. Any drift speed limitation on current is supplemented by a (nonlinear) change in  $\Sigma$  where the local  $E$  field requires it.

#### b. Discrete Realization

Notation: The (nonuniform) time levels for any variable are indexed with a leading superscript; the Lagrangian fluid mesh is denoted by  $r$ , and its material derivatives by a superscripted dot (or dots). Spatial indexing is denoted by trailing subscript.

Method: The base representation for all the hydrodynamic variables is the set  $\{ {}^i_c N_j, {}^i_c T_{Ij}, {}^i_c \theta_{ej}, {}^i_r \}$  and  $\{ {}^i_c E_{z,j} \}$ , the diffusing electric field. The relationships among the basic fluid variables on the Lagrangian mesh are illustrated in Fig. 2. The numbers of cell ions  $\{ {}^i_c N_j \}$  are a conserved vector of ions/cm resident in the (compressible) cell and assigned spatial locations given by the cell center position, the equal area point.

In general, at any subcycle point  $t^*$  within  $({}^i t, {}^{i+1} t)$ , one must map  $\{ t^*, {}^*c T_{Ij}, {}^*c E_{zj}, {}^*c \theta_{ej} \} \rightarrow \{ {}^*c \dot{T}_{Ij}, {}^*c \dot{E}_{zj}, {}^*c \dot{\theta}_{ej} \}$  in such a way that the intermediate fields  $\{ {}^*r_j, {}^*v_{rj}, {}^*c \theta_{jk}, {}^*J_{zj} \}$  are all consistent with one another. Only the time can enter as a generator of  ${}^*r_j$  and  ${}^*v_{rj}$ , because

of the Lagrangian nature of the mesh.

Although the  $^*V_{rj}$  and  $^*B_{\theta j}$  calculations must be considered coupled problems, a magnetic field calculation from any given velocity profile is the pivotal element in achieving the desired self-consistency.

If the mesh and its velocity are presumed given, or at least provisionally established subject to iterative refinement, then there is just one current density profile

$$J_z = J_z(T_e, n_e, B_\theta) \left( E_z + \delta_r B_\theta + \left( \frac{1}{e} \partial_r T_e \right) \chi \frac{B_0'' + B_1'' \chi^2}{\delta_0 + \delta_1 \chi^2 + \chi^4} \right) \quad (4)$$

with  $B_\theta = (2/or) \int_0^r (2\pi r_1 J_z) dr_1$ , and  $\chi = - (1.7588 \cdot 10^7 r_e) B_\theta$ , a nonlinear integral equation, using Braginskii's functions  $\delta, \delta$ . This information is sufficient to define a derivative function,  $\dot{Y}_j = \dot{Y}_j(Y_k, t^*)$  with  $Y_k = \{^*T_{Ik}, ^*E_{zk}, ^*\theta_{ek}\}$  and the Jacobian is either lower Hessenberg (no photons) or a full matrix (with radiation transport).

The mesh  $r_j, \dot{r}_j$  and  $Y_j$  are then integrated by a fully implicit NML technique<sup>3</sup>, using an estimated integrating factor to track the "stiff" elements of the set. Each location  $Y_j$  thus obtains a local filter for integration which, for a 2nd order method, is

$$^*Y_j = \frac{\epsilon h B_{-1}(\epsilon) ^*\dot{Y}_j}{1 + f_j h \epsilon B_{-1}(\epsilon)} + \frac{I_j(^k Y_j, ^{k-1} Y_j, ^k \dot{Y}_j, ^{k-1} \dot{Y}_j; \epsilon, f_j)}{1 + f_j h \epsilon B_{-1}(\epsilon)}$$

$$I_j = A_0(\epsilon) e^{\epsilon h f_j ^k Y_j} + A_1(\epsilon) e^{(1+\epsilon) f_j h ^{k-1} Y_j} +$$

$$n[B_0(\epsilon) e^{\epsilon h f_j ^k (\dot{Y}_j - f_j Y_j)} + B_1(\epsilon) e^{(1+\epsilon) f_j h ^{k-1} (\dot{Y}_j - f_j Y_j)}]$$

where  $\epsilon = (t^* - ^k t)/h$ ;  $h = ^k t - ^{k-1} t$  and the coefficients  $[B_{-1}, B_0, B_1, A_0, A_1]$  prescribe the bare variable step filter which acts when  $f_j \rightarrow 0$ . Here  $f \neq 0$  only if

AD-A157 535

ADVANCED CONCEPTS THEORY ANNUAL REPORT 1984(U) NAVAL  
RESEARCH LAB WASHINGTON DC 26 JUN 85 NRL-MR-5598

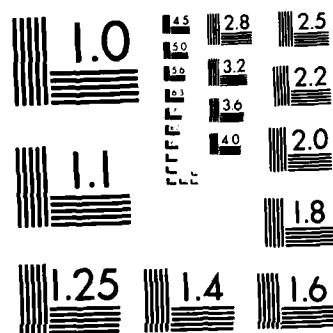
2/2

UNCLASSIFIED

F/G 28/9

NL

									END				
									FILED				
									DEC				



MICROCOPY RESOLUTION TEST CHART  
NBS 1963-A

$$\left| f_j \doteq \frac{1}{2} \left( \frac{k_{Yj}^{\dot{Y}}}{k_{Yj}} + \frac{k_{Yj}^{k-1 \dot{Y}}}{k_{Yj}^{k-1}} \right) \right| > f_{\min} \quad \text{and,}$$

$$\left( \frac{k_{Yj}^{\dot{Y}}}{k_{Yj}} \right) \left( \frac{k_{Yj}^{k-1 \dot{Y}}}{k_{Yj}^{k-1}} \right) > 0.$$

#### b. Limitations and Remedies

Once the displacement current has been neglected one must also approximate in some way the source of field momentum ( $g_r = \frac{1}{c} S_r$ ) and the proper formulation is that of a flux limit. This flux limit takes the form of a filter derived from the detailed balance of field and fluid momentum

$$\int_{r<}^{r>} d^3r [\partial_t g_r + \partial_t P_r] = \int_{r<}^{r>} dr [r^{-1} \partial_r (\rho r v_r^2) +$$

$$r^{-1} \partial_r (r p^* - r p)^* + B^2/4\pi r] = 0$$

which implies a bound on  $\int dr (\partial_t g)$  over each resolution domain for  $\int dr (\partial_t P)$  as determined by the artificial viscosity model. The result is a generalized Rankine-Hugoniot jump condition

$$v_{>} - v_{<} = \frac{r_{<} p_{<}^* - r_{>} p_{>}^*}{|r_c \rho_c v_c|} - (r_c \rho_c v_c)^{-1} \int_{r<}^{r>} dr \left( \frac{B^2 - E^2}{8\pi} - n_{\text{ion}} \tilde{T} \right),$$

$p^* = E^2 + B^2 + n_{\text{ion}} \tilde{T}$  (total pressure).  $\tilde{T} = zT_e + T_{\text{ion}}$  (effective fluid temperature).  $p_c = M_{\text{ion}}$  (density at cell center). The flux limit arises as a bound on the spatial gradient of  $\beta$  admitted in the E field source

term  $B\partial_t\beta$ , i.e.

$$|\partial_u\beta| < \left| \frac{\tau_o(V_J + 5 - V_J)}{5c(r_J + 5) - \tau_J} \right|$$

The limit prevents unstable growth of  $E_z$  on the outer surface of the model plasma due to underresolved flow gradients.

A second and more fundamental limitation arises due to acausal propagation of magnetic disturbances. This may obtain, for example, when an interior zone increases its conductivity, due to compression or Ohmic heating, and draws more current. The added current will produce an immediate rise in strength of  $B$  in all exterior zones, but the resulting change in the (magnetically insulating)  $\beta_r B_\theta$  component of the total  $E'$  field is not a diffusive source of  $E$  in those exterior domains. When this source does not act the flow appears "over-insulated", the total  $E'$  field (in the plasma frame) reverses and so must  $J$  in the exterior domains. In a proper electromagnetic calculation this source would be reflected in  $\partial_t J$ , the  $E$  field would propagate inward rapidly and cancel the change in the  $\beta B$ . The current reversal would not be as likely to occur. For fixed  $\partial_t J$  the wave equation source term produces a first integral

$$\partial_t E = - \partial_t J \cdot \tau_{rev} \cdot 4 \pi .$$

While this source and its first integral are unavailable to the diffusive theory, an explicit source for  $E$  is added which turns on when a reversal of  $J$  occurs and seeks to drive the lab frame  $E$  in a direction that will quench the reversal. In the above relation the integration interval  $\tau_{rev}$  forms a natural free parameter with which to calibrate the "battery" source term to a time scale below that typical of magnetosonic wave transit and limit the resulting stiffness to acceptable levels.

A third practical limitation to the model is the difficulty in obtaining current and voltage measurements (at the outer radius) which are well synchronized and comparably accurate. If the experimental voltage and current traces have any relative phase error, the subtraction of these waveforms to produce a plasma voltage is subject to excessive noise and

tends to produce rather wild boundary conditions for the model.

The most effective remedy to date is to insist on continuity in the waveguide impedance at the plasma boundary and let

$$E_p = c E_j (I_{gen}/I_p),$$

where

$E_p$  = ghost point boundary value,

$I_p$  = axial current flowing in the plasma,

$I_{gen}$  = known current waveform near the load,

$c E_j = E_z$  value at the outermost cell center.

## II. VELOCITY SCALING BEHAVIOR

### a. A simple diagnostic

The study consists of driving a constant initial configuration with a current pulse

$$I_{gen}(t) = f I_0 \frac{1}{2} \left( 1 + \tanh \frac{(t-t_0)}{t_s} \right); \quad (5)$$

for a load mass (in Neon) of 63  $\mu\text{g}/\text{cm}$ , a peak initial density at 1.25 cm, and a current  $I_0$  typical of Gamble II currents, the load implodes in about 125 ns. The value of "f" defines the scale parameter.

In order to compare the 1-D calculation with the 0-D snowplow model<sup>4</sup>, one may mass average the velocity and electric fields as

$$V_{load} = \left( \sum_i N_i c v_{ri}^2 / \sum_i N_i \right)^{1/2} \quad (6a)$$

$$\bar{E}_z = \left( \sum_i N_i c E_{zi} \right) / \sum_i N_i \quad (6b)$$

and from  $\bar{E}_z$  develop the expected scale velocity arising from the snowplow model

$$V_{\text{snowplow}} = [c^{1/2} / (4 \pi \rho_0)^{1/4}] \bar{E}_Z^{1/2} \quad (7)$$

where  $\rho_0$  is the initial average mass density. The ratio of these two velocities generally represents a rough comparison of the 1-D model pinch speed and that of the snowplow, and tends to peak at a time near the middle of the Z-pinch's run down.

Let

$$S(f, Q_{\text{rad}}, A) = \sup_{t \leq t_{\text{implosion}}} (V_{\text{load}} / V_{\text{snowplow}}) \quad (8)$$

and one may examine the quality of the snowplow model as a predictor of pinch speed (and available kinetic energy for later radiation).

#### b. Conclusion

As shown in Fig. 3, the snowplow scaling with  $f$ :  $0.15 < f < 1.75$  is by no means perfect. The effect of early radiation on the scaling error is most acute for the low current cases. However, the general trend is to reduce the pinch velocity and narrow the load width, as shown in the fluid trajectory comparison; Fig. 4a,b. At the higher current levels, the closing of the  $S(f)$  and  $S(f, Q_{\text{rad}} = 0)$  appears to be asymptotic, rather than showing a cross over.

A more extensive study can thus indicate the corrections needed in  $V_{\text{snowplow}}$  to use it as a guide in predicting the late time available kinetic energy resident in the load.



# RADIATION-COUPLED ELECTROMAGNETOHYDRODYNAMICS

## PLANE PARALLEL WAVEGUIDE

$$\nabla^2 z = -c^{-2} \int dr_1 r_1 \delta(r, r_1) \partial_t j_z(r_1, t)$$

$$E_z = -\nabla \nabla z$$

$$B_\theta = \nabla z \wedge z$$

$$① j_z = \sigma E' \quad E'_z = E_z + \beta_r B_\theta$$

$$② j_z = \sigma n_0 c_0$$

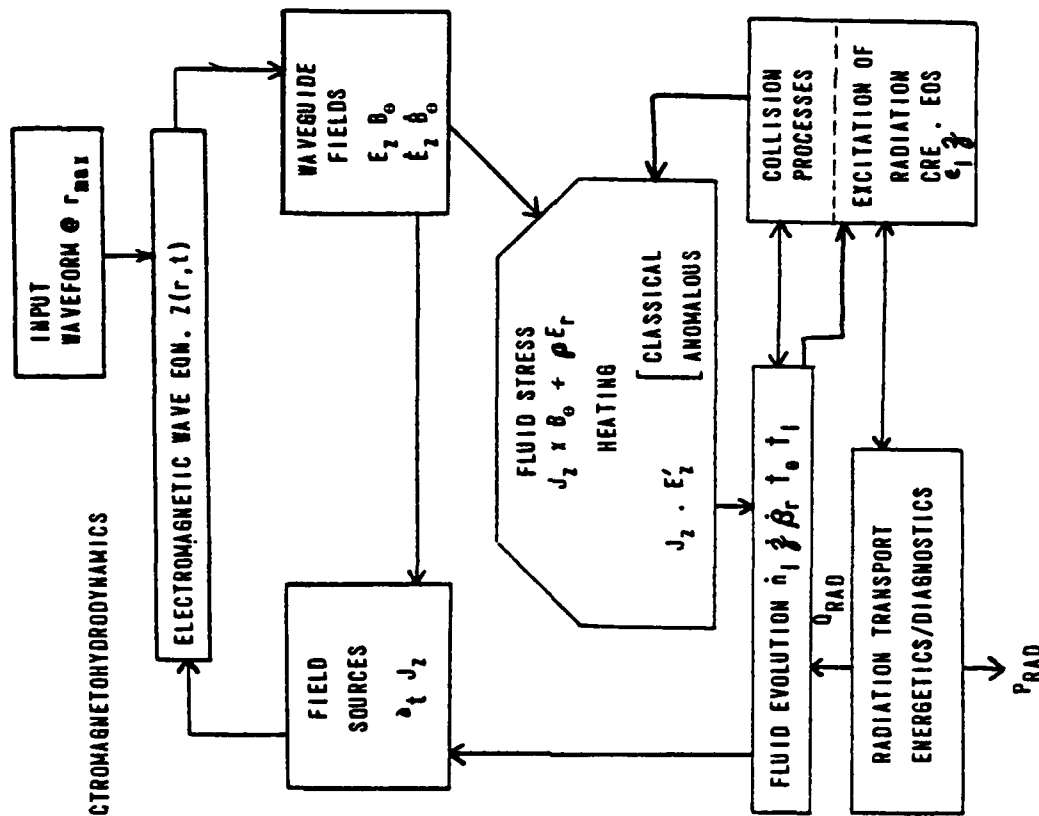
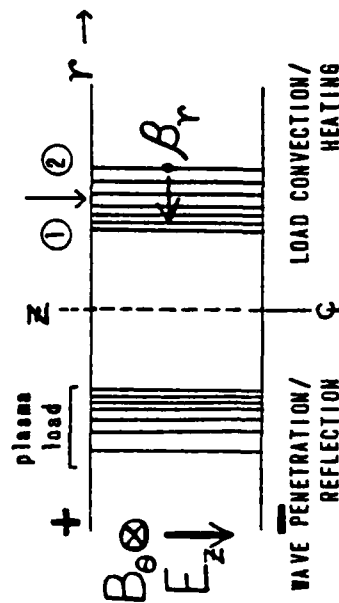


Figure 1



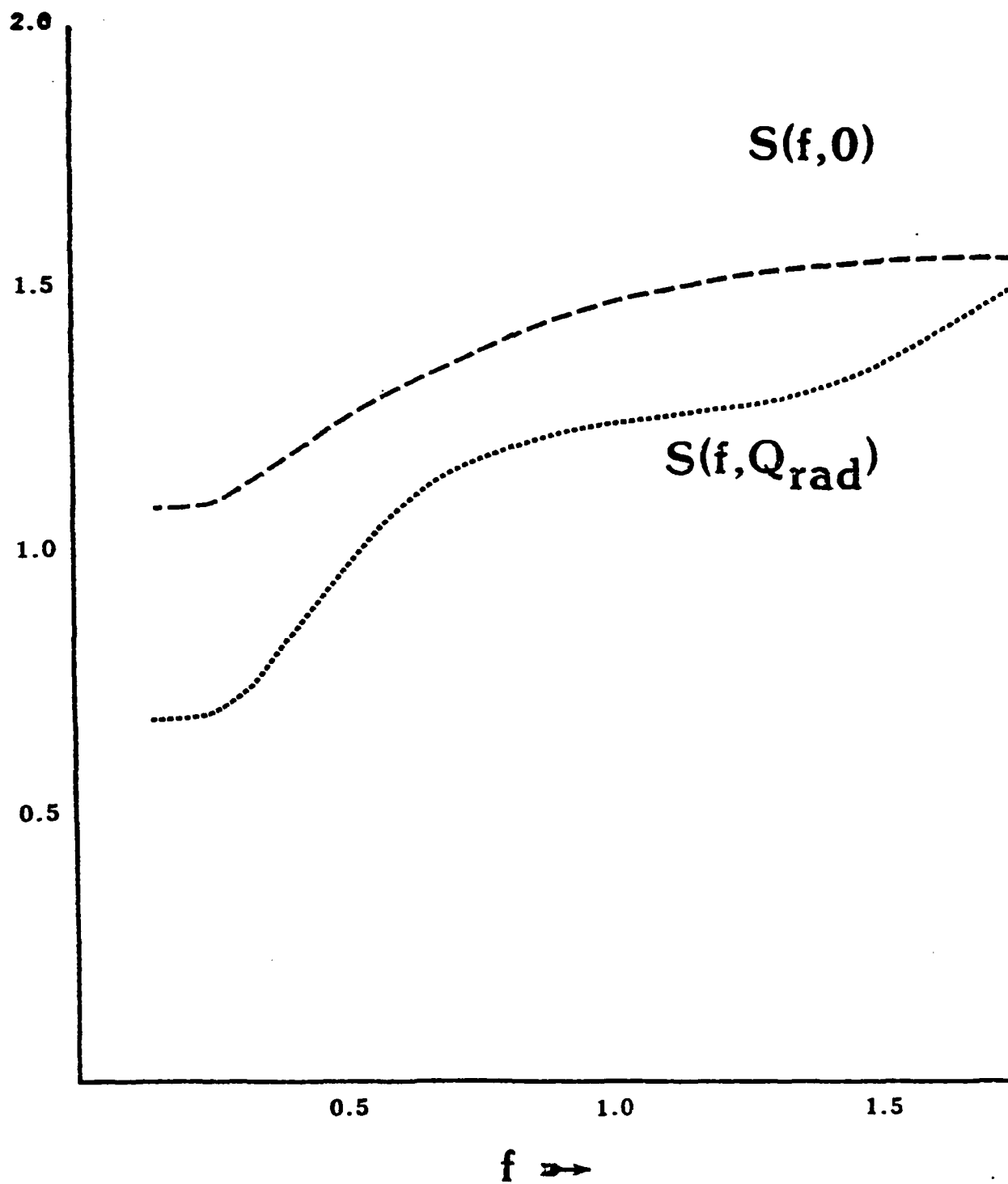


Figure 3

# Trajectories Scale 1.00

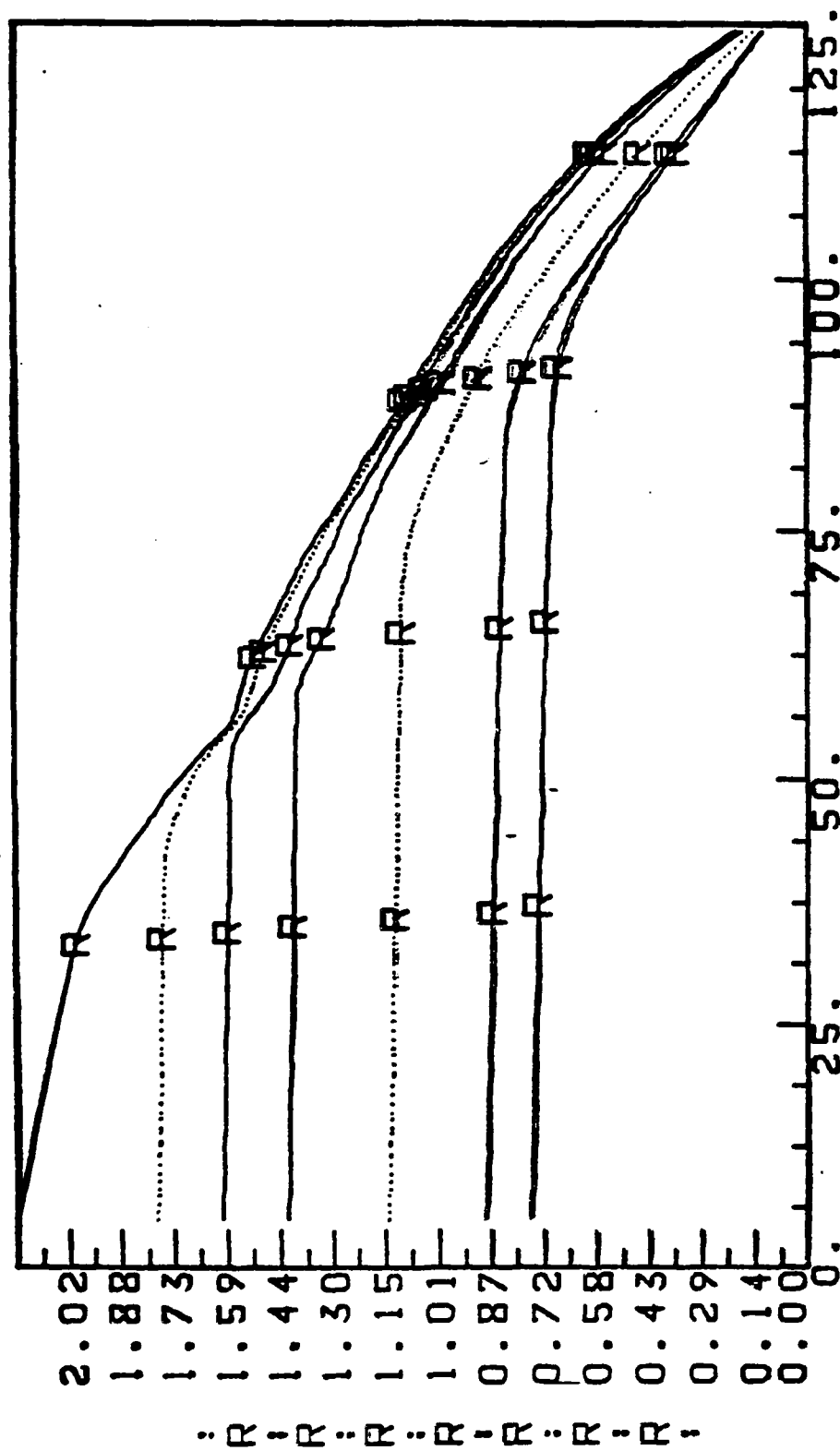


Figure 4(a)

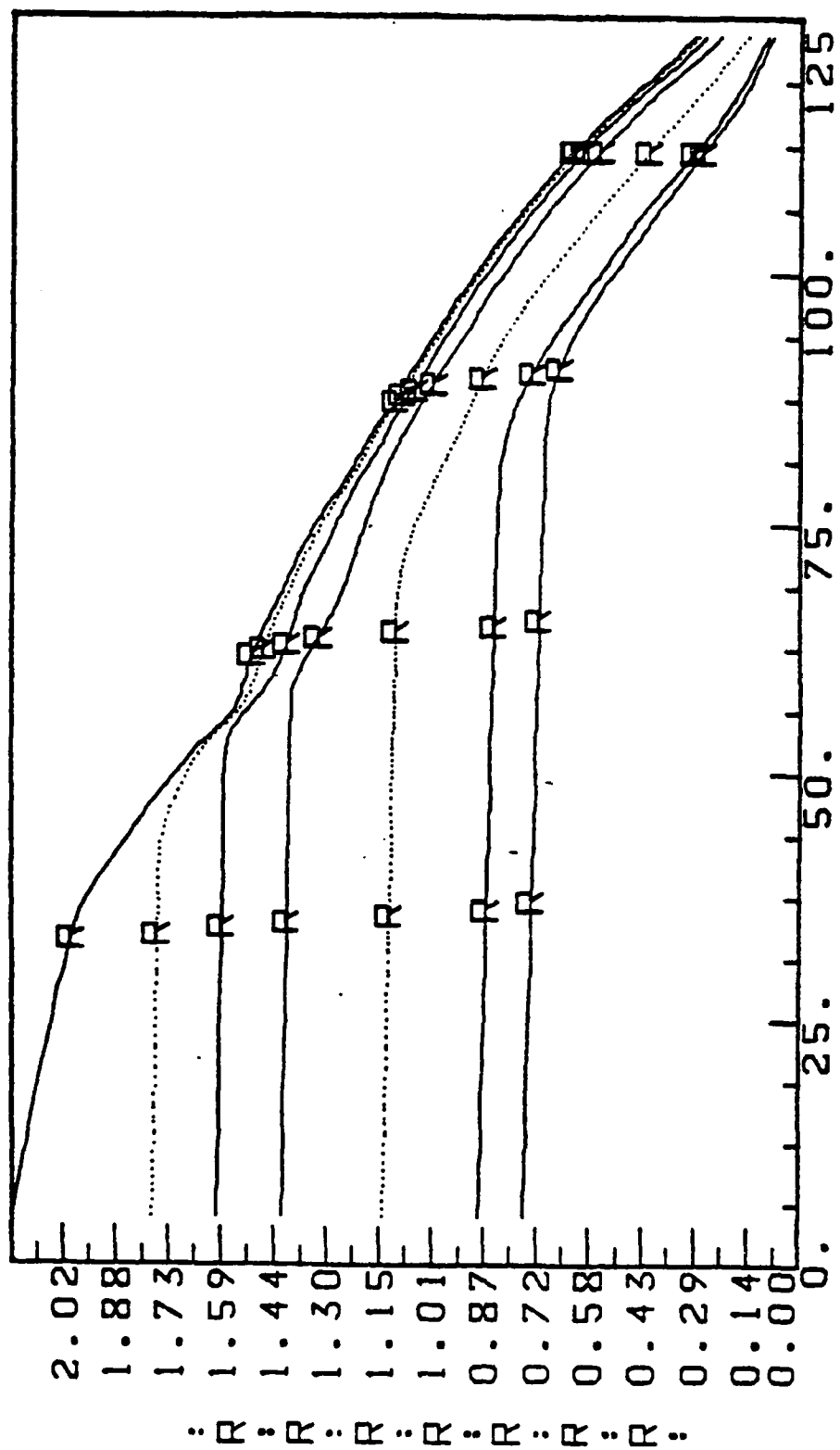


Figure 4(b)

## References

1. Generalized Hertz Vector Potential and Their Application to Diode Imploded Plasmas. R. E. Terry, J. Guillory, and D. Duston, APS - DPP 23rd Annual Meeting, October 1981.
2. Alternate Implosion Models for the Plane Parallel Diode, R. E. Terry and J. Guillory, DNA Report 6153F, April 1982.
3. Investigations of Plasma Loaded Diodes and Imploding Plasma Radiation Sources, S. A. Goldstein, et.al., JAYCOR Report J206-84-006/6231, April 1984.
4. Classical Electrodynamics, J. D. Jackson, Wiley, New York (1962). p. 322 ff.

## F. Ion-beam deposition, heating, and radiation from an aluminum plasma

### I. INTRODUCTION

Recent advances in pulsed power and diode technologies have made it possible to deliver intense proton beams onto a planar target with high efficiency. Thus, the interaction of energetic charged particle beams with materials of different composition, density, temperature, ionization state, etc., has become an active field of research (for example, see citations 1-16 and their included references). One significant application of this research is the use of ion beams to generate x-rays for materials research; other applications include ion implantation studies and ICF investigations.

Many studies of intense ion beam-materials interactions have introduced a variety of assumptions and approximations to characterize the atomic physics, ionization dynamics, absorption/emission physics, and radiative transfer. For example, Saha equilibrium is often invoked, and radiation transport is treated via a photon diffusion approximation with use of Planck (black-body) radiation distributions. These treatments may prevail in the cooler denser regions but not for the entire plasma. In this paper, a collisional radiative equilibrium (CRE) treatment of the ionization balance, a detailed configuration accounting (DCA) of the atomic level structure, and a radiation transport algorithm based on a combination of probabilistic and frequency-by-frequency ray tracing techniques are used. The CRE model generates Saha-Boltzmann populations in the denser, cooler regions of the plasma and reduces to the corona model in the rarefied, hotter regions. The radiation transport algorithm reproduces the results of the photon diffusion approximation in the cooler, denser plasma regimes. Thus, the approach taken in this paper is more general than those which employ the foregoing assumptions, but it reproduces their results in their regimes of validity; moreover, our approach is applicable in regimes where these assumptions cannot be used. This model has been described in detail elsewhere.<sup>17</sup> Instead of using the Bethe or LSS formalism<sup>18</sup> for calculating stopping power by the bound electrons in the material, the detailed generalized oscillator strength (GOS) stopping cross sections of McGuire, Peek, and Pitchford<sup>19</sup> for Al ions are used.

The sequence of events for charged particle beam-matter interaction involves consideration of several phenomena. First, there is the energy deposition within the slab by the beam. Then, there is the subsequent hydrodynamic response of the slab as it responds to this energy influx; a blow-off region develops on the front (beam) side of the plasma, while the back surface recoils away from the beam. As the slab plasma heats up, the plasma ions emit radiation which can affect the energy balance of the plasma. Thus at any instant in the plasma, there is the interplay of deposited beam energy, thermal conduction, hydrodynamic motion, radiation transport, plasma internal energy, magnetic fields, etc. to be taken into account.

With the exception of magnetic and electric field effects, this paper represents an attempt to treat all these effects self-consistently in a one-dimensional simulation of a proton beam incident on an initially solid density Al slab.

## II. THEORETICAL MODEL

The interaction of the ion beam with the target is strongly dependent on the local temperature and degree of ionization in the plasma. In addition, optical pumping and energy transport by photons of all frequencies can influence the plasma temperature and degree of ionization, and can modify the hydrodynamic response of the slab. Thus, the deposition of the beam, the hydrodynamic evolution and atomic physics of the plasma, as well as the transport of radiation, must be calculated self-consistently.

Discussion of the theoretical model can be separated for convenience as follows: (a) hydrodynamics and thermal conduction, (b) ionization and atomic physics, (c) radiation emission and transport, and (d) beam dynamics and energy deposition.



Qualitative comparisons of the ion beam-slab interaction with a treatment<sup>17</sup> of a laser beam-slab interaction shows that the laser produces higher temperatures and lower densities on the front (beam) side of the plasma, while the proton beam is more efficient at heating up the back side due to deeper penetration into the target.

Since these treatments of the beam-target interaction are one-dimensional, energy flow normal to the direction of the beam has been neglected; in addition, self-field effects have not been considered. These effects could alter significantly the range, the magnitude, and shapes of the plasma profiles given here. A two-dimensional radiation hydrodynamics code will be used to investigate some of these effects in a separate paper.

early times. In both cases, the dense part of the plasma at later times is heated predominantly by radiation transport rather than thermal conduction. The laser case shows much lower densities and higher temperatures on the front side of the plasma, whereas on the backside the laser case shows much higher density and lower temperatures. Also, by comparing Figs. 1,2 and 12, it can be seen that the laser beam calculation produces much sharper density and temperature gradients. These results substantiate the view that proton beams are more efficient than laser beams for heating up the interior and backside of the target; this is due to deeper penetration into the target by the ion beams.

## V. SUMMARY

The interaction of a one-MeV proton beam with an aluminum slab has been simulated using a fully self-consistent, one-dimensional, hydrodynamic-ionization-radiation transport model. Detailed calculations of the bound electron stopping power were used instead of analytic theories such as the LSS model and the Bethe equation.<sup>18</sup> The atomic populations as functions of density and temperature were obtained from a collisional-radiative-equilibrium assumption. The CRE model encompasses the Saha-Boltzmann and the corona models in that it reproduces their results in their regions of validity; however, it is more general in that it is applicable in intermediate regimes in which these models do not apply. Radiation transport was calculated using a hybrid scheme that combines a multi-frequency formalism for the continuum with a probability-of-escape method for the lines. This scheme takes into account the effect of the radiation on the atomic populations, and reduces to the photon diffusion approximation in regimes where that approximation is valid.

Profiles of the plasma density and temperature at various times in the plasma evolution have been presented. Calculated spectral emissions from the front and rear surfaces at various times have also been presented.

Comparisons with calculations omitting radiation show that radiation transport can significantly affect plasma evolution, leading to substantially different temperature and density profiles.

(e.g., see Fig. 8). Rearside heating at this time is due primarily to convection. In the first treatment, the beam is still being stopped near the center of the plasma, but radiation transport is keeping the rear side at a high temperature even after the beam turns off at 10 nsec.

Fig. 10 shows the time behavior of the density and temperature of the front side of the plasma. Here the effects of radiation transport are more pronounced; the radiationless case produces much higher temperatures and much lower densities. The marked drop in temperature after 10 nsec in the radiation transport case is due to radiative cooling.

Fig. 11 gives the energy history of the plasma along with the energy partitioning for the radiationless case. The plasma energy is equal to the deposited energy at all times. The thermal energy is much higher than in Fig. 6 for the radiation-hydro case; this indicates that radiation cooling occurs at the expense of the plasma thermal energy. This is also indicated by the much higher temperatures in the radiationless curves in Figs. 7-8. The potential energies are not very different in the two calculations. The radiationless case has higher kinetic energy at later times; this accounts for the greater widths of the plasma in this case.

These comparisons of the radiationless and hydro-radiation transport cases clearly establish the importance of radiation and radiation transport effects in hot plasmas for the conditions considered here. Further calculations are underway in order to determine the parameter space over which this situation prevails.

#### IV. COMPARISON WITH LASER-TARGET INTERACTION

It is of interest to make some qualitative comparisons with a simulation of a laser-aluminum target interaction at roughly the same incident energy intensity. Duston, et. al.<sup>17</sup> studied the interaction of a 1.06 micron laser beam at an intensity of  $10^{13}$  W/cm<sup>2</sup> and a long pulse length (3 nsec full width at half maximum) with an 8  $\mu$ m thick aluminum foil. Fig. 12 is taken from that study.

In the laser case, after the initial blow off plasma is formed, the beam does not penetrate into the target beyond the critical density surface, whereas the ion beam penetrates deep into the target, at least at

Figure 6 shows the energy history of the plasma and the partitioning of that energy. At early times, the radiated power is an insignificant fraction of the beam energy, but at late times, it becomes a significant portion of the energy budget. At about 12 nsec, it surpasses the total energy (sum of kinetic, potential, and thermal energies) in the plasma. At this point, more than half the energy deposited by the beam has been lost due to radiation<sup>13</sup>.

To investigate the importance of radiation transport, the simulation was repeated, but with radiation omitted. The CRE ionization dynamics treatment was retained, but the radiation was not included in the source and sink terms in the hydrodynamic equations, and optical pumping of the atomic levels was excluded. Fig. 7 shows temperature and density profiles at 3 nsec with and without radiation. Including radiation effects produces a more uniformly-dense plasma in this case. The densities are not very different, except that the profile without radiation shows a dip in the center and a much less dense blow off region in the front. The radiationless temperature profile also attains a higher maximum value.

Figure 8 shows similar comparisons at 10 nsec. Both density profiles exhibit gradients near the rear surface, but the radiationless density gradient is much steeper, and has a lower density blow off region in the front. Because there is no energy loss due to radiation, much higher temperatures result.

Figure 9 shows the temperature and density of the rearside of the plasma as a function of time when radiation is included and when it is omitted. The curves are very similar until about 4 nsec; after this time the rear side is denser and cooler when radiation is omitted. Since, at these times, the beam is stopped in the plasma well before it reaches the back side, the large temperature difference between 4 nsec and 10 nsec indicates that radiation transport plays a significant role in heating the rear side. This agrees with a conclusion reached in a study of the interaction of a  $10^{13}$  W/cm<sup>2</sup> laser pulse at 1.06  $\mu$ m wavelength on a thin 8.0  $\mu$ m Al foil [Duston, et.al<sup>17</sup>].

The density and temperature rise around 9 nsec in the radiationless case is due both to a shock reaching the rear surface and to deeper penetration by the beam. This deeper penetration results from generally lower plasma densities at later times than when radiation is included

The 15  $\mu\text{m}$  thickness is chosen because it corresponds approximately to the range of 1 MeV protons in cold solid density Al<sup>33</sup>. Hence, the beam is initially stopped within the target and deposits most of its energy near the back surface where the Bragg peak occurs in the stopping cross sections.

A point to be noted also in this regard is that, for consistency, the average charge obtained from solving the CRE equation is used throughout the calculation. Continuum lowering is not taken into account. This means that, near solid density, the average charge  $\bar{Z}$ , and hence the electron density, is probably low. The free electron contribution to stopping power is somewhat underestimated at early times in the plasma evolution. However, on a time scale of the order of nanoseconds, the plasma density is two orders of magnitude below solid density  $\rho_s$ , and the CRE  $\bar{Z}$  is valid.

Figures 1 and 2 show density and temperature profiles at different times as the plasma evolves. As may be noted from these figures, the plasma spreads and becomes more uniform in density and temperature as time increases.

Figures 3 through 5 show calculated spectra emitted from the front and rear sides of the plasma. In Fig. 3, at 0.5 nsec, the rear side at temperatures near 40 eV is about twice as hot as the front surface due to peaking of the stopping power near the rear surface. This results in a more intense rearside spectrum. As may be seen from Fig. 2, the temperature situation has reversed at later times, and at 4.31 nsec (Fig. 4), the front side is emitting a much more intense spectrum than the rear side. The peak intensity on the front side has risen two orders of magnitude and shifted to higher photon energies. The rear side intensity has also increased, but less dramatically. Some K shell emission in the region around one to two keV can be noted.

Front and rearside spectra at about 10 nsec (when the beam is shut off) are shown in Fig. 5. The front side spectrum is very similar to the 4.31 nsec spectrum, but the rear side intensity has increased as the plasma continues heating and becomes more uniform [see Figs. 1 and 2]. K shell emission is very prominent here. At later times when the plasma has cooled considerably and become very uniform, the spectra from both sides are very similar and have been reduced in intensity from the 10 nsec levels.

where  $m_p$  is the proton mass, and

$$\mu = \frac{m_B m_I}{m_B + m_I} . \quad (27)$$

#### 4. Enhanced Stopping Power From Collective Effects

The stopping power of a dense ion beam can differ from the sum of single particle stopping powers. One way in which this can occur is through phase mixing of the polarization wakes produced in the ambient medium by the beam particles. The magnitude of this particular effect is similar to that given by McCorkle and Iafrate<sup>32</sup> for electron beams,

$$S_b = S_0 (1 + 2\pi n_B a^3/3) \quad (28)$$

where  $S_b$  is the enhanced stopping power,  $S_0$  is the single particle stopping power,  $n_B$  is the beam number density and  $a$  is the ratio of the beam velocity and local plasma frequency

$$a = v_B / \omega_{pe} . \quad (29)$$

For the case considered below, a 1 MeV proton beam with a flux  $n_B v_B = 10^{26}$   $\text{cm}^{-2} \text{sec}^{-1}$  on a solid density aluminum target, the correction to the stopping power is quite small.

### III. RESULTS

The interaction of a monoenergetic 1 MeV proton beam with a planar aluminum slab of 15  $\mu\text{m}$  thickness is investigated. The beam is assumed to consist of a square-shaped pulse of 10 nanosecond duration with a flux of  $10^{26}$  protons/ $\text{cm}^2\text{-sec}$ . The beam intensity on target is  $1.6 \times 10^{13}$   $\text{W/cm}^2$ , which is comparable to the intensities available with current pulsed-power generators.

The first term in  $S_f(V)$  is the short range ion-electron binary-encounter scattering term and is taken from the work of Campbell,<sup>29</sup> who adapted it from Brueckner and Brysk.<sup>30</sup> The second term is the polarization term and is taken from Pines and Bohm.<sup>31</sup> For distances larger than  $D$ , the plasma acts as a continuous medium, and distant collisions cause loss of energy by the excitation of plasma oscillations, which appear as an oscillating wake behind the projectile.

### 3. Interaction with Plasma Ions

For stopping power due to the plasma ions, an expression taken from Campbell<sup>29</sup> and Mehlhorn<sup>18</sup> is used;

$$\left(\frac{dE}{dx}\right)_i = \frac{\rho(x)}{m_i} S_i(V), \quad (21)$$

where

$$S_i(V) = \frac{4\pi e^4 Z_B^2 \bar{Z}^2}{m_i V^2} \ln \Lambda F(\xi) \quad (22)$$

where

$$\xi^2 = m_i V^2 / 2kT_i, \quad (23)$$

$$F(\xi) = \text{erf}(\xi) - \frac{2}{\sqrt{\pi}} \left(1 + \frac{m_i}{m_B}\right) \xi e^{-\xi^2} \quad (24)$$

$$\ln \Lambda = (1/2) \ln (1 + b_{\max}^2 / b_{\min}^2). \quad (25)$$

$b_{\max}$  is set equal to  $D$ , and  $b_{\min}$  is given by

$$b_{\min} = \text{MAX} \left\{ \frac{Z_B \bar{Z} e^2}{\mu m_p V^2}; \frac{h}{2\mu m_p V} \right\} \quad (26)$$

The bound electron stopping power is calculated from

$$\left(\frac{dE}{dx}\right)_b = (\rho(x)/m_I) S_b(v) \quad (15)$$

where  $S_b(v)$  is the stopping cross section in  $\text{erg cm}^2$  and is obtained from Eq. (14).

## 2. Interaction With Free Electrons

For heated target materials, the atoms become ionized, and stopping due to free electrons must be considered. The free electron stopping power is calculated from

$$\left(\frac{dE}{dx}\right)_e = \frac{\rho(x)}{m_I} S_f(v), \quad (16)$$

with

$$S_f(v) = \frac{2\pi e^4 Z_B^2 \bar{Z}}{mV^2} F(\xi) \left\{ \ln \left(1 + \frac{D^2}{b^2}\right) + \ln (1 + 4\xi^2) \right\}, \quad (17)$$

where  $\bar{Z}$  is the average charge of the target ions,  $D$  is the Debye shielding length, and

$$\xi = (m_B V^2 / 2kT)^{1/2}, \quad (18)$$

where  $kT$  is the electron temperature, and

$$F(\xi) = \text{erf}(\xi) - 2\xi e^{-\xi^2} / \sqrt{\pi}. \quad (19)$$

The quantity  $b$  is the minimum impact parameter for electron-ion scattering and is given by

$$b = \text{MAX} \left\{ \frac{Z_B e^2}{mV^2}, \frac{h}{2mV} \right\}, \quad (20)$$

i.e., the maximum of either the classical or quantum-mechanical impact parameter defined by the uncertainty principle.



By use of least-squares methods, these MPP data were fitted by a function of the form

$$F_q(y) = \exp (A_q + B_q y + C_q y^2 + D_q y^3) , \quad (14)$$

where  $y = \ln (E/E_0)$ , and  $E_0 = 0.1$  MeV.  $F_q(y)$  gives stopping cross sections in units of  $10^{-15}$  eV cm<sup>2</sup>/atom. Table 1 gives the fitting parameters  $A_q$ ,  $B_q$ ,  $C_q$  and  $D_q$  for each value of  $q$ . All the fits were within 7%, except for  $q=3$ , where the maximum deviation was 9%. Thus, Eq. (14) yielded reasonably good fits to the calculated cross sections.

In the treatment of the beam-target interaction, the average ionic charge  $\bar{Z}$  in a given cell is used to obtain stopping power. For non-integer values of  $\bar{Z}$ , Eq. (14) is used for  $q$  and  $q+1$ , where  $q$  is the integer part of  $\bar{Z}$ , and the stopping cross section for  $\bar{Z}$  is obtained by linear interpolation between  $F_q(y)$  and  $F_{q+1}(y)$ .

For  $q=0$ ,  $q=1$  and  $q=2$ , the MPP data, and hence the fits, are monotonically decreasing for energies  $\geq 0.1$  MeV. For these cases, a local-oscillator model (LOM)<sup>27,28</sup>, is used to calculate bound electron stopping power for energies below 0.1 MeV. These LOM cross sections are adjusted to match the MPP data at 0.1 MeV, and the cross sections at lower energy are scaled accordingly. The MPP data for  $q = 8, 9$ , and  $10$  are also monotonically decreasing for  $E \geq 0.1$  MeV, but at these charge levels, the stopping power is dominated by the free-electron contribution; hence, no adjustments to the bound electron stopping power at energies less than 0.1 MeV are made. The fits are just extended below 0.1 MeV.

For the other  $q$  values between 3 and 11, the MPP data peak in the 0.1 MeV - 100 MeV range; hence the fits are extended below 0.1 MeV to obtain low energy cross section data. For  $q > 11$ , the bound electron stopping power is set to some low value, since free electron stopping dominates.

From an energetics point of view, errors in the low energy regime are not as critical as at higher energies. For example, a proton with an initial energy of one MeV has lost 90% of its energy and is near the end of its range by the time it degrades to a 0.1 MeV proton. Therefore, errors in stopping power below 0.1 MeV will not affect energy deposition profiles very much.

#### d. Beam Dynamics and Energy Deposition

It is assumed that, on the timescale of the slab response (several nanoseconds), the beam maintains uniform flow, that is

$$\rho_B u_B = \dot{m} = \frac{J m_B}{e Z_B} \quad (10)$$

where  $\rho_B$  and  $u_B$  are the local mass density and axial velocity of the beam. The mass flux  $\dot{m}$  is assumed constant up to the point the beam is stopped.  $J$  is the beam current per unit area;  $m_B$  and  $Z_B$  are the mass and charge of a beam ion.

For a relativistic beam with negligible thermal spread, the kinetic energy of a beam ion is related to the local velocity by

$$E_B = \frac{m_B c^2}{\sqrt{1-u_B^2/c^2}} - m_B c^2. \quad (11)$$

The energy is also related to the stopping power by

$$E_B(x') = E_0 - \int_{-\infty}^{x'} \left( \frac{dE}{dx} \right)_T dx, \quad (12)$$

where  $E_0$  is the initial energy,  $x'$  is the distance into the slab, and the total stopping power is given by the sum of the ion-free electron, ion-bound electron and ion-plasma ion interactions,

$$\left( \frac{dE}{dx} \right)_T = \left( \frac{dE}{dx} \right)_e + \left( \frac{dE}{dx} \right)_b + \left( \frac{dE}{dx} \right)_i. \quad (13)$$

#### 1. Interaction With Bound Electrons

Recently, McGuire, Peek, and Pitchford<sup>19</sup> (MPP) published detailed calculations of stopping power cross sections of protons by Al ions. By using the generalized-oscillator-strength formulation of the Born approximation, they calculated tables of stopping cross sections for protons interacting with Al ions of charge  $q$ , where  $0 \leq q \leq 11$ , in the energy range 0.1 MeV to 100 MeV.

The multifrequency model<sup>24</sup> solves the equation of radiation transport at a large number of discrete frequencies, providing resolution of emission lines, recombination edges and absorption edges. It provides accurate radiation transport at high density, and gives spectral details such as self-absorption features. However, a large number of frequencies is required to provide adequate resolution, and it tends to be a relatively costly method.

The hybrid model uses the multifrequency formalism to transport the continuum (bound-free and free-free) radiation and frequency-integrated escape probabilities to transport the lines. Continuum opacities are interpolated from the multifrequency mesh and folded into the line transport calculations. The line opacities are assumed to have negligible impact on the continuum energetics.

In all of the models outlined above, local ionization state-dependent inner-shell opacities are included, since these processes are very important in the cool, dense plasma regions. Inner-shell photoionization cross sections for the neutral element are taken from the fits by Biggs and Lighthill<sup>25</sup>. For ions, inner shell photoionization cross sections are estimated using the neutral cross section data, but with the absorption edges shifted; the positions of the ionization-dependent absorption edges are based on the Hartree-Fock calculations of Clementi and Roetti.<sup>26</sup>

The local rate of energy change in zone  $j$ , due to radiation transport is given by

$$\dot{\epsilon}_j = - \sum_P (F_{Pj} - \sum_k C_{Pkj} F_{Pk}) \quad (9)$$

where  $F_{Pk}$  is the rate of energy loss in zone  $k$  due to a discrete radiative process (or frequency group)  $P$ , and  $C_{Pkj}$  is the radiative coupling of zone  $k$  to zone  $j$  for that process. The couplings are functions of opacity, integrated over process and photon path. In the probabilistic model, a matrix of couplings must be computed for each bound-bound, bound-free and free-free process; for the multifrequency model, they must be computed for each discrete frequency. In this way, the net cooling and heating by radiation emission and absorption among the various zones of the plasma is accounted for accurately.

The ionization and excitation energy can also be calculated by

$$\epsilon_I = \sum_i \chi_i f_i N_I, \quad (8)$$

where  $\chi_i$  is the energy of level  $i$ , measured from the ground state of the neutral atom.

### c. Radiation Emission and Transport

Radiation emission from a plasma and its opacity are dependent on the local atomic level population densities. Except for optically thin plasmas, however, the level populations depend on the radiation field, since optical pumping via photoionization and photoexcitation can produce significant population redistribution. Thus, the ionization and radiation transport processes are strongly coupled and must be solved self-consistently. In this model, an iterative procedure<sup>22</sup> is used, where level populations are calculated using the radiation field from the previous iteration, then using these populations to calculate a new radiation field and recalculating populations until convergence is reached.

Three distinct radiation transport schemes have been developed, and can be used interchangeably in the code: A probabilistic scheme, a multifrequency scheme and a hybrid method. Descriptions of these transport methods have appeared elsewhere; in this paper, their general properties will be outlined.

The probabilistic model<sup>23</sup> forms local angle and frequency averaged escape probabilities for each emission line and for each bound-free process. Free-free radiation is treated with a multifrequency formalism. The radiation transport and emission spectra are calculated from these escape probabilities. The method is cost-effective, can treat comprehensive atomic models and provides good overall energetics, but cannot calculate certain spectral details and breaks down at very high densities.

thermal equilibration times are short compared with the time scales of the energy input and changes in the hydrodynamic variables.

The local rate of change of energy due to radiation transport  $\dot{\epsilon}_{\text{rad}}$ , and that due to the beam deposition  $\dot{\epsilon}_{\text{dep}}$ , will be discussed in Sections C and D.

#### b. Ionization and Atomic Physics

The ionic populations in the plasma may be characterized by a set of atomic rate equations of the form

$$\frac{df_i}{dt} = \sum_j W_{ji} f_j - \sum_j W_{ij} f_i \quad (6)$$

where  $f_i$  is the fractional population of atomic level  $i$ , and  $W_{ji}$  is the net reaction rate describing the transition from initial state  $j$  to final state  $i$ . An equation of this type is constructed for each of the atomic levels included in the model.

For sufficiently dense plasmas of the sort we expect to model with the ion-beam code, the effective populating and depopulating rates are generally fast compared with the hydrodynamic response. An equilibrium assumption can be justified, which involves dropping the explicit time dependence in equation (6). The plasma is then said to be in collisional-radiative equilibrium (CRE),<sup>21</sup> whereby the plasma ionization state responds instantaneously to changes in hydrodynamic quantities.

The rate coefficients that are used to calculate the populating and depopulating rates,  $W_{ji}$ , are calculated using various scattering techniques. The processes included in this calculation and the methods used in calculating the corresponding rate coefficients are summarized elsewhere<sup>17</sup>.

Once the set of rate equations (including the radiation transport) has been solved for the level populations,  $f_i$ , the electron density can be calculated,

$$N_e = \sum_i z_i f_i N_I \quad (7)$$

where  $z_i$  is the ionic charge of level  $i$  and  $N_I$  is the total ion density.

### a. Hydrodynamics and Thermal Conduction

The basic hydrodynamic variables of mass, momentum, and total energy are transported in one dimension using a numerical scheme with a sliding-zone version of flux-corrected transport.<sup>20</sup> A special gridding algorithm is used which moves zones in a Lagrangian fashion and adjusts the mesh in order to resolve steep gradients in the flow. The hydrodynamic equations solved are

$$\frac{D\rho}{Dt} = \frac{\partial \rho}{\partial t} + \frac{\partial}{\partial x} (\rho u) = 0, \quad (1)$$

$$\frac{D(\rho u)}{Dt} = - \frac{dP}{dx}, \quad (2)$$

$$\begin{aligned} \frac{D\varepsilon_T}{Dt} = & - \frac{\partial}{\partial x} (uP) + \dot{\varepsilon}_{\text{rad}} + \dot{\varepsilon}_{\text{dep}} \\ & + \frac{\partial}{\partial x} \left\{ \eta N \frac{\partial T}{\partial x} \right\}, \end{aligned} \quad (3)$$

where  $\rho$  is mass density,  $u$  is velocity,  $P$  is pressure,  $\varepsilon_T$  is total energy density,  $\dot{\varepsilon}_{\text{rad}}$  is the rate of energy loss or gain due to radiation,  $\dot{\varepsilon}_{\text{dep}}$  is the rate of energy gain due to the beam deposition process,  $\eta$  is the thermal conductivity, and  $N$  is the ion density. The thermal conduction is calculated implicitly, using an iterative Crank-Nicholson scheme.

Since densities did not much exceed solid density in this study, a simple equation of state was assumed with

$$P = \frac{2}{3} (\varepsilon_T - \frac{1}{2} \rho u^2 - \varepsilon_I), \quad (4)$$

where  $\varepsilon_I$  is the ion potential energy due to ionization and excitation. A single temperature model was employed,

$$kT = \frac{P}{(\rho/m_I) (1+\bar{Z})}, \quad (5)$$

where  $m_I$  is ion mass, and  $T$  is temperature. The ionization energy,  $\varepsilon_I$ , and effective charge,  $\bar{Z}$  are calculated from the ionization-radiation equations which are explained below. A single temperature assumption is valid in the solid dense material as well as in the beam deposition region, since

Table 1 — Least-square-fitting parameters to the MPP stopping powers\*

q	A <sub>q</sub>	B <sub>q</sub>	C <sub>q</sub>	D <sub>q</sub>
0	3.135	-4.415 (-1)	-2.592 (-2)	-1.031 (-3)
1	2.773	-3.534 (-1)	-3.719 (-2)	-5.234 (-4)
2	2.159	-8.853 (-2)	-9.409 (-2)	3.625 (-3)
3	1.012	6.257 (-1)	-2.644 (-1)	1.651 (-2)
4	8.459 (-1)	5.977 (-1)	-2.480 (-1)	1.482 (-2)
5	6.575 (-1)	5.506 (-1)	-2.331 (-1)	1.374 (-2)
6	5.423 (-1)	4.501 (-1)	-2.085 (-1)	1.212 (-2)
7	4.447 (-1)	2.828 (-1)	-1.564 (-1)	7.782 (-3)
8	3.716 (-1)	8.571 (-2)	-1.072 (-1)	4.287 (-3)
9	3.148 (-1)	-1.870 (-1)	-3.894 (-2)	-4.858 (-4)
10	-4.684 (-1)	-2.246 (-1)	6.746 (-3)	-5.082 (-3)
11	-7.250	2.867	-5.093 (-1)	2.388 (-2)

\* Numbers in parentheses indicates powers of ten

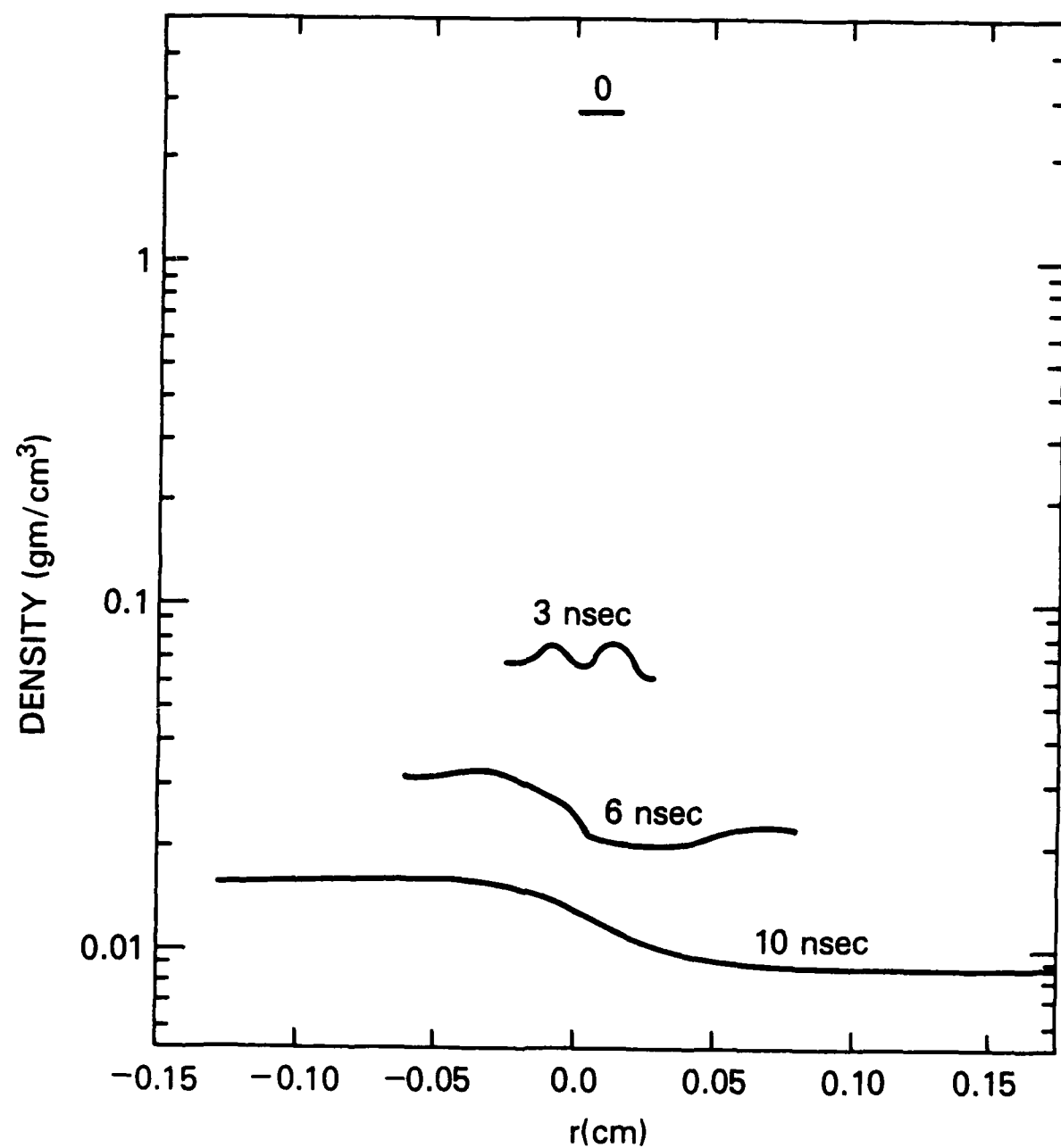


Fig. 1 — Density profiles at different times in the plasma evolution



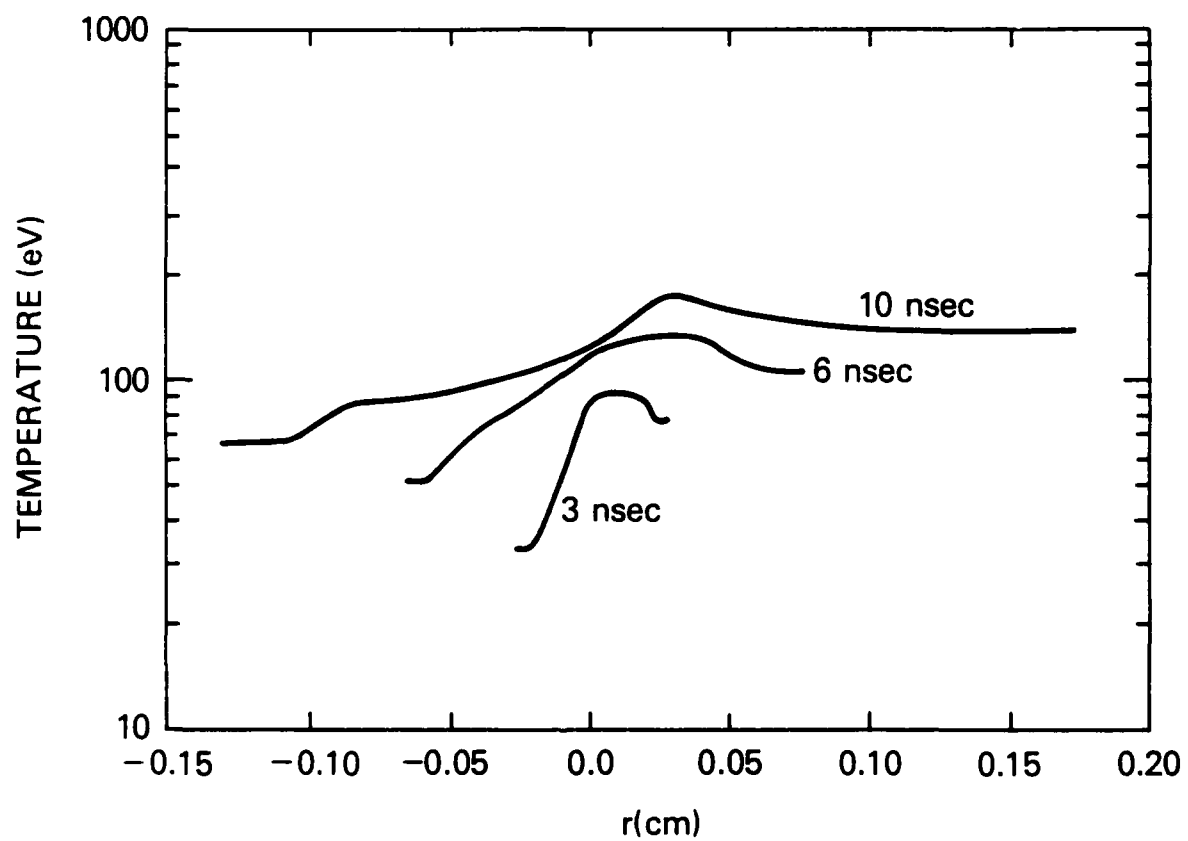


Fig. 2 — Temperature profiles at different times in the plasma evolution

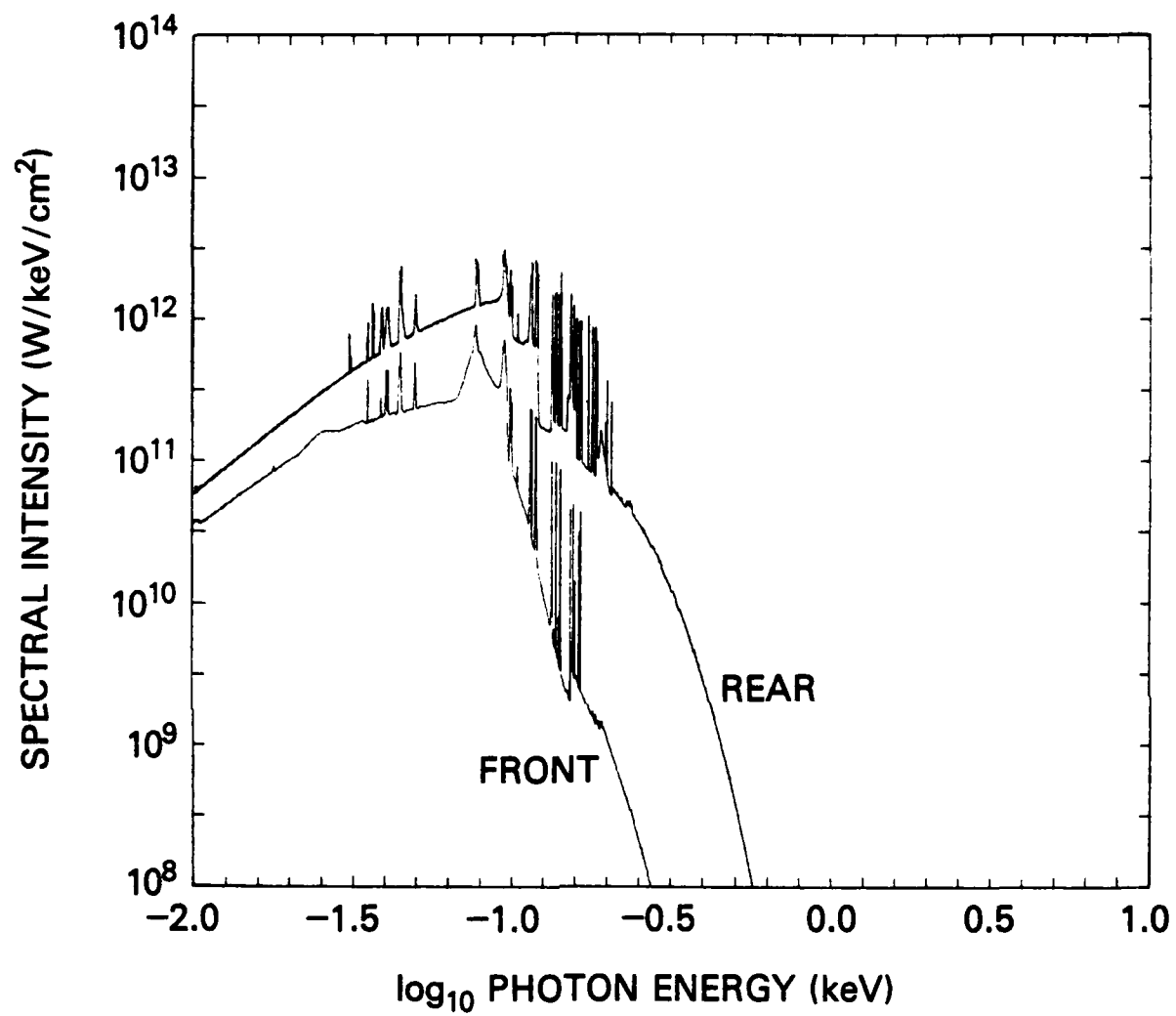


Fig. 3 — Front and rear side spectra at 0.5 nsec

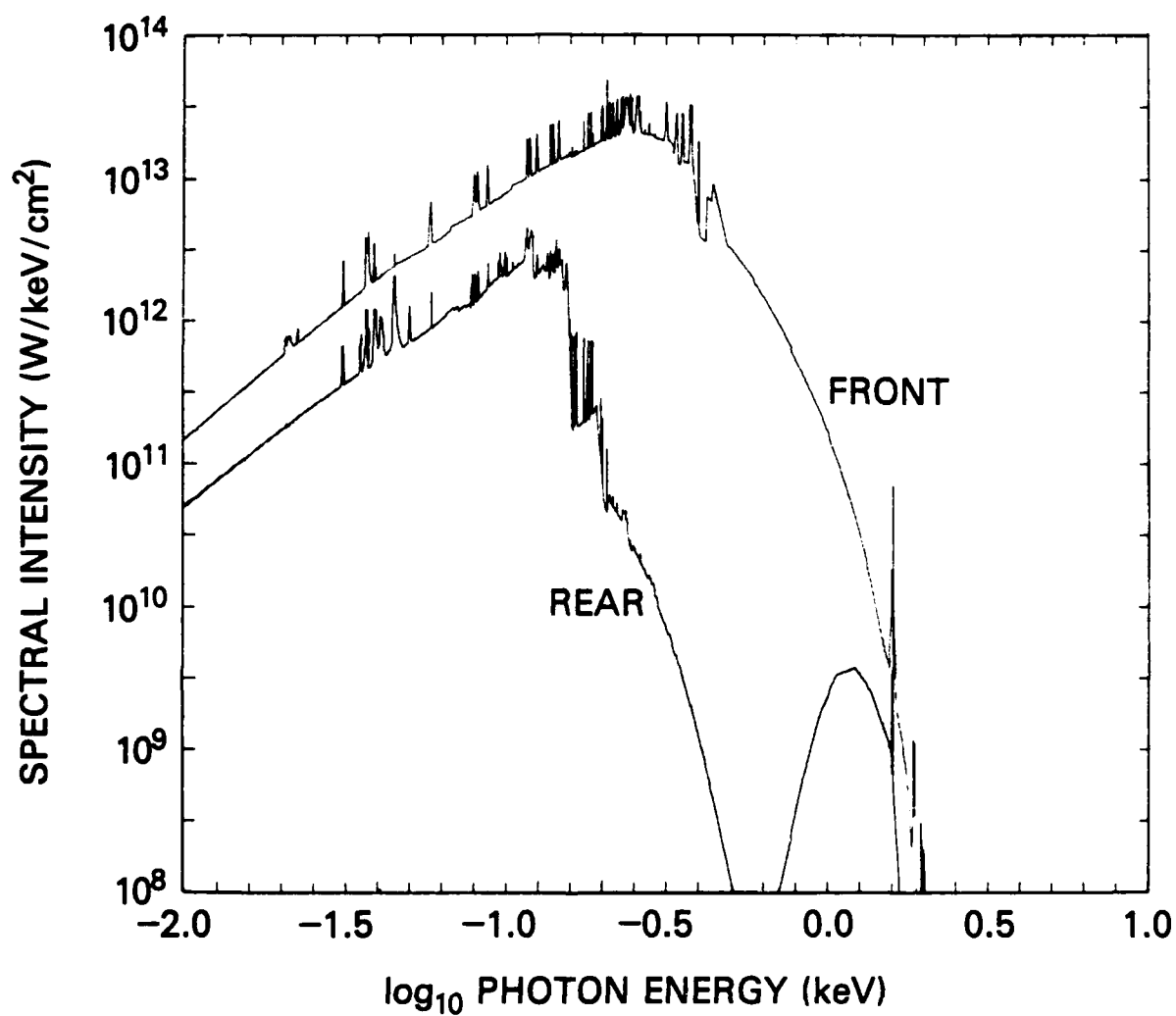


Fig. 4 — Front and rear side spectra at 4.31 nsec

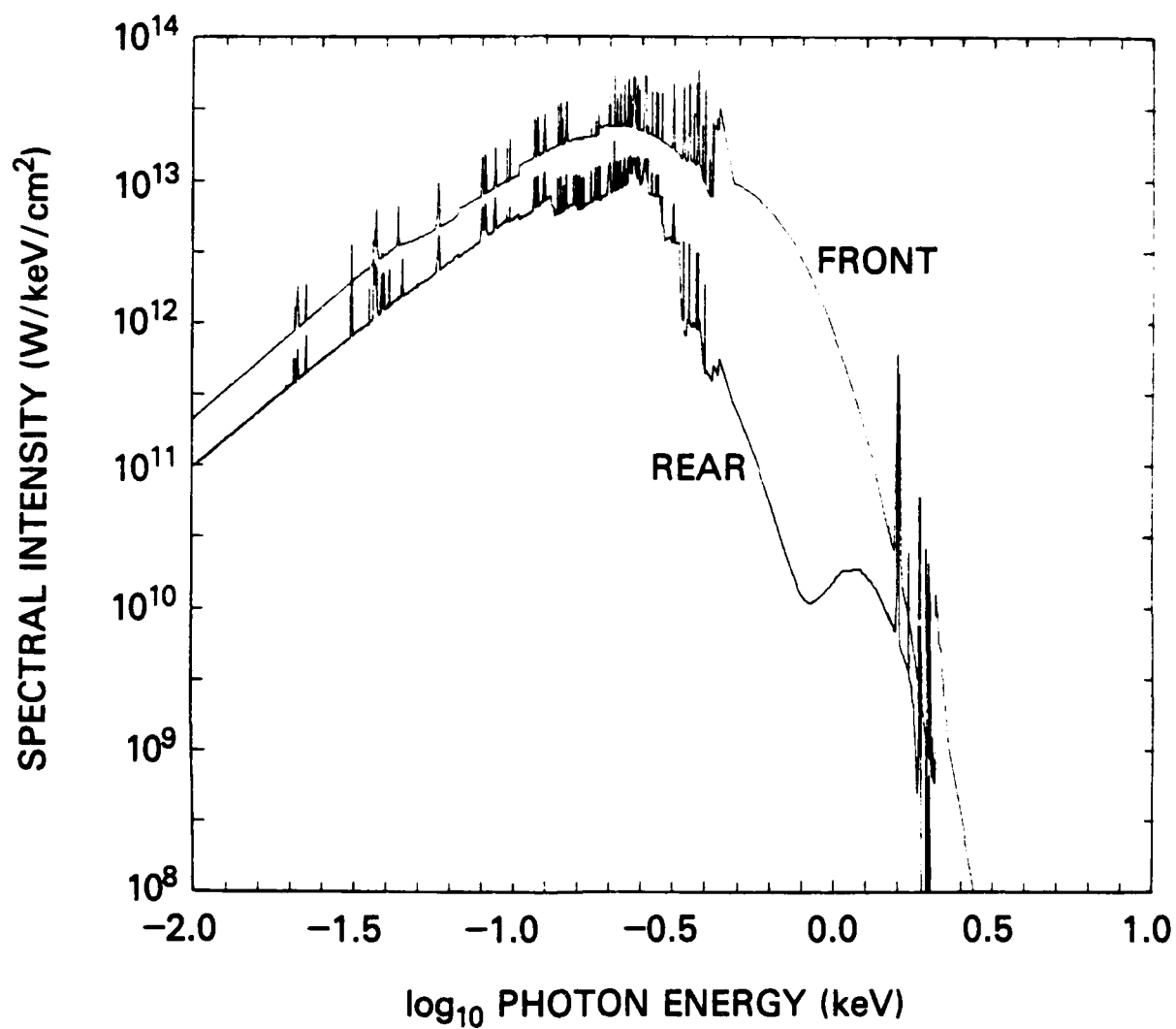


Fig. 5 — Front and rear side spectra at 10 nsec

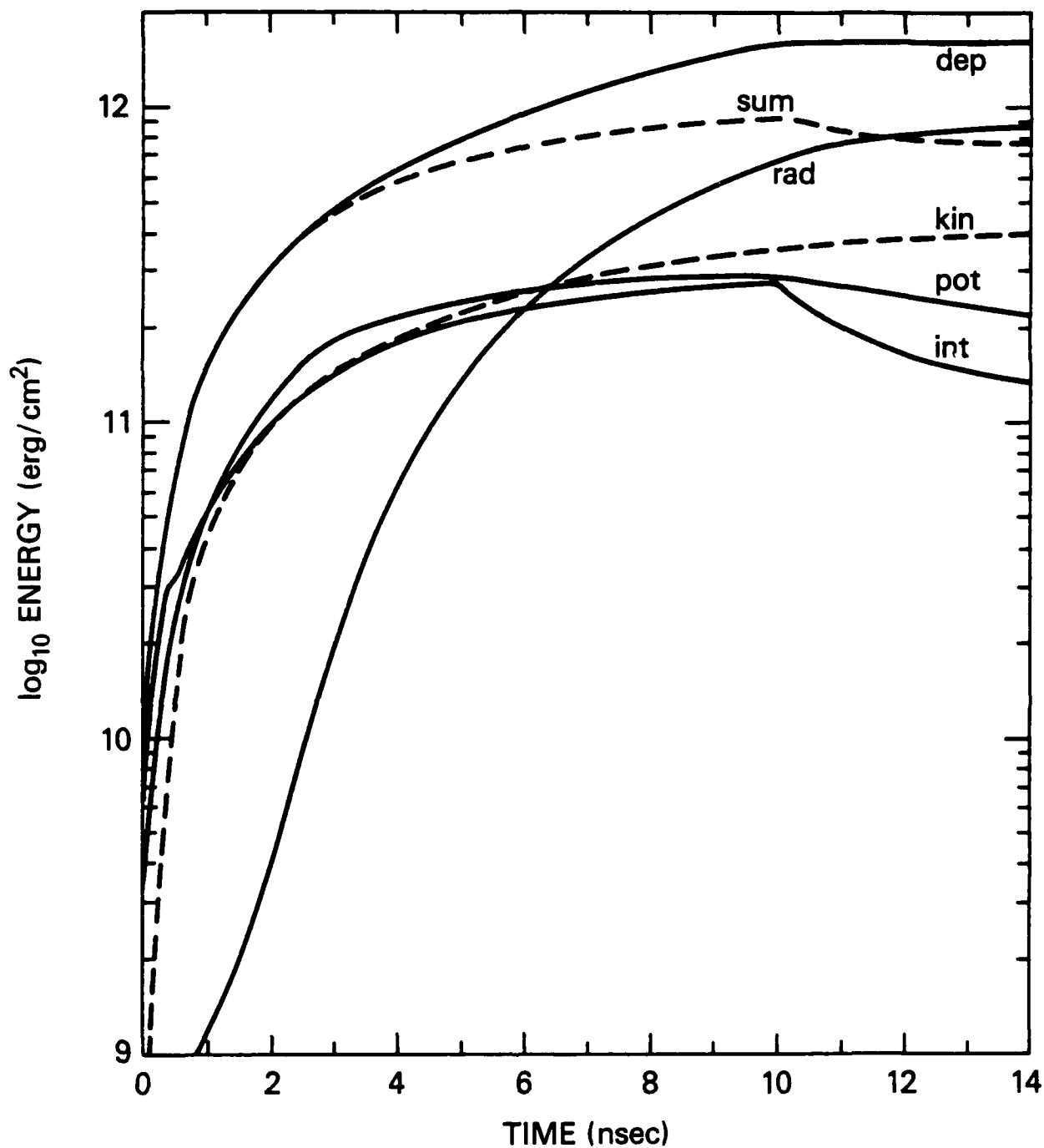


Fig. 6 — Beam-target energy partitioning as a function of time, including beam deposition (dep), total plasma energy (sum), plasma kinetic energy (kin), plasma thermal energy (int), ionization energy (pot) and radiated energy (rad).

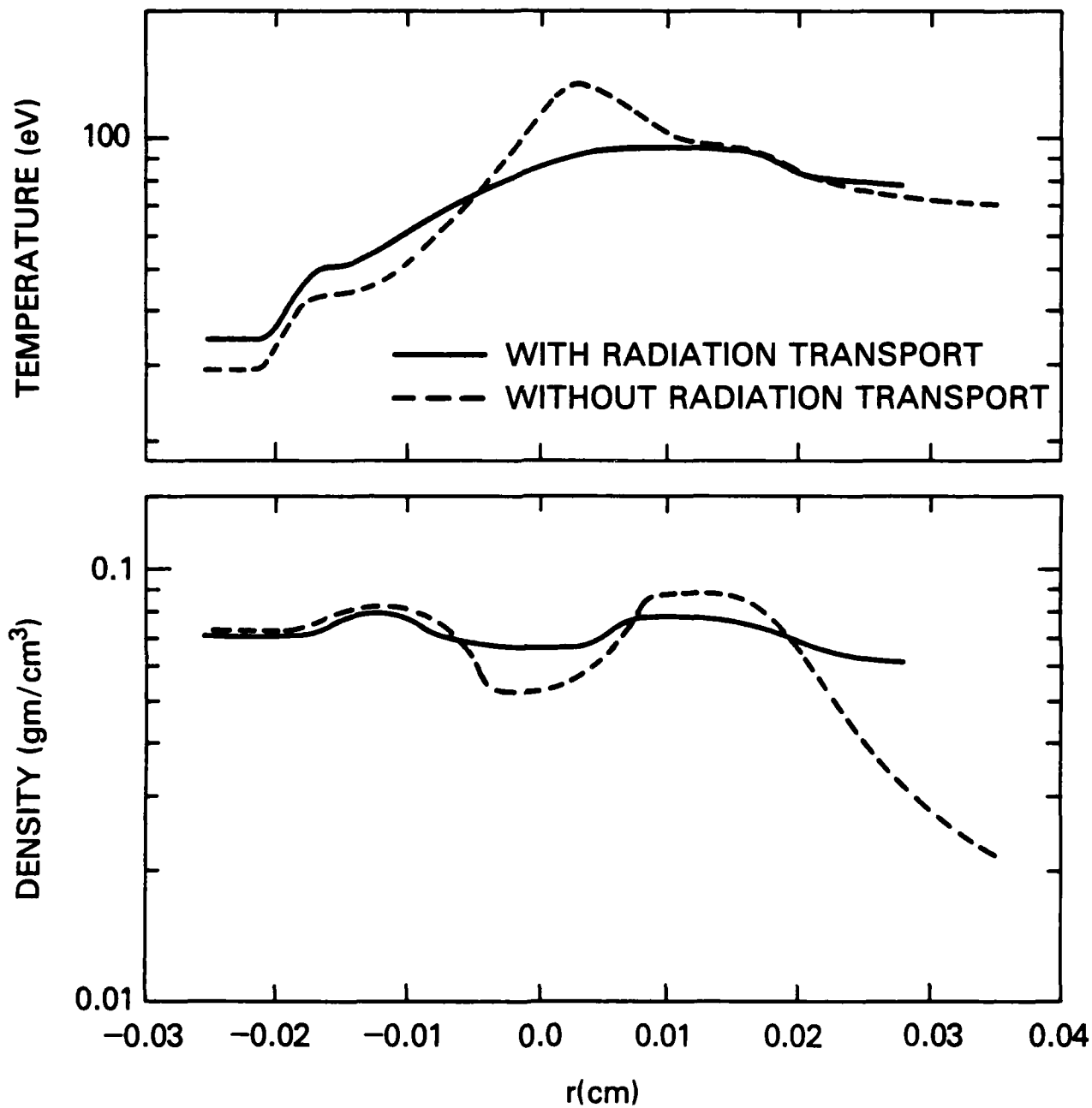


Fig. 7 — Comparison of temperature and density profiles at 3 nsec with and without effects of radiation

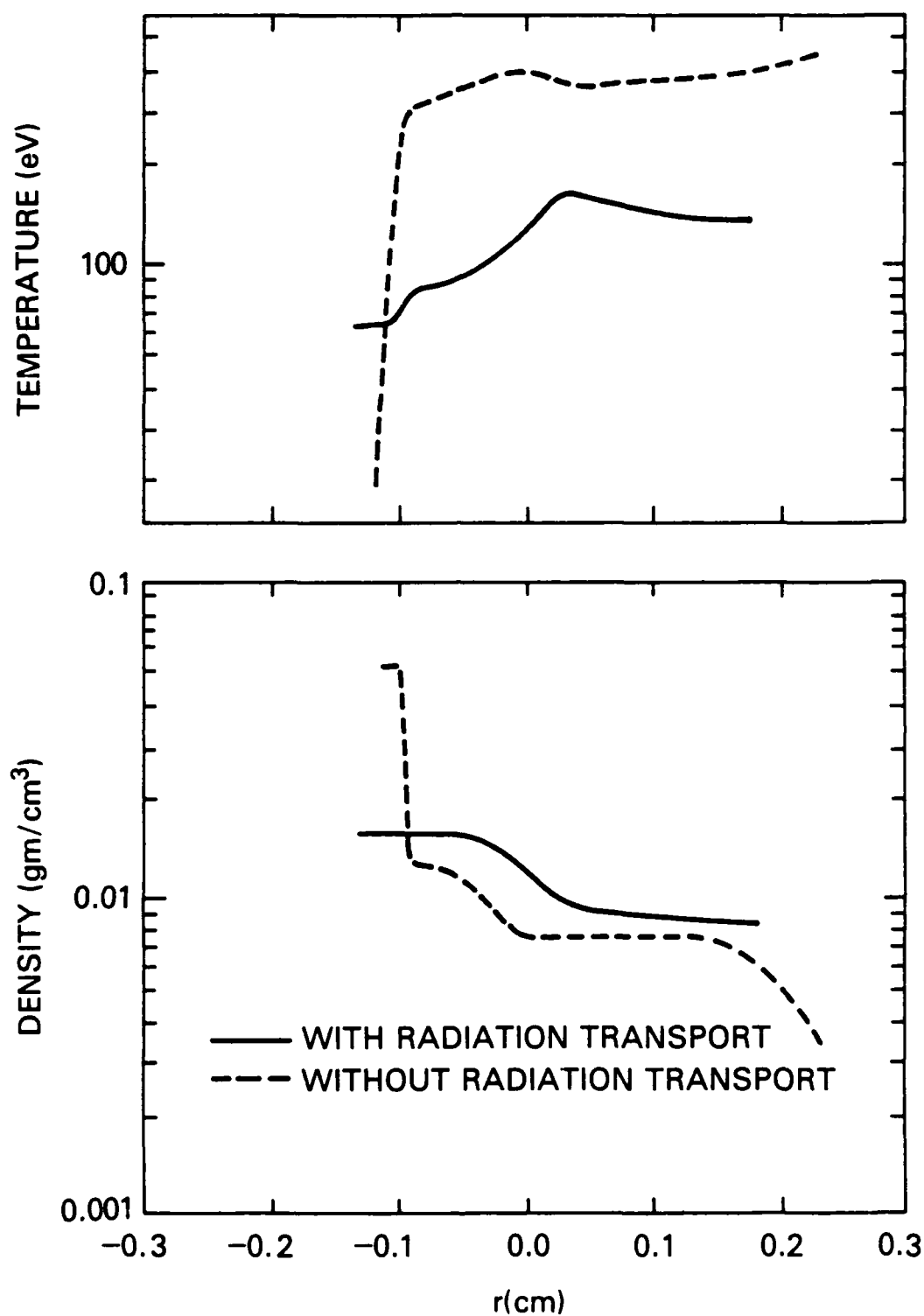


Fig. 8 — Comparison of temperature and density profiles at 10 nsec with and without effects of radiation

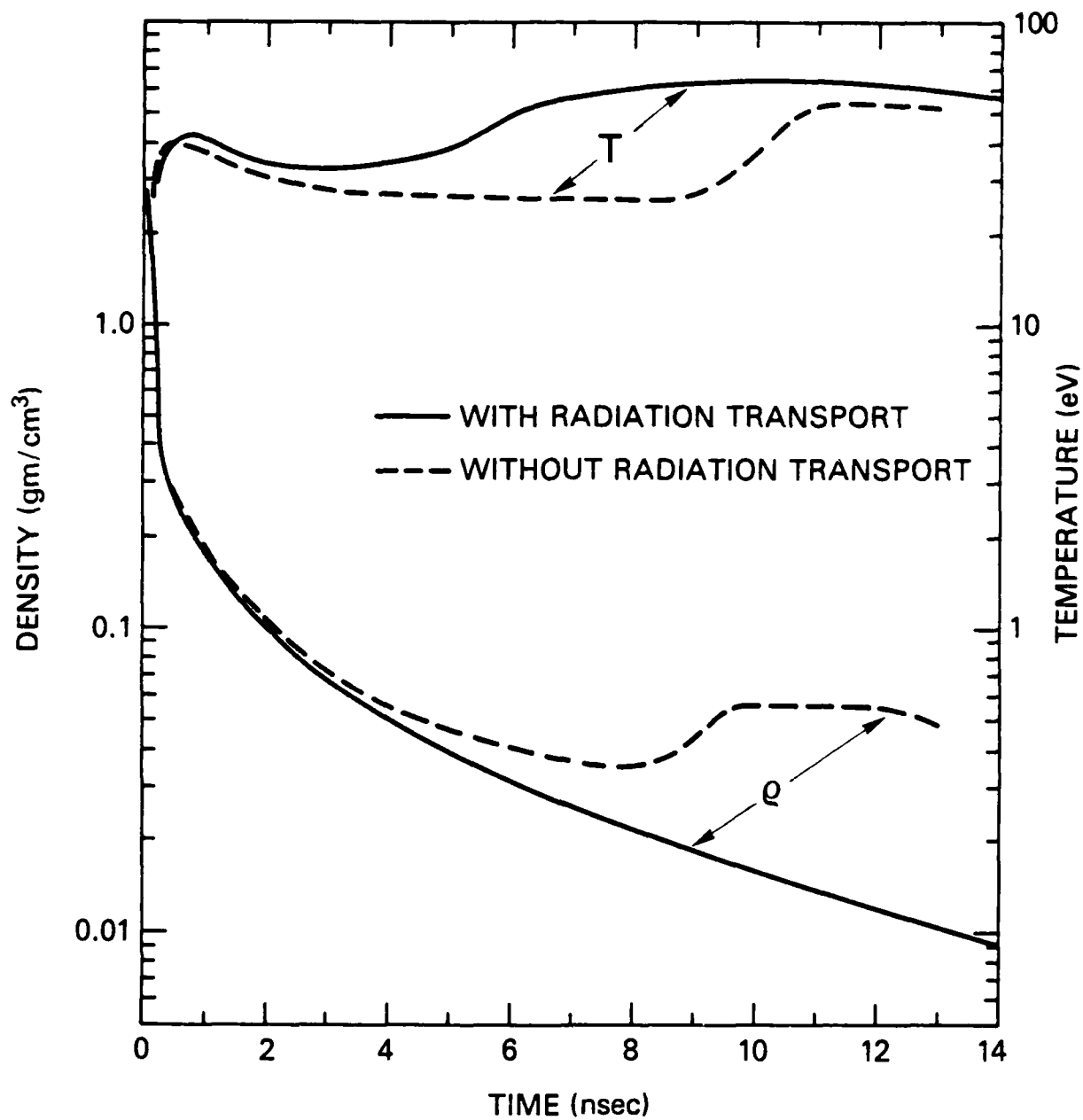


Fig. 9 — Temperature and density history of the rear surface of the plasma with and without radiation transport. T is temperature and  $\rho$  is density.



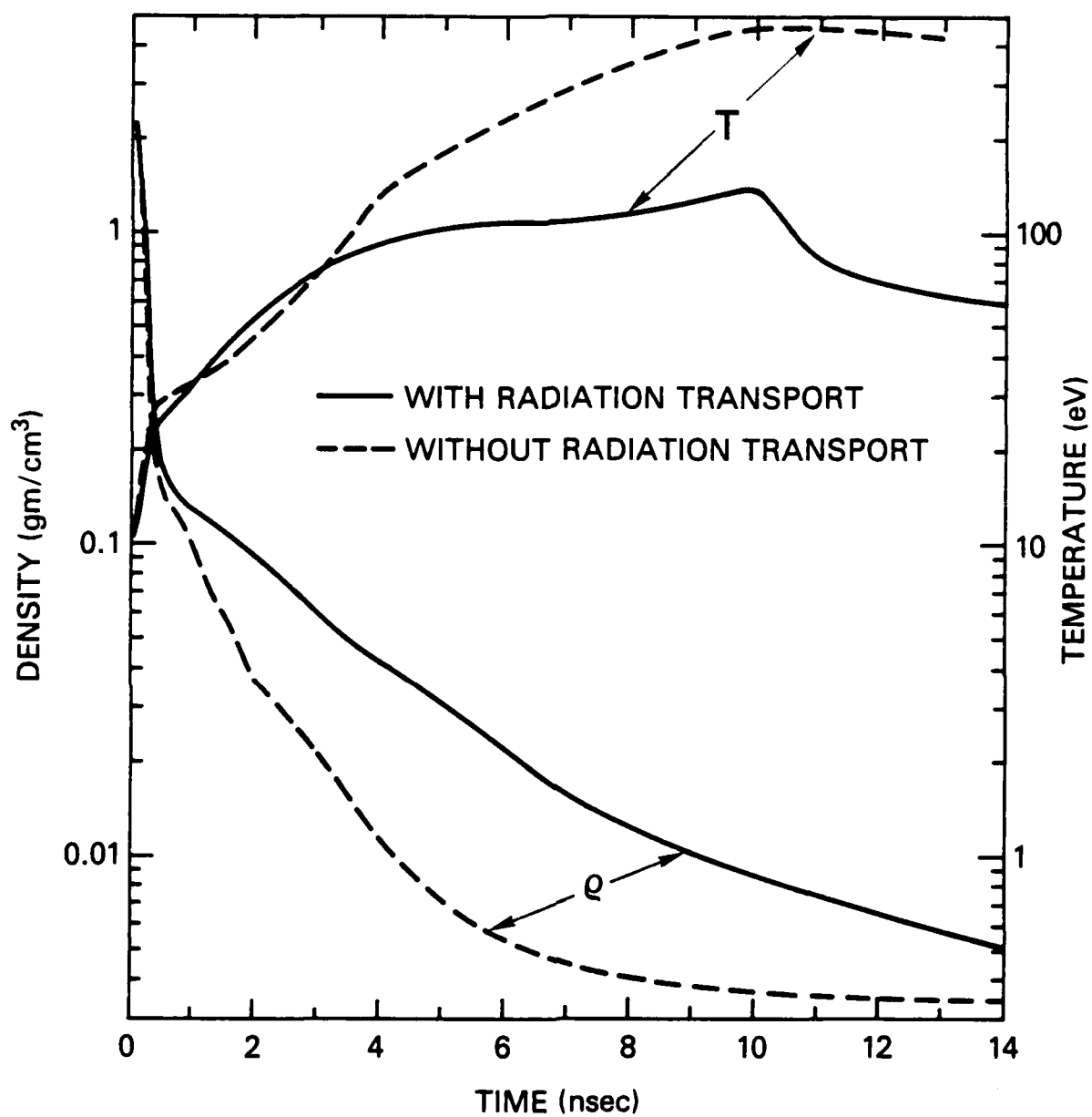


Fig. 10 — Temperature and density history of the front surface of the plasma with and without radiation transport. T is temperature and  $\rho$  is density.

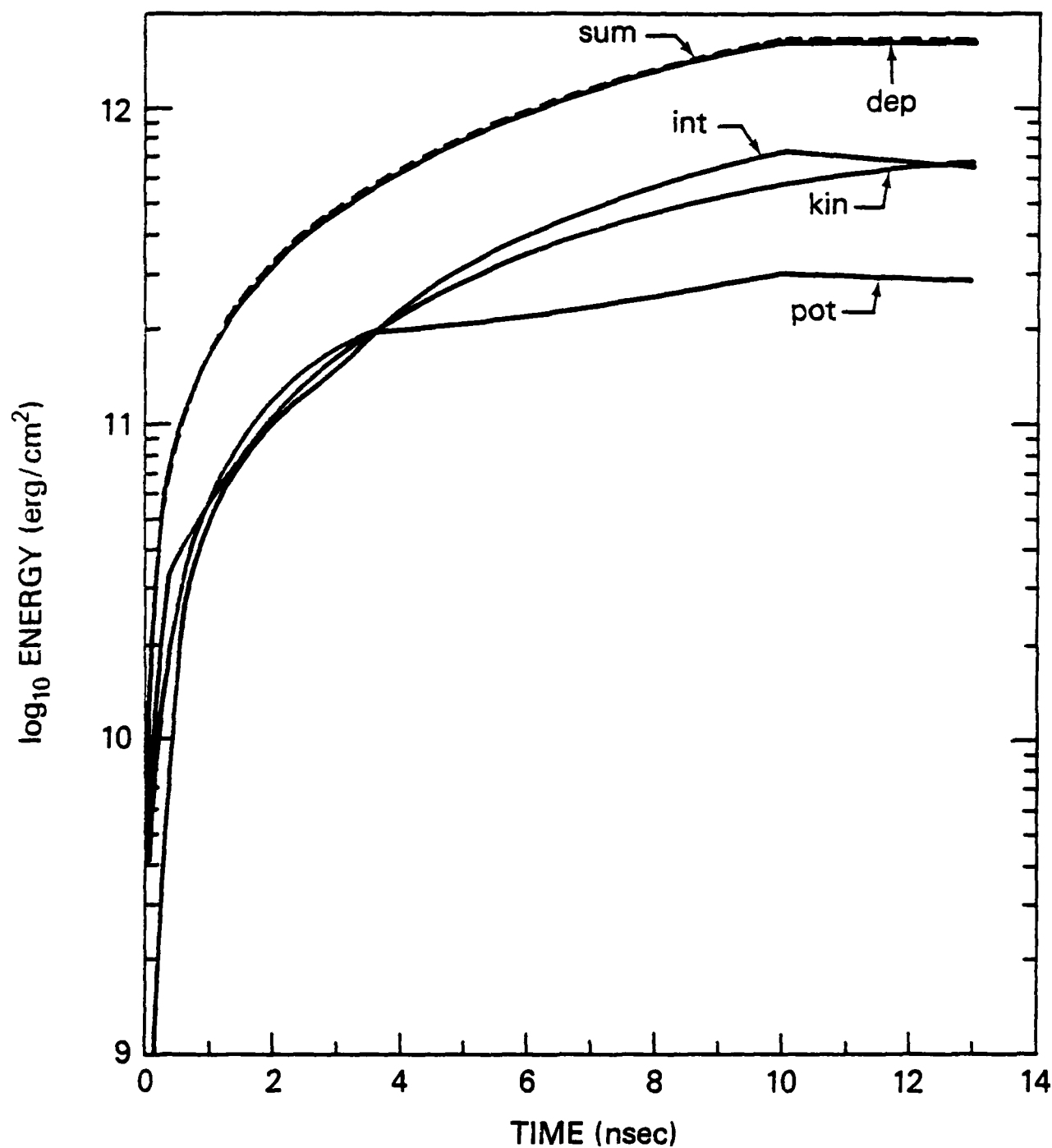


Fig. 11 — Beam-target energy partitioning when radiation effects are omitted (same labels as Fig. 6).

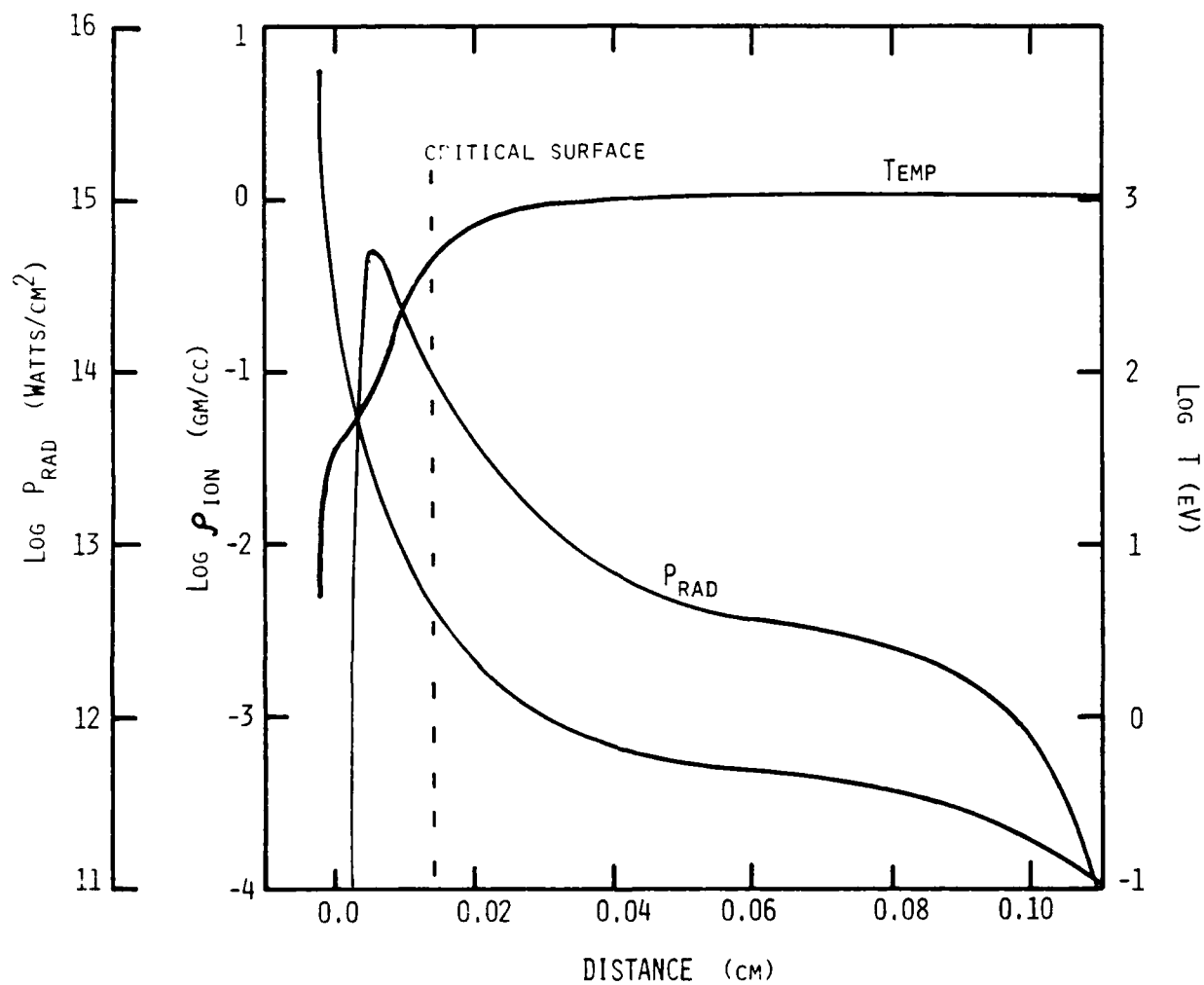


Fig. 12 — Temperature, density, and radiative cooling profiles at about 5 nsec in the laser heated foil study (Ref. 31).

## References

1. S. A. Goldstein, G. Cooperstein, R. Lee, D. Mosher, and S. J. Stephanakis, Phys. Rev. Lett. 40, 1504 (1978).
2. F. C. Young, D. Mosher, S. J. Stephanakis, S. A. Goldstein, and T. A. Mehlhorn, Phys. Rev. Lett. 49, 549 (1982).
3. D. J. Johnson, G. W. Kuswa, A. V. Farnsworth Jr., J. P. Quintenz, R. J. Leeper, E. J. T. Burns, and S. Humphries Jr., Phys. Rev. Lett. 42, 610 (1979).
4. E. J. T. Burns, D. J. Johnson, A. V. Farnsworth, Jr., G. W. Kuswa, G. A. Doschek, and U. Feldman, Appl. Phys. Lett. 35, 140 (1979).
5. L. P. Mix, E. J. T. Burns, D. L. Fehl, D. L. Hanson, and D. J. Johnson, Proceedings of the Conference on Low Energy X-Ray Diagnostics, Monterey, Cal. (1981).
6. R. B. Miller, An Introduction to the Physics of Intense Charged Particle Beams, (Plenum Press, New York, 1982).
7. H. J. Doucet and J. M. Buzzi, editors High Power Beams 81, Ecole Polytechnique, Palaiseau, France (1981).
8. R. G. Evans, Rutherford and Appleton Laboratories Report RL-81-022 (1981).
9. E. Nardi and Z. Zinamon, Phys. Rev. Lett. 49, 1251 (1982).
10. E. Nardi, E. Peleg, and Z. Zinamon, Phys. Fluids 21, 574 (1978); Appl. Phys. Lett. 39, 46 (1981).
11. E. Peleg and Z. Zinamon, Phys. Fluids 24, 1527 (1981).
12. Yu. V. Afanas'ev, V. A. Isakov, and O. N. Krokhin, Sov. Phys. JETP 54, 910 (1981).
13. A. V. Dobkin and I. V. Nemchinov, Sov. J. Plasma Phys. 8(1), 54 (1982).
14. S. Miyamoto, T. Ozaki, K. Imasaki, S. Higaki, S. Nakai, and C. Yamanaka, Institute of Laser Engineering, Osaka University, Japan, ILE 8118P (1981).
15. M. Tamba, N. Nagata, S. Kawata, and K. Niu, Institute of Plasma Physics, Nagoya University, Japan, IPPJ-612 (1982).
16. T. A. Mehlhorn, J. M. Peek, E. J. McGuire, J. N. Olsen, and F. C. Young, J. Phys. Colloq. (France) 44, 39 (1983).
17. D. Duston, R. W. Clark, J. Davis and J. P. Apruzese, Phys. Rev. A 27, 1441 (1983).

18. F. A. Mehlhorn, J. Appl. Phys. 52,6522 (1981); Sandia Laboratories Report No. SAND80-0038 (1980).
19. E. J. McGuire, J. M. Peek, and L. C. Pitchford, Phys. Rev. A 26,1318 (1982).
20. J. P. Boris and D. L. Book, J. Comp. Phys. 11, 38 (1973).
21. D. R. Bates, A. E. Kingston and R. W. P. McWhirter, Proc. R. Soc. Lond. A 267,297 (1962).
22. J. P. Apruzese, J. Davis, D. Duston, and R. W. Clark, Phys. Rev. A 29, 246 (1984).
23. J. P. Apruzese, J. Davis, D. Duston, and K. G. Whitney, J. Quant. Spectrosc. Rad. Transfer 23,479 (1980); J. P. Apruzese, J. Quant. Spectrosc. Rad. Transfer 25,419 (1981).
24. J. P. Apruzese, P. C. Kepple, K. G. Whitney, J. Davis, and D. Duston, Phys. Rev. A 24,1001 (1981).
25. F. Biggs and R. Lighthill, Sandia Laboratories Report No. SC-RR-710507 (1971).
26. E. Clementi and C. Roetti, At. Data and Nucl. Data Tables 14,177 (1974).
27. J. E. Rogerson, NRL Memo Report 4485 (1981).
28. R. K. Nesbet and J. F. Ziegler, Appl. Phys. Lett. 31,810 (1977).
29. P. M. Campbell, (1980) (Private communication).
30. K. A. Brueckner and H. Brysk, KMSF Document KMSF - U7 (1971).
31. D. Pines and D. Bohm, Phys. Rev. 85,338 (1952).
32. R. A. McCorkle and G. J. Iafrate, Phys. Rev. Lett. 39,1263 (1977).
33. L. C. Northcliffe and R. F. Schilling, Nuclear Data Tables A7, 233 (1970).

DISTRIBUTION LIST

Assistant to the Secretary of Defense Atomic Energy Washington, D.C. 20301 ATTN: Executive Assistant	1 Copy
Defense Technical Information Center Cameron Station 5010 Duke Street Alexandria, Va 22314	2 copies
Director Defense Intelligence Agency Washington, D.C. 20301 ATTN: DT-1B R. Rubenstein	1 Copy
Director Defense Nuclear Agency Washington, D.C. 20305 ATTN: DDST ATTN: TITL ATTN: RAEV ATTN: STVI	1 copy 4 copies 1 copy 1 copy
Commander Field Command Defense Nuclear Agency Kirtland AFB, New Mexico 87115 ATTN: FCPR	1 Copy
Chief Field Command Livermore Division Department of Defense P.O. Box 808 Livermore, CA 94550 ATTN: FCPRL	1 Copy
Director Joint Strat TGT Planning Staff Offutt AFB Omaha, Nebraska 68113 ATTN: JSAS	1 Copy

Undersecretary of Defense  
for RSCH and ENGRG  
Department of Defense  
Washington, D.C. 20301  
ATTN: Strategic and Space Systems (OS)

1 Copy

Deputy Chief of Staff for RSCH DEV and ACQ  
Department of the Army  
Washington, D.C. 20301  
ATTN: DAMA-CSS-N

1 Copy

Commander  
Harry Diamond Laboratories  
Department of the Army  
2800 Powder Mill Road  
Adelphi, MD 20783  
ATTN: DELHD-N-NP  
ATTN: DELHD-R J. Rosado  
ATTN: DELHD-TA-L (Tech. Lib.)

1 copy each

U.S. Army Missile Command  
Redstone Scientific Information Center  
Attn: DRSMI-RPRD (Documents)  
Redstone Arsenal, Alabama 35809

3 Copies

Commander  
U.S. Army Missile Command  
Redstone Arsenal, Alabama 35898  
ATTN: DRCPM-PE-EA

1 copy

Commander  
U.S. Army Nuclear and Chemical Agency  
7500 Backlick Road  
Building 2073  
Springfield, VA 22150  
ATTN: Library

1 copy

Commander  
U.S. Army Test and Evaluation Command  
Aberdeen Proving Ground, MD 21005  
ATTN: DRSTE-EL

1 Copy

Commanding Officer  
Naval Intelligence Support Center  
4301 Suitland Road, Bldg. 5  
Washington, D.C. 20390  
ATTN: NISC-45

1 Copy

<p>Commander            Naval Weapons Center            China Lake, CA 93555            ATTN: Code 233 (Tech. Lib.)</p>	1 Copy
<p>Officer in Charge            White Oak Laboratory            Naval Surface Weapons Center            Silver Spring, MD 20910            ATTN: Code R40            ATTN: Code F31</p>	1 copy each
<p>Air Force Weapons Laboratory            Kirtland AFB, New Mexico 87117            ATTN: SUL            ATTN: CA            ATTN: APL            ATTN: Lt. Col. Generosa</p>	1 copy each
<p>Deputy Chief of Staff            Research, Development and Accounting            Department of the Air Force            Washington, D.C. 20330            ATTN: AFRDQSM</p>	1 Copy
<p>Space and Missile Systems Organization/IN            Air Force Systems Command            P. O. Box 92960            Worldway Postal Center            Los Angeles, CA 90009            ATTN: IND D. Muskin (Intelligence)</p>	1 Copy
<p>HQ BMO/MM            Norton AFB, CA 92409            ATTN: Col. J. M. Wells</p>	1 Copy
<p>Space and Missile Systems Organization/SK            Air Force Systems Command            Post Office Box 92960            Worldway Postal Center            Los Angeles, CA 90009            ATTN: SKF P. Stadler (Space Comm. Systems)</p>	1 Copy
<p>AVCO Research and Systems Group            201 Lowell Street            Wilmington, MA 01887            ATTN: Library A830</p>	1 Copy



BDM Corporation  
7915 Jones Branch Drive  
McLean, Virginia 22101  
ATTN: Corporate Library

1 Copy

Berkeley Research Associates  
P.O. Box 983  
Berkeley, CA 94701  
ATTN: Dr. Joseph Workman

1 Copy

Berkeley Research Associates  
P.O. Box 852  
5532 Hempstead Way  
Springfield, VA 22151  
ATTN: Dr. Joseph Orens  
ATTN: Dr. Nino Pereira

1 Copy each

Boeing Company  
P. O. Box 3707  
Seattle, WA 98134  
ATTN: Aerospace Library

1 Copy

The Dikewood Corporation  
1613 University Bldv., N.E.  
Albuquerque, New Mexico 8710  
ATTN: L. Wayne Davis

1 Copy

EG and G Washington Analytical  
Services Center, Inc.  
P. O. Box 10218  
Albuquerque, New Mexico 87114  
ATTN: Library

1 Copy

General Electric Company  
Space Division  
Valley Forge Space Center  
P. O. Box 8555  
Philadelphia, PA 19101  
ATTN: J. Peden

1 Copy

General Electric Company - Tempo  
Center for Advanced Studies  
816 State Street  
P.O. Drawer QQ  
Santa Barbara, CA 93102  
ATTN: DASAC

1 Copy

Institute for Defense Analyses  
1801 N. Beauregard St.  
Alexandria, VA 22311  
ATTN: Classified Library

1 Copy

IRT Corporation  
P.O. Box 81087  
San Diego, CA 92138  
ATTN: R. Mertz

1 Copy

JAYCOR  
11011 Forreyane Rd.  
P.O. Box 85154  
San Diego, CA 92138  
ATTN: E. Wenaas

1 Copy

JAYCOR  
205 S. Whiting Street, Suite 500  
Alexandria, VA 22304  
ATTN: R. Sullivan

1 Copy

KAMAN Sciences Corp.  
P. O. Box 7463  
Colorado Springs, CO 80933  
ATTN: J. Hoffman  
ATTN: A. Bridges  
ATTN: D. Bryce  
ATTN: W. Ware

1 copy each

Lawrence Livermore National Laboratory  
University of California  
P.O. Box 808  
Livermore, California 94550  
Attn: DOC CDN for L-153  
Attn: DOC CDN for L-47 L. Wouters  
Attn: DOC CDN for Tech. Infor. Dept. Lib.

1 copy each

Lockheed Missiles and Space Co., Inc.  
P. O. Box 504  
Sunnyvale, CA 94086  
Attn: S. Taimlty  
Attn: J.D. Weisner

1 copy each

Lockheed Missiles and Space Co., Inc.  
3251 Hanover Street  
Palo Alto, CA 94304  
Attn: J. Perez

1 Copy

Maxwell Laboratory, Inc. 9244 Balboa Avenue San Diego, CA 92123 ATTN: A. Kolb ATTN: M. Montgomery ATTN: J. Shannon	1 Copy each
McDonnell Douglas Corp. 5301 Bolsa Avenue Huntington Beach, CA 92647 ATTN: S. Schneider	1 Copy
Mission Research Corp. P. O. Drawer 719 Santa Barbara, CA 93102 ATTN: C. Longmire ATTN: W. Hart	1 Copy each
Mission Research Corp.-San Diego 5434 Ruffin Rd. San Diego, California 92123 ATTN: Victor J. Van Lint	1 Copy
Northrop Corporation Northrop Research and Technology Center 1 Research Park Palos Verdes Peninsula, CA 90274 ATTN: Library	1 Copy
Northrop Corporation Electronic Division 2301 120th Street Hawthorne, CA 90250 ATTN: V. Damarting	1 Copy
Physics International Company 2700 Merced Street San Leandro, CA 94577 Attn: C. Stallings Attn: C. Gilman	1 Copy each
R and D Associates P.O. Box 9695 Marina Del Rey, CA 90291 ATTN: W. Graham, Jr. ATTN: P. Haas	1 Copy each

Sandia National Laboratories P.O. Box 5800 Albuquerque, New Mexico 87115 ATTN: Doc Con For 3141 ATTN: D. McDaniel	1 copy each
Science Applications, Inc. P. O. Box 2351 La Jolla, CA 92038 ATTN: J. Beyster	1 copy
Spire Corporation P. O. Box D Bedford, MA 01730 ATTN: R. Little	1 copy
SRI International 333 Ravenswood Avenue Menlo Park, CA 94025 ATTN: S. Dairiki	1 copy
S-CUBED P. O. Box 1620 La Jolla, CA 92038 ATTN: A. Wilson	1 copy
Texas Tech University P.O. Box 5404 North College Station Lubbock, TX 79417 ATTN: T. Simpson	1 copy
TRW Defense and Space Systems Group One Space Park Redondo Beach, CA 90278 ATTN: Technical Information Center	1 Copy
Vought Corporation Michigan Division 38111 Van Dyke Road Sterling Heights, Maine 48077 ATTN: Technical Information Center (Formerly LTV Aerospace Corp.)	1 Copy

Naval Research Laboratory  
Plasma Radiation Branch  
Washington, D.C. 20375

Code 4720	-	50	Copies
Code 4700	-	26	Copies
Code 2628	-	20	Copies

Director of Research  
U.S. Naval Academy  
Annapolis, MD 21402

2 copies

**END**

**FILMED**

9-85

**DTIC**